UNIVERSITY OF SOUTHAMPTON

FACULTY OF ENGINEERING AND APPLIED SCIENCE

OPTOELECTRONICS RESEARCH CENTRE

THE DEVELOPMENT OF HIGH POWER FIBRE CHIRPED PULSE AMPLIFICATION SYSTEMS

by

Fei He

Thesis for the degree of Doctor of Philosophy

JANUARY 2009

UNIVERSITY OF SOUTHAMPTON

ABSTRACT

FACULTY OF ENGINEERING AND APPLIED SCIENCE
OPTOELECTRONICS RESEARCH CENTRE

Doctor of Philosophy

THE DEVELOPMENT OF HIGH POWER FIBRE CHIRPED PULSE AMPLIFICATION SYSTEMS

by Fei He

With its broad gain bandwidth and high optical conversion efficiency, ytterbium (Yb)-doped silica fiber represents an attractive medium for the generation and amplification of ultrashort optical pulses. Research interest in Yb-doped fiber chirped pulse amplifier (CPA) systems first appeared in the late 1990s. However, the potential advantages and capabilities of Yb-doped fiber CPA systems were not fully studied during the early research. Further scaling of both the average power and the pulse energy have now become possible with the development of several key technologies that are associated with Yb-doped fiber CPA systems.

This thesis describes the development of practical high power, ultra-short pulse, diode pumped, Yb-doped fiber based laser systems. Novel aspects of the systems include the use of dielectric gratings as the pulse stretcher and compressor, and the application of compact chirped-fiber-Bragg-grating (CFBG) pulse stretchers. This thesis also presents the development of a numerical model that can reliably predict the performance of high power Yb-doped fiber amplifier systems. This model has been used to optimize the design of the amplifier cascade in order to maintain the bandwidth of the seed pulse.

This thesis reports two versions of an Yb-doped fiber CPA system that was optimized for either high average power or high pulse energies. The first approach was to operate the fiber CPA system at high pulse repetition rates to achieve high average powers, with the highest possible pulse energy below the nonlinear threshold. The second approach was to operate the fiber CPA system at low pulse repetition rates to achieve high pulse energies. The high energy pulses from this system can be used for high harmonic generation in argon gas to generate ultra-short pulse X-rays in the wavelength range of 10-50 nm.

Finally, the development of a novel fiber CPA system operating with strong self-phase-modulation (SPM) is described, which applied adaptive shaping of the spectral phase of the input pulses. The pre-compensation of both SPM induced phase distortion at high energies, and residual dispersion from mismatched stretcher/compressor technologies at low energies are investigated.

List of contents

List of figures

List of tables

DECLARATION OF AUTHORSHIP

I, Fei He, declare that the thesis entitled:

THE DEVELOPMENT OF HIGH POWER FIBRE CHIRPED PULSE AMPLIFICATION SYSTEMS

and the work presented in the thesis are both my own, and have been generated by me as the result of my own original research. I confirm that:

- this work was done wholly or mainly while in candidature for a research degree at this University;
- where any part of this thesis has previously been submitted for a degree or any other qualification at this University or any other institution, this has been clearly stated;
- where I have consulted the published work of others, this is always clearly attributed;
- where I have quoted from the work of others, the source is always given. With the exception of such quotations, this thesis is entirely my own work;
- I have acknowledged all main sources of help;
- where the thesis is based on work done by myself jointly with others, I have made clear exactly what was done by others and what I have contributed myself;
- parts of this work have been published (see *list of publications*).

Signed: …… ……

Date:……January 2009……

Acknowledgement

I would like to thank my supervisor, Prof. David Richardson, and my co-supervisor, Dr. Jonathan Price for their guidance, encouragement and patience throughout my research and during the writing of this thesis.

I would like to express my gratitude to all those who helped with and encouraged my studies. I am obliged to all the co-workers in my research group, especially Dr. Andrew Malinowski and Dr. Andy Piper. I thank Dr. Jay Dawson, Ben Pyke, Dr. Craig Siders, and Dr. Chris Barty, who provided the dielectric gratings, assisted the stretcher alignment, and shared their experience on designing the pulse stretcher and compressors. I thank Dr. Morten Ibsen for fabricating the chirped fiber Bragg gratings. I thank Dr. Kentaro Furusawa, Dr. Jayanta Sahu and John Hayes, who fabricated the Yb-doped large mode area fibers. I thank Prof. Johan Nilsson and Dr. Daniel Soh for the useful discussions on numerical modelling of Yb-doped fiber amplifiers. I thank Prof. David Shepherd and his research group for making available the pulse shaping technology presented in this thesis.

I am grateful to my mentor, Dr. Eleanor Tarbox, for encouraging my studies and proof reading my thesis. I thank Simon Butler and Tim McIntyre for machining mechanical parts and for advice on the mechanical aspects. I thank ORC staff, Dr. John Mills, Dr. Periklis Petropoulos, Dr. Yoonchan Jeong, Dr. Jacob Mackenzie, Dr. Jerry Prawiharjo, Dr. Marco Petrovich, Dr. Jo Flanagan, Dr. Benn Thomsen, and many other ORC students for discussing ideas, lending equipment and helping things.

I acknowledge the ORC studentship for supporting my PhD studies, and I thank Prof. Rob Eason, Prof. David Shepherd, and Eve Smith for their support of the ORC PhD students.

Finally, I would like to thank my family for their support throughout my studies.

List of abbreviations used

AMCM	Approximate McCumber Method
AOM	Acousto-Optic Modulator
AOTF	Acousto-Optic Tunable Filter
ASE	Amplified Spontaneous Emission
CFBG	Chirped Fiber Bragg Grating
CPA	Chirped Pulse Amplification
CW	Continuous Wave
EDFA	Er Doped Fiber Amplifier
EOM	Electro-Optic Modulator
FFT	Fast Fourier Transform
FWHM	Full Width Half Maximum
GSA	Generalized Simulated Annealing
HR	High Reflectivity
LLNL	Lawrence Livermore National Laboratory
LMA	Large Mode Area
MCVD	Modified Chemical Vapor Deposition
MOPA	Master Oscillator and Power Amplifier
NA	Numerical Aperture
ORC	Optoelectronics Research Centre
OSA	Optical Spectrum Analyzer
PBGF	Photonic Band-Gap Fiber
PBS	Polarizing Beam Splitter
PCF	Photonic Crystal Fiber
PM	Polarization Maintaining
SBS	Stimulated Brillouin Scattering
SESAM	Semiconductor Saturable Absorber Mirror
SLM	Spatial Light Modulator
SPM	Self Phase Modulation
SRS	Stimulated Raman Scattering
WDM	Wavelength Division Multiplexing
Yb	Ytterbium

Chapter 1 Introduction

This PhD thesis presents research on high power, ultrafast, fiber-based laser sources. The aim of this research is to achieve optical pulses, with pulse energies up to the milli-Joule level and pulse durations in the sub-picosecond region, based on Yb-doped fiber chirped pulse amplification (CPA) systems. This fiber source can be used as a seed for high harmonic generation in Argon gas to generate ultra-short pulse X-rays in the wavelength range of 10-50 nm.

High power, ultra-short, pulses are required in many scientific and industrial applications that rely on nonlinear interactions with materials, such as X-ray generation, supercontinuum generation, and the pumping of optical parametric oscillators (OPOs). Over many years of development, bulk crystal solid-state laser and amplifier systems using the CPA technique have established themselves as the source of choice for these applications [1]. A general schematic of a CPA system is illustrated in Figure 1.1. Ultra-short pulses from a seed source are stretched in time in a pulse stretcher to reduce the pulse intensity. Then the stretched pulses are amplified in a cascade of amplifiers without reaching the damage and nonlinear distortion threshold of the gain material (bulk crystal or rare-earth doped fiber). Finally, the amplified pulses are recompressed back to (or close to) the original pulse duration in the compressor which is able to handle a much higher intensity than the gain medium. Although the bulk crystal based CPA systems can deliver the highest pulse energies, they are usually complex and suffer from thermo-optical problems at high average powers which prevent them from being applied in many practical applications of ultrafast technology. The development of a compact source of high power ultra-short pulses has therefore generated strong research interest.

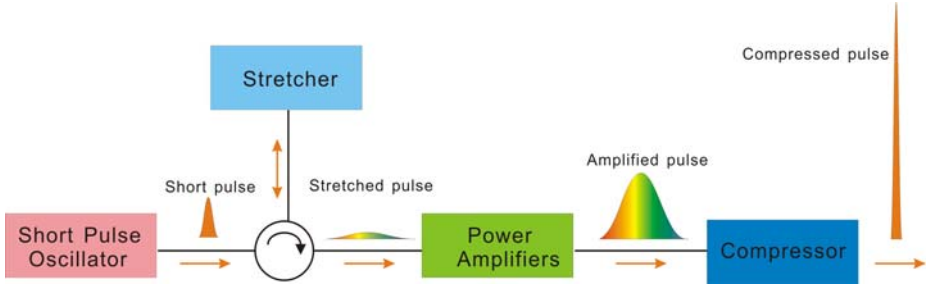

Figure 1.1: Schematic of a typical CPA system

Ytterbium (Yb) doped silica fiber lasers consist of mainly fiber components and therefore have the potential for compactness and robustness. Yb-doped fiber's broad gain bandwidth makes it attractive for both the generation and amplification of ultra-short pulses. Yb-doped fiber provides inherently good thermal management because its high optical conversion efficiency leads to low heat generation and its large surface area aids heat removal. This enables high power pump sources to be used in Yb-doped fiber lasers and amplifiers, without the thermo-optical problems that usually occurred in bulk crystal solid-state lasers. An additional key aspect of Yb-doped fibers is the high beam quality inherent to the tight beam confinement in the fiber.

However, the development of an Yb-doped fiber-based, high power, ultra-short pulse source is challenging. Compared with conventional solid-state laser sources, Yb-doped fiber lasers and amplifiers have a long device length (typically 1-10 m) and a highly confined mode area, which results in strong nonlinear interactions despite the low intrinsic nonlinearity of silica. Therefore, the power level that Yb-doped fiber sources achieve, by using the cladding pumped technology, can easily reach the thresholds of many well known nonlinear effects in fibers such as self phase modulation (SPM) and stimulated Raman scattering (SRS). These nonlinear effects, which are able to degrade output pulse quality, have become the main limitations for power scaling fiber sources. Other technological challenges include the reliability of the seed source, the thermal damage of fibers at high average powers, the optical damage of fibers (especially at the fiber end faces) at high pulse intensities, as well as the compensation of higher order dispersion and the maintenance of the spectral bandwidth in the CPA system in order to avoid distortion to the recompressed pulses.

Pulse stretching and compression is one of the key technologies involved in the development of fiber CPA systems. As high as possible stretching/compressing ratio is usually applied in fiber CPA systems to maintain the pulse from distortions due to the SPM and the SRS (discussed in details in Chapter 2) and to achieve the highest output pulse energy. Conventionally, gold-coated gratings are used in CPA systems within the pulse stretcher and compressor, which provide a pulse stretching/compressing ratio of a few hundred to a thousand times. A compact chirped fiber Bragg grating (CFBG) based pulse stretcher, with both 2^{nd} order dispersion and 3^{rd} order dispersion matched to the compressor, has also been reported in fiber CPA systems [2].

Doped fiber technology itself is another key aspect in fiber CPA systems, and this has progressed rapidly in recent years with the motivation to increase the nonlinear thresholds. Amplifier fibers, such as large mode area (LMA) fiber and photonic crystal fiber (PCF), have been developed to reduce the nonlinearity of the fiber device by using

the largest possible mode area while maintaining mode quality, and minimizing the device length. A detailed discussion on Yb-doped fiber technology is provided in Chapter 2.

Before the start of this thesis research in 2003, pulse energies of ~10 μJ with pulse full width half maximum (FWHM) duration of ~500 fs were demonstrated in fiber CPA systems, and the results were proved to be reliably re-producible [3, 4]. A fiber CPA system with ~1 mJ output pulse energy was reported in 2001 [5]. However, this early demonstration has not been repeated by any other research groups, and it was unclear whether the quoted energies in [5] had included corrections required to account for the ASE power in the output signal.

At the Optoelectronics Research Centre (ORC), University of Southampton, our group started research on the fiber-based CPA system in the 1990s. By taking advantage of the ability of the ORC to fabricate in-house designed CFBGs as the pulse stretcher, and also the ability of the ORC to fabricate LMA fiber for the final fiber amplifier, our group developed a fiber-based CPA system providing ~10 μJ pulse energy [4]. Figure 1.2 shows the schematic of the system. A highly stable, mode locked, fiber laser had been developed and used as the seed to the CPA system. The details of the fiber seed can be found in ref. [6]. Pulses from the fiber oscillator were stretched by the CFBG stretcher (spectral window of 7 nm) with both 2^{nd} order dispersion and 3^{rd} order dispersion required to compensate for the compressor. The stretched pulses were then passed through two single-mode (5 μm core diameter) core-pumped Yb-doped fiber amplifiers. Electro-optic and acousto-optic modulators (EOM/AOM) were used to reduce the repetition rate and filter amplified spontaneous emission (ASE) between amplifier stages, respectively. Power amplification took place in a 9 m length of cladding pumped, LMA fiber with a core diameter of 16.5 μm and a cladding diameter of 200 μm. The fiber was pumped from opposite ends with 915 nm and 975 nm pump diodes. At pulse energies of ~10 μJ, the recompressed pulses had a FWHM pulse duration of ~500 fs and a spectral bandwidth of ~5 nm (the time-bandwidth product $\Delta\nu\Delta\tau \sim 0.7$). Further increase in the pulse energy was limited by the onset of SRS.

With this background research, my supervisor, Professor David Richardson, obtained an Engineering and Physical Sciences Research Council (EPSRC) project grant to develop a practical high power, ultra-short pulse, diode pumped, Yb-doped, fiber-based, laser system for X-ray generation. The aim of the CPA system is to deliver sub-picosecond pulses with up to milli-Joule level pulse energy. This thesis research work is mostly devoted to this project.

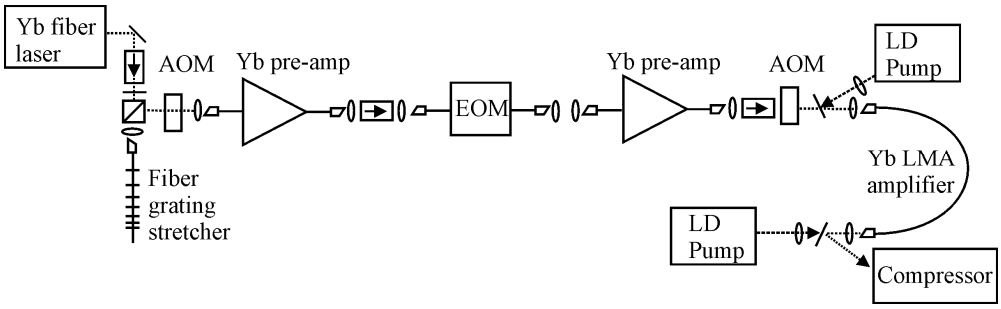

Figure 1.2: Schematic of CPA system developed at ORC. (LD=laser diode.) (from Ref. [7])

My thesis research provided a number of contributions to this research project, as well as to our research group and to the whole research community, which can be summarized as follows:

We collaborated with Lawrence Livermore National Laboratory (LLNL), which is one of the few places in the world that develop state of the art pulse stretching/compression technology. We are grateful to LLNL for the fabrication of the dielectric gratings and assistance with the design of the pulse stretcher and compressor. The dielectric gratings have the advantage of high efficiency, high damage threshold, and a high stretching/compressing ratio, as they can be fabricated in large dimensions [8]. Therefore, they can be used in high average power, as well as in high pulse energy, applications. The stretcher design provided by LLNL minimized spatial inhomogeneities, and dispersion up to 5^{th} order was well matched to the compressor. The stretcher was also designed with the consideration of compactness in mind. I provided contributions in the alignment and optimization of the compressor, the grating characterization, and assistance in the stretcher alignment. The details of the dielectric grating stretcher and compressor are presented in Chapters 5 and 6.

In addition to the bulk grating stretcher work, I also investigated the application of compact CFBG stretchers. The CFBGs, with up to 3^{rd} order dispersion matched to the dielectric compressor, were fabricated at the ORC by Dr. M. Ibsen [9]. I performed detailed and systematic characterization of the CFBG stretchers, including the reflected and transmitted spectra, the dispersion characteristics, and the recompressed pulses from the CPA system when using the CFBG as the stretchers.

In this thesis research, I developed numerical models that reliably predict the performance of high power Yb-doped fiber amplifier systems which consist of different types of Yb-doped fibers and pump techniques [10]. These models were used to optimize the amplifier cascade design in order to maintain the bandwidth of the seed pulse, as any decrease of spectral bandwidth would increase the minimum duration of the

recompressed pulses. In addition, the models were used to assist the LMA fiber design for high power applications, although that research was halted prematurely by the ORC fire that occurred during this thesis research.

In this thesis research, I developed two versions of fiber CPA systems aimed towards high average power or high pulse energies. My first approach was to operate the fiber CPA system at high pulse repetition rates to achieve high average powers, with the highest possible pulse energy below the nonlinear threshold. The system, which consisted of a CFBG stretcher, LMA fibers, and a dielectric grating compressor, provided high quality 360 fs pulses with 70 W average power and 7 μJ energy. As far as I know, this was a world record in terms of the combination of average power and pulse energy for fiber CPA systems when it was reported [11]. During this work, I applied ZEMAX software to enable efficient launching of high pump powers (>350 W) into the double-clad Yb-doped fiber. My second approach was to operate the fiber CPA system at low pulse repetition rates to achieve high pulse energies. The system, which consisted of a dielectric grating stretcher, commercial 40 μm diameter core PCFs, and a dielectric grating compressor, delivered pulses with up to 130 μJ pulse energy (peak power of ~110 MW). The pulses from this system can be used for X-ray generation.

This thesis research also presented the development of a novel fiber CPA system operating with strong SPM, which applied adaptive shaping of the spectral phase of the input pulses. I am grateful to Prof. D. P. Shepherd's group for providing the pulse shaper technology. I investigated pre-compensation of both SPM phase distortion at high energies, and residual dispersion from mismatched stretcher/compressor technologies at low energies. Phase shaping resulted in improved pulse quality. High quality 800 fs, 65 μJ recompressed pulses were produced. This technique could benefit a wide variety of fiber amplifier systems and was self-optimizing for operation at both low and high pulse energies.

In addition to the work on the CPA system, I also contributed to a number of productive collaborations. I developed modeling tools to simulate the gain saturation effect in fiber amplifiers, which was applied to another project in our research group on adaptive pulse shape controlled nanosecond fiber master oscillator and power amplifier (MOPA) systems [12, 13]. The results, which were also published in [10], are presented in Appendix I. The fiber amplifier models developed in this thesis research contributed to other research groups in the ORC, including Prof. D. P. Shepherd's project on a fiber optical parametric amplifier system, and Prof. A. C. Tropper's project on fiber parabolic amplifiers. I collaborated with Dr. M. L. V. Tse from the ORC fiber fabrication group on

the experimental measurement of soliton pulse compression in dispersion-decreasing holey fibers. The results were published in [14].

The contents of each chapter of this thesis are summarized as follows. Chapter 2 reviews some of the basic theories underlying the research presented in this thesis (with the exception of the Yb spectroscopy and numerical modeling techniques that are presented in more detail in Chapter 3). The chapter begins with a brief description of the history of the CPA techniques, followed by an introduction to Yb-doped fiber technology and various nonlinear effects that limit the pulse energy in fibers. This chapter also reviews previously reported fiber-based CPA research undertaken before the start of this Thesis research work and the results from fiber CPA systems published during this Thesis research.

Chapter 3 describes the optimization of the gain bandwidth of Yb-doped fiber amplifier cascades. The chapter starts with the background theories underlying the operation of fiber amplifiers. Results from numerical simulations of the amplifier chain obtained by using modeling tools are compared with experimental results.

The experimental work on the development of the high power ultra-short pulse fiber CPA system is described in Chapters 4-7. Chapter 4 provides an overview of the fiber CPA technology, including a system schematic, the performance of individual components, the pulse selection method that was usually used in our high pulse energy CPA systems [15], and some of the practical limitations. Chapter 5 reports on the performance of a fiber CPA system operating at high repetition rate (10 MHz). The system provided average powers of 70 W and pulse energies of 7 μJ. Chapter 6 describes the performance of the fiber CPA system operating at a low repetition rate (16.7 kHz) as required to achieve high pulse energies. The system produced pulse energies up to 130 μJ. Chapter 7 presents a fiber CPA system incorporating a liquid crystal spatial light modulator (SLM) in order to achieve adaptive phase control of the pulses. Phase shaping resulted in an improved pulse quality, with the autocorrelation peak typically increased by a factor of three compared to unshaped pulses. High quality 800 fs (pulse FWHM), 65 μJ recompressed pulses were produced from that system. Finally, Chapter 8 provides conclusions and discusses future work.

References

[1] D. Strickland and G. Mourou, "Compression Of Amplified Chirped Optical Pulses," *Optics Communications*, vol. 56, pp. 219-221, 1985.

[2] A. Malinowski, A.Piper, J.H.V.Price, F.He, M.Ibsen, J.Nilsson, and D.J.Richardson, "Short pulse high power fiber laser systems," in *Conference on Lasers and Electro-Optics*. Baltimore: Optical Society of America, 2005, (invited).

[3] D. Taverner, A.Galvanauskas, D.Harter, D.J.Richardson, and L.Dong, "Generation of high energy pulses using a large mode area erbium doped fibre amplifier," *Technological Digest of Conference on Lasers and Electro-Optics*, pp. 102-104, 1996.

[4] J. H. V. Price, "The Development of High Power, Pulsed Fiber Laser Systems and Their Applications," in *PhD Thesis, Optoelectronics Research Centre*: University of Southampton, 2003.

[5] A. Galvanauskas, Z. Sartania, and M. Bischoff, "Millijoule femtosecond all-fiber system," presented at Conference on Lasers and Electro-Optics, Baltimore, 2001, paper CMA1.

[6] L. Lefort, J. H. V. Price, D. J. Richardson, G. J. Spuhler, R. Paschotta, U. Keller, A. R. Fry, and J. Weston, "Practical low-noise stretched-pulse Yb^{3+}-doped fiber laser," *Optics Letters*, vol. 27, pp. 291-293, 2002.

[7] J. H. V. Price, A.Malinowski, A.Piper, F.He, W.Belardi, T.M.Monro, M.Ibsen, B.C.Thomsen, Y.Jeong, C.Codemard, M.A.F.Roelens, P.Dupriez, J.K.Sahu, J.Nilsson, and D.J.Richardson, "Advances in high power short pulse fiber laser systems and technology," in *Photonics West*. San Jose, SPIE, 2005, 5709-30 (Invited).

[8] M. D. Perry, R. D. Boyd, J. A. Britten, D. Decker, B. W. Shore, C. Shannon, and E. Shults, "High-Efficiency Multilayer Dielectric Diffraction Gratings," *Optics Letters*, vol. 20, pp. 940-942, 1995.

[9] M. Ibsen, M. K. Durkin, M. J. Cole, M. N. Zervas, and R. I. Laming, "Recent Advances in Long Dispersion Compensating Fiber Bragg Gratings," *IEE Colloquium on Optical Fiber Gratings, (Ref. No.1999/023)*, pp. 6/1-7, 1999.

[10] F. He, J.H.V.Price, K.T.Vu, A.Malinowski, J.K.Sahu, and D.J.Richardson, "Optimisation of cascaded Yb fiber amplifier chains using numerical-modelling," *Optics Express*, vol. 14, pp. 12846-12858, 2006.

[11] F. He, J. H. V. Price, A. Malinowski, A. Piper, M. Ibsen, and D. J. Richardson, "High Average Power, High Energy, Femto-second Fiber Chirped Pulse Amplification System," presented at Conference on Lasers and Electro-Optics, Baltimore, 2007, CMEE5.

[12] K.T.Vu, A.Malinowski, D.J.Richardson, F.Ghiringhelli, L.M.B.Hickey, and M.N.Zervas, "Adaptive pulse shape control in a diode-seeded nanosecond fiber MOPA system," *Optics Express*, vol. 14, pp. 10996-11001, 2006.

[13] F.He, J.H.V.Price, K.T.Vu, A.Malinowski, J.K.Sahu, and D.J.Richardson, "Optimisation of cascaded Yb fiber amplifier chains using numerical-modelling," *Optics Express*, vol. 14, pp. 12846-12858, 2006.

[14] M.L.V.Tse, P.Horak, J.H.V.Price, F.Poletti, F.He, and D.J.Richardson, "Pulse compression at 1.06 microns in dispersion-decreasing holey fibers," *Optics Letters*, vol. 31, pp. 3504-3506, 2006.

[15] M. E. Fermann, A. Galvanauskas, and G. Sucha, *Ultrafast lasers : technology and applications*. New York: Marcel Dekker, 2003.

Chapter 2 Background theory and practical technology used in fiber-based CPA systems

In order to generate high power, ultra-short pulses, the CPA technique is used in state of the art laser systems. Nonlinear effects, such as SPM and SRS, have been observed in different fiber-based CPA systems, and are believed to be the main limitation to power scaling [1-3]. Therefore, fiber technology has been developed in recent years towards producing a larger mode area and higher pump absorption (thus shorter device length can be used) to increase the threshold for nonlinear distortions. To provide the background knowledge on the work presented in this thesis, this chapter presents the development of CPA and associated fiber technology, introduces the nonlinear fiber optics theory, and reviews other high power fiber-based CPA systems reported both before, and during, this thesis research.

This chapter is organized as follows. Section 2.1 provides a brief history of the development of the fiber CPA systems. Section 2.2 begins with an introduction to the main properties of Yb-doped fibers and then provides a brief summary of the development of Yb-doped fiber designs for high power pulse amplification, including core-pumped single-mode fiber, double-clad fiber, LMA fiber, and PCF. Section 2.3 describes the effects of dispersion on ultra-short pulses, which is useful for understanding the stretching and compression process in CPA systems and the effects of mismatched dispersion between stretcher and compressor. Important nonlinear effects, such as SPM and SRS, are also discussed in this section. Section 2.4 reviews the development of the pulse stretcher and compressor technologies, state of the art high pulse energy fiber CPA systems, and the technologies that have been used to overcome the key limitations in fiber CPA systems.

2.1 The elements of fiber CPA systems

The CPA technique, which was originally developed in the context of radar technology, was first applied to laser systems by Donna Strickland and Gérard Mourou at the

University of Rochester in the mid 1980s [4]. In high power, ultra-short pulse, laser sources, the pulse peak power in the gain medium was limited not only by material damage, but also by some well-known nonlinear effects. For example, the pulse peak power in bulk crystals was limited by nonlinear processes such as self-focusing, and the pulse peak power in fibers was limited by nonlinear effects such as SPM and SRS. In a CPA system, an ultra-short laser pulse can be stretched in time scale to reduce its intensity by a factor of 10^3 or more. The stretched pulse is then amplified in the gain medium at power levels below the nonlinear threshold. Finally, the amplified laser pulse is recompressed back to the original pulse width, thus achieving orders of magnitude higher peak power than laser systems could generate before the invention of CPA.

Since its first demonstration, CPA was widely used in bulk crystal solid state lasers for the generation of high power ultra-short pulses. Until now, CPA is still the state of the art technique which almost all of the highest power lasers (with pulse peak powers in the petaWatt level) in the world currently utilize [5, 6].

Rare-earth doped fiber, which can be used as the gain medium for laser generation and amplification, was first developed in the 1960s based on Nd-doped glass [7]. Early work was focused on Nd-doped fibers because of the Nd^{3+} ion's advantage of a four level transition, which allowed the use of low brightness pumps such as flash lamps. In the 1980s, the demonstration of the modified chemical vapor deposition (MCVD) process has enabled the fabrication of low loss, rare-earth doped, silica fiber [8]. As a result, rapid progress in the development of Er-doped fiber amplifier (EDFA) technology took place due to its application in telecommunications. Therefore, initial fiber CPA work started with Er-doped fibers, but further power scaling was achieved in the late 1990s by the use of Er/Yb and Yb-doped LMA fibers in conjunction with the cladding pumping technique. Current state of the art high power fiber-based CPA systems usually utilize Yb-doped fiber due to its advantages presented in the next section.

2.2 Fiber technologies available for application in CPA systems

2.2.1 Yb-doped silica fiber

Yb-doped silica fiber has attracted interest since the 1990s because of its unique energy level structure and spectroscopic characteristics. The energy level structure of the Yb^{3+} ion is simple compared to other rare-earth ions. As shown in Figure 2.1, the Yb^{3+} ion's energy levels consist of only two relevant manifolds: the ground manifold $^2F_{7/2}$ (with four

Stark levels, labeled as (a) to (d)) and a well-separated excited manifold $^2F_{5/2}$ (with three Stark levels, labeled as (e) to (g)), ~10,000cm^{-1} above the ground level [9]. This simple structure provides freedom from unwanted processes such as excited state absorption of pump or signal, and concentration quenching by an inter-ionic energy transfer process, which can be observed in other rare-earth doped fibers, notably EDFAs [10].

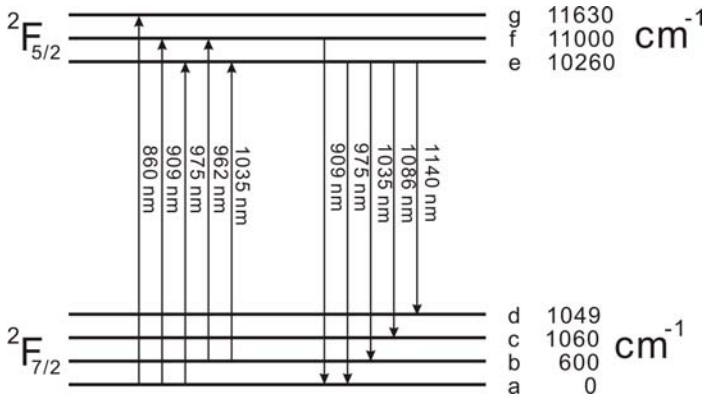

Figure 2.1: Yb^{3+} ion's energy level structure [9]

Unlike the Nd^{3+} ion which is a four-level system, the Yb^{3+} ion has only three-level and quasi-three-level transitions, which require a higher pump intensity to create gain. However, with the development of high brightness diode laser pumps and low loss single-mode, rare-earth doped, silica fibers, Yb-doped fiber laser and amplifier systems have become the preferred gain medium for high average power, high beam quality, laser applications.

The unique features of Yb's spectroscopy, which will be discussed in detail in Chapter 3, make Yb-doped silica fiber one of the most ideal gain media for short pulse amplification. A number of key characteristics of Yb-doped fiber laser and amplifier systems can be summarized as follows [9, 11]:

- Broad absorption and emission bandwidth.
- High power diode pumping: cladding-pumping makes it possible to use compact, low brightness but high power diodes.
- Simple energy level structure which avoids excited state absorption, concentration quenching and cooperative upconversion.
- Low quantum defect: Yb-doped glass fiber has a quantum defect of less than 10%, which can provide optical-to-optical efficiencies well above 80%.

- Good thermo-optical behaviour: thermal lensing effects in an optical fiber are orders of magnitude weaker compared to a solid-state medium due to the distributed heat dissipation [12].
- Compact and robust: mode is defined by fiber refractive index profile; good mode quality can be guaranteed by the refractive index profile design, and is not dependent on the free-space alignment of a free-space cavity.
- Variable repetition rates: Yb's long upper level lifetime (~1 ms) enables continuous-wave (CW) pumping of Yb-doped fiber amplifiers operating at repetition rates from GHz to kHz by appropriate time-gating of the seed pulses.

2.2.2 Double-clad fiber and cladding-pumped technology

High NA (NA>0.1), small core (core diameter <10 μm) Yb-doped single-mode fibers can be used in core-pumped amplifiers where signal and pump light are coupled into an Yb-doped fiber core by using a wavelength division multiplexing (WDM) coupler, as shown in Figure 2.2 (a). Although core-pumped amplifiers have advantages of stability, compactness, high gain and low noise, the output power is limited to <1 W by the amount of pump power available from single-mode pump diodes. Therefore, core-pumped amplifiers are usually used as low power, high gain, pre-amplifiers at the beginning of an amplifier cascade.

The development of double-clad fiber and cladding-pump technology allows for the use of high power, multimode, pump sources, which enables the power scaling of fiber lasers from the sub-watt level to the kilowatt level. The typical design of a double-clad fiber is shown in Figure 2.2(b). The core (primary waveguide) is usually doped with rare-earth material, and guides the input signal. The inner cladding (secondary waveguide) has a lower refractive index compared with the core, and is designed to be multimode to enable coupling and guiding of the light emitted from highly multimode pump sources. The outer cladding has a lower refractive index than the inner cladding. The design of double-clad fiber allows the launch of powerful multimode diode pumps while the core structure still controls the output signal mode quality. Therefore, a low brightness, high power, diode laser can be used to pump a high brightness signal beam in cladding-pumped amplifiers.

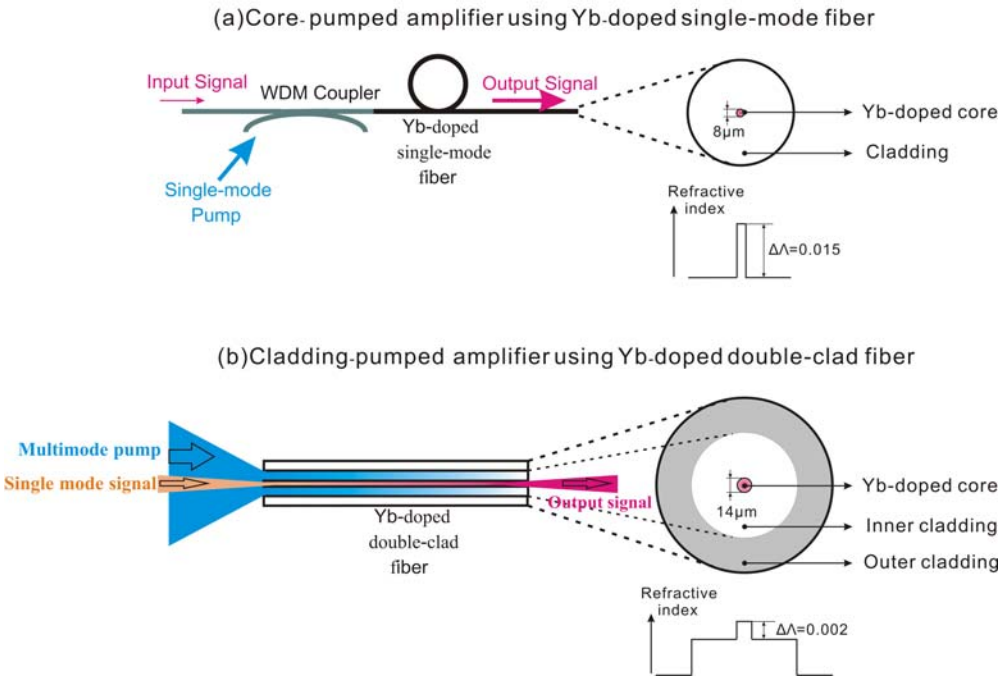

Figure 2.2: Amplifier configuration, fiber cross- section and index profile design of (a)core-pumped amplifier using Yb-doped single-mode fiber, and (b)cladding-pumped amplifier using Yb-doped double-clad fiber.

The pump absorption is typically quite low (<0.4 dB/m, at 975 nm) in conventional circularly-symmetrical, double-clad Yb fibers (Figure 2.3(a)), because some of the guided pump light propagates in helical modes and does not have sufficient overlap with the doped core [13-15]. Therefore, a D-shaped inner cladding design (Figure 2.3(b)) has been applied in ORC fabricated, Yb-doped, double-clad fibers to promote inter-modal mixing for improving the pump absorption. With a core to inner cladding diameter ratio of 1:10, the ORC fibers have a typical pump absorption of ~3 dB/m at 975 nm.

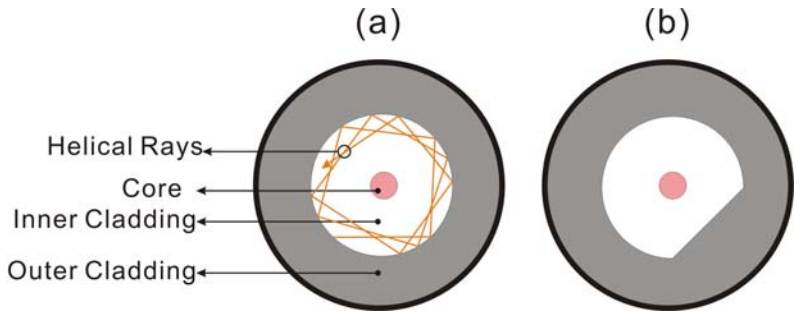

Figure 2.3: Inner cladding designs of Yb-doped double-clad fiber. (a) circular, (b) D-shape

2.2.3 The development of fiber technology for high power applications

2.2.3.1 Single-mode fiber

Single-mode fibers support only one propagation mode per polarization state for a given wavelength [16]. In the simplest form, an optical fiber consists of a core and a cladding with different refractive indices, a structure which is also referred to as step-index fiber. For step-index fibers, the number of modes supported by the fiber can be determined by the normalized frequency, also referred to as the V number, which is defined as

$$V = \frac{2\pi\ a}{\lambda}\sqrt{n_1^2 - n_2^2} \tag{2.1}$$

where n_1 and n_2 are the refractive index of the core and cladding respectively, a is the core radius and λ is the wavelength of light [17, 18]. The condition for only single-mode guidance is ensured subject to the following condition

$$V < 2.405 \tag{2.2}$$

Single-mode characteristics of standard step-index fibers are limited to a certain wavelength range. The short wavelength limit is set by the single-mode cut-off wavelength, beyond which the single-mode condition (Equation 2.2) is no longer satisfied. The long wavelength limit is defined in practice by the bend losses or sometimes the material absorption. In contrast to step index fibers, PCF can be designed to provide endlessly single-mode operation, which results in a very wide single-mode wavelength range. The details will be discussed in the following sections.

The numerical aperture (NA) is another important fiber parameter, and defined as the sine of the maximum angle of an incident ray with respect to the fiber axis, so that the ray hitting the fiber core can be transmitted into and guided in the core. Figure 2.4 illustrates the ray picture of how light is coupled into the fiber.

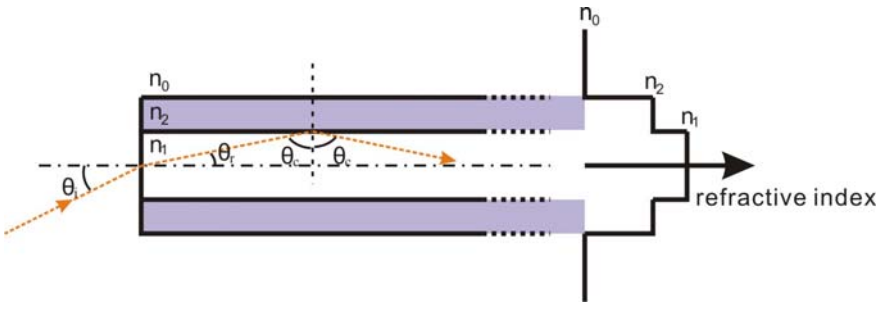

Figure 2.4: The ray picture of fiber NA

When a light ray is incident from air with refractive index $n_0 \cong 1$ to the fiber core, Snell's law gives

$$n_0 \sin\theta_i = n_1 \sin\theta_r \tag{2.3}$$

where θ_i is the incident angle of the input light, and θ_r is the refracted angle. From Figure 2.4, we also have

$$\theta_r = 90^0 - \theta_c \tag{2.4}$$

where θ_c is the critical angle for total internal reflection

$$\sin\theta_c = \frac{n_2}{n_1} \tag{2.5}$$

By substituting Equation (2.4) and (2.5) into (2.3), we can derive the relation between the NA and the refractive index of the core and cladding, as [19],

$$NA \cong \sin\theta_{i\_\max} \cong \sqrt{n_1^2 - n_2^2} \tag{2.6}$$

Note that Equation (2.6) only provides an approximation of the connection between the NA and the acceptance angle of the fiber. This relation becomes less reliable for non-step-index fibers.

Bending loss is the propagation loss in an optical fiber caused by bending. A fiber with high NA usually has low bending loss, as the light is strongly guided. The bending loss can increase very quickly once a critical bend radius is reached. This bending radius limit can vary from a few millimeters (for fibers with high NA) to tens of centimeters (for fibers with low NA).

At a certain bending radius, the bending loss is typically larger for higher-order modes in a multimode fiber. Therefore, by properly adjusting the bend radius, it is possible to introduce significantly higher losses for higher-order modes, without affecting the lowest-order mode. This technique has been applied in high power fiber amplifiers when using a fiber that can support several modes to achieve a higher effective mode area.

2.2.3.2 Large mode area fiber

For some applications, such as the amplification of intense pulses in fibers, presented in this thesis research, it is desirable to use fibers with LMA, with a single-mode (or only a few modes) guidance. A typical single-mode fiber has a core diameter of a few micrometers, corresponding to an effective mode area of less than 100 μm^2, whereas LMA fibers can have larger core diameters of tens of micrometers, corresponding to an effective mode area of hundreds or even thousands of μm^2. Due to the reduced pulse

intensities, LMA fibers effectively have lower nonlinearities and a higher damage threshold than standard single-mode fibers.

A straightforward approach to obtain LMA fiber with single-mode propagation is to increase the core size and decrease the NA. However, as the fiber guiding becomes weak with the decrease of NA, the bending losses can be significant, and ultimately this becomes the critical limit for the largest achievable mode areas. Additional difficulties can arise from the refractive index control when introducing high concentrations of rare-earth dopants into the fiber core. PCF technology has been developed as another approach to obtain single-mode fibers with LMAs. PCFs with mode area of a few thousands of μm^2 have been reported recently [20-22]. However, the increase of the mode area of the PCFs is also limited by the weak guidance problem [23, 24].

In practice, it is possible to use quasi-single-mode fibers, which are not strictly single-mode but support only a few transverse modes, in fiber amplifiers to achieve close to diffraction limited beam quality [1]. Bending of the fiber is usually used to give high losses to all the higher-order modes. The practical difficulty is the launching of the input signal, as well as the optimization and the reliability of the bending condition.

The LMA fibers fabricated at the ORC have benefitted from refined design approaches and have an optimized refractive index profile and doping distribution. A typical index profile design of an ORC fabricated Yb-doped LMA fiber is shown in Figure 2.5. The refractive index profile consists of a low NA central core region having a diameter of 30-40 μm with Yb ions selectively doped into only the central part of the core to give preferential gain to the fundamental mode, which has peak intensity at the centre. An outer ring of raised index is incorporated to reduce the fiber bend loss. Although the core size has been extended beyond the strictly-single-mode region, these LMA fibers can provide near diffraction limited beam quality by launching the input signal beam appropriately.

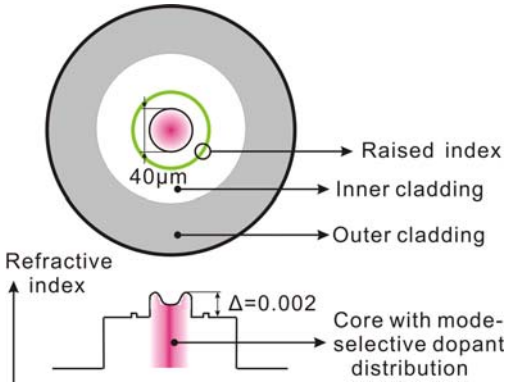

Figure 2.5: Index profile design of ORC fabricated Yb-doped LMA fiber

2.2.3.3 Photonic crystal fiber

PCF is a kind of optical fiber which obtains light guiding properties through its built-in microstructure. The unique cladding structure of PCF is shown in Figure 2.6. PCFs can have either a 'solid-core' or a 'hollow-core' with a periodic photonic crystal lattice of hollow channels in the cladding. According to their mechanism for light confinement, PCFs can be divided into two categories, high index guiding fibers and low index guiding fibers. Those with a 'hollow-core', or a solid-core with a lower index than the microstructured cladding, can confine light by the photonic bandgap effect [25]. Such low index guiding PCF is also referred to as Photonic Band-Gap Fiber (PBGF), which is not related to the work presented in this thesis. In contrast, high index guiding PCF, which usually has a solid core with a higher average index than the microstructured cladding, can operate on the same index-guiding principle as conventional optical fiber. The guiding property of high index guiding PCF is usually viewed as a modified form of total internal reflection. The freedom to manipulate the parameters, including the hole diameter, d, lattice pitch, Λ, and the air hole shape of the PCF provides a means of controlling the refractive index profile more precisely than other fiber technology. In the rest of this thesis, unless otherwise noted, the abbreviation PCF refers to high index guiding solid-core PCF.

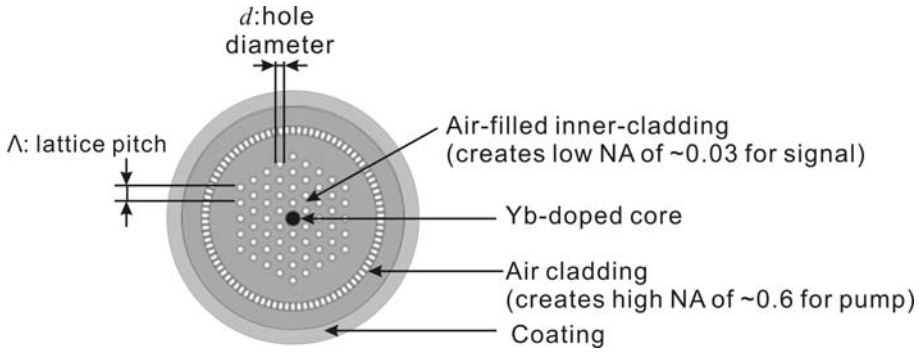

Figure 2.6: A typical design of Yb-doped PCF for high power applications [3, 26]

The V-number and the single-mode condition (Equation (2.1) and (2.2)) for step-index fibers can be applied to the PCFs by the use of the effective cladding index, which is strongly dependent on λ/Λ [27]. Figure 2.7 shows the single-mode boundary $V = 2.405$ of the normalized wavelength λ/Λ over the relative hole diameter d/Λ [3]. When $d/\Lambda < 0.4$, the PCF becomes single-mode for all the λ/Λ. This region is referred to as the endlessly single-mode region [27].

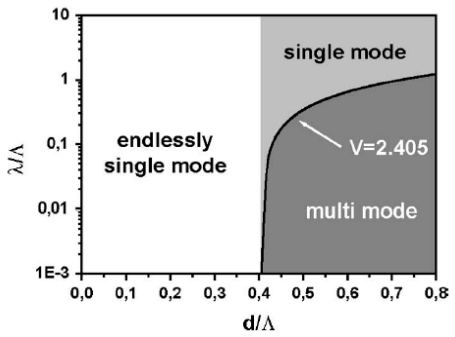

Figure 2.7: Endlessly single-mode region for PCFs (from ref.[3])

The flexibility of micro-structuring also provides the realization of double-clad PCF with a high NA of the inner cladding for efficient pump coupling. In a typical design of Yb-doped PCF for high power applications (Figure 2.6), the air-silica micro-structured inner cladding of the fiber is surrounded by a web of silica bridges (referred to as an air cladding). Due to the very large contrast of refractive index introduced by the air cladding structure, PCF can have a high inner cladding NA of up to 0.6 (relative to polymer coated double-clad fibers with an inner cladding NA of ~0.4). For a given inner cladding dimension, higher NA lowers the requirements on the pump source with respect to beam quality and brightness.

Commercial PCF, with a mode field diameter as large as 30 μm (effective mode area of 750 μm^2), with robust single-mode operation, is available from Crystal Fibre A/S. The core has a diameter of ~40 μm with a NA of ~0.03. The inner cladding has a high NA of 0.6, and thus allows the diameter of the inner cladding to be reduced to 170 μm while maintaining sufficient brightness acceptance for efficient pumping. This results in a high overlap ratio of the core to the inner cladding, leading to shorter absorption lengths, and therefore a short device length of 1~2 m can be used to reduce fiber nonlinearity. The outer cladding diameter of this fiber is 620 μm.

In order to achieve extreme scaling of the mode area to further reduce nonlinearity, a rod-type PCF with NA of 0.02 and core diameter of 60 μm (effective mode area of ~2000 μm^2) was reported in 2005 [28]. The inner cladding had a diameter of 180 μm, with an NA of 0.6, and the outer cladding diameter was as large as 2 mm and possessed no coating in order to enable heat-sinking.

The scaling of the mode area of rod-type PCFs had developed quickly in the last two years. A rod-type PCF with a core diameter of 70 μm (effective mode area of ~2200 μm^2) became commercially available from Crystal Fibre A/S in 2007 [29]. A rod-type PCF with a core diameter of 80 μm (effective mode area of ~4000 μm^2) was

reported at Friedrich-Schiller-University, Jena in 2007 [21]. The pump absorption of this fiber was measured to be as high as 30 dB/m, at 976 nm, which allowed a length of just a few tens of centimeters to be used in a laser or amplifier setup. The increased effective mode area and reduced fiber length allowed for significant pulse peak power and energy scaling.

2.2.4 Beam quality

Beam quality, which controls the size of the focused spot and the divergence of the laser beam, is a critical parameter for many applications. For a laser beam, the beam parameter product is the product of a laser beam's divergence angle (half-angle) and the radius of the beam waist. The beam quality is usually quantified by the M^2 factor in practice, which is the ratio of the beam parameter product of an actual beam to that of a diffraction-limited Gaussian beam at the same wavelength. In other words, the half-angle divergence of an actual laser beam is:

$$\theta = M^2 \frac{\lambda}{\pi \omega_0} \tag{2.7}$$

where ω_0 is the beam radius of the beam waist.

Laser beams with $M^2 = 1$ corresponds to a diffraction limited Gaussian beam, which usually can be provided by a laser with a single transverse mode. A diffraction limited beam has the minimum possible beam divergence for a given waist radius, and the potential to be focused to the smallest possible spots for a given wavelength.

The M^2 factor can be calculated from the measured evolution of the beam radius along the propagation direction. In the M^2 measurements presented in this thesis research, the beam radius is measured by using the Beamscan series product from Photon Inc., and the calculation is in accordance with international organization for standardization (ISO) Standard 11146 [30].

2.2.5 Polarization maintaining fiber

Conventionally, a single-mode fiber is not truly single-mode because it can support two orthogonally polarized modes [16]. Real fibers always exhibit some degree of birefringence, which is the difference of the modal refractive indices for the two orthogonally polarized states, due to the small departures from cylindrical symmetry.

When a linearly polarized laser beam propagates in a birefringent medium, with the polarization direction not on one of the birefringent axes, there are two polarization components with different wavenumbers. As a result, the light propagating in the fiber changes its polarization state in an uncontrolled way with bending and temperature variations [16].

In order to transmit light without changing its state of polarization, polarization-maintaining (PM) optical fiber has been developed by introducing high built-in birefringence ($\sim 10^{-4}$). With the increase of birefringence, the differences of the propagation constants of the two polarization modes are increased. As a consequence, the disturbance along the fiber required to effectively couple the two polarization modes is also increased. Provided that the birefringence is large enough and that the polarization of light launched into the fiber is aligned with one of the birefringent axes, the input polarization state will be preserved even if the fiber is bent.

PM fibers have a number of advantages when used in Yb-doped fiber amplifiers. PM fibers can maintain the output polarization state without changes due to temperature and bending variations, while non-PM fiber cannot. In addition, PM fiber does not allow nonlinear polarization rotation, a phenomenon where the change in the polarization state of light in a fiber is dependant on the intensity [16].

Although we are aware of the advantages of using PM fibers, there is no intrinsic difference between Yb-doped PM and non-PM fibers in respect to gain, nonlinear effects, output mode quality, and slope efficiency, which are more critical characteristics for our applications. Note that polarization mode dispersion, which has been studied extensively for optical communication systems [16], is generally not an issue for fiber amplifiers due to the relatively short length. Therefore, non-PM fibers have mainly been used in this thesis research.

2.3 Nonlinear fiber optics

In order to enable a thorough understanding of the nonlinear effects in fibers, this section will provide an overview of nonlinear fiber optics theory. Dispersion, which arises from the linear response of the bound electrons in silica and the waveguide dispersion of the fiber, will be described first because of its significance due to the broad bandwidth of the ultra-short pulses. The optical Kerr effect, the phenomenon in which the refractive index of the medium changes when the electron orbit is deformed by a strong electric field [31], must be considered when the pulses have high peak powers. The Kerr nonlinearity

introduces SPM and cross phase modulation (XPM), which are due to the elastic response of the bound electrons to an intense optical field. Raman and Brillouin scattering, which are caused by inelastic scattering where energy is exchanged with the medium through the creation or annihilation of phonons, are the other nonlinear phenomena that usually appear when high peak power pulses are propagating in fibers.

2.3.1 Pulse propagation equation

The propagation equation for broad bandwidth optical pulses propagating in low loss single-mode fibers, also known as the nonlinear Schrödinger equation, can be expressed as

$$i\frac{\partial A}{\partial z} - \frac{\beta_2}{2}\frac{\partial^2 A}{\partial t^2} + i\frac{\alpha}{2}A + \gamma|A|^2 A = 0 \tag{2.8}$$

where $A(z,t)$ is the pulse amplitude and is normalized such that $|A|^2$ represents the optical power [16]. z is the position along the fiber and t is the time. β_2 is the group velocity dispersion (GVD), α is the loss coefficient, and the nonlinear parameter, γ, is defined as

$$\gamma = (n_2\omega_0)/(cA_{eff}) \tag{2.9}$$

In Equation (2.9), n_2 is the nonlinear refractive index coefficient related to the 3rd order susceptibility $\chi^{(3)}$ of optical fibers. n_2 is a measure of the intensity dependence of the refractive index $\tilde{n}(\omega, I)$ by the relation $\tilde{n}(\omega, I) = n(\omega) + n_2 I$, where $n(\omega)$ is the linear responds of the refractive index, I is the intensity, and ω is the angular frequency. A_{eff} is the effective core area which is related to the modal distribution, $F(x,y)$, by

$$A_{eff} = \frac{\left(\int\int_{-\infty}^{\infty}|F(x,y)|^2\,dxdy\right)^2}{\int\int_{-\infty}^{\infty}|F(x,y)|^4\,dxdy} \tag{2.10}$$

The second and fourth term in Equation (2.8) govern the effect of dispersion and nonlinearity respectively. Depending on the pulse's initial duration, T_0, and peak power, P_0, the dispersion length $L_D = T_0^2/|\beta_2|$ and the nonlinear length $L_{NL} = 1/(\gamma P_0)$ provide the length scales over which dispersive or nonlinear effects become important for pulse evolution. The dispersion dominated region corresponds to the case when

$L_D << L_{NL}$, which will be discussed in section 2.3.2. The nonlinearity dominated region corresponds to the case when $L_D >> L_{NL}$, which will be discussed in section 2.3.3.

2.3.2 Group velocity dispersion in silica fibers

The one dimensional propagation equation, described in Equation (2.8), enables us to study the effects of dispersion. In a linear dispersive medium, the effect of GVD can be studied by setting $\gamma = 0$ in Equation (2.8). If we use the normalized amplitude, U , as $A(z,t) = \sqrt{P_0}\exp(-\alpha\ z/2)\ U(z,t)$, where P_0 is the peak power of the incident pulse, $U(z,t)$ satisfies the following equation

$$i\frac{\partial U}{\partial z} = \frac{\beta_2}{2}\frac{\partial^2 U}{\partial t^2} \tag{2.11}$$

For ultra-short pulses, it is necessary to include the β_3 term in Equation (2.11) because the expansion parameter, $\Delta\omega/\omega_0$, is no longer small enough to justify the truncation of the Taylor expansion of $\beta(\omega)$ after the β_2 term. The propagation equation including both β_2 and β_3 terms, while still neglecting the nonlinear effects, can be written as

$$i\frac{\partial U}{\partial z} = \frac{\beta_2}{2}\frac{\partial^2 U}{\partial t^2} + \frac{i\beta_3}{6}\frac{\partial^3 U}{\partial t^3} \tag{2.12}$$

This equation can be solved by using the Fourier-transform method. The general solution is

$$U(z,t) = \frac{1}{2\pi}\int_{-\infty}^{\infty}\tilde{U}(0,\omega)\exp\left(\frac{i}{2}\beta_2\omega^2 z + \frac{i}{6}\beta_3\omega^3 z - i\omega t\right)d\omega \tag{2.13}$$

where $\tilde{U}(0,\omega) = \int_{-\infty}^{\infty}U(0,t)\exp(i\omega t)dt$.

When the incident field $U(0,t)$ is specified to be a Gaussian, super-Gaussian or Hyperbolic-Secant pulse, the effects of dispersion and 3rd order dispersion can be studied analytically. For example, a Gaussian pulse has an incident field defined by

$$U(0,t) = \exp\left(-\frac{t^2}{2T_0^2}\right) \tag{2.14}$$

where T_0 is the half-width at the $1/e$ intensity point. For a Gaussian pulse, T_0 is related to the full width half maximum (FWHM) width by $T_{FWHM} \approx 1.665T_0$. By using Equation (2.14) with Equation (2.13), Gaussian pulses with dispersion effects can be expressed as

$$\tilde{U}(z,\omega) = \left(2\pi T_0^2\right)^{1/2} \exp\left[\frac{i\omega^2}{2}\left(\beta_2 z + iT_0^2\right) + \frac{i}{6}\beta_3\omega^3 z\right] \qquad (2.15)$$

The effects of dispersion on ultra-short pulse are important in CPA systems because residual dispersion from the stretcher, the compressor, and all other dispersive components in the system will result in symmetric ($\beta_2 z$ mismatch) and asymmetric ($\beta_3 z$ mismatch) pulse broadening. Figure 2.8(a) and (b) depict the pulse broadening with different $\beta_2 z$ and $\beta_3 z$ values respectively for a Gaussian input pulse with 0.22 ps FWHM. It can be seen that the principal effect of dispersion ($\beta_2 z$) is a symmetric broadening of the pulse and the creation of a linear chirp. However, the principal effect of 3rd order dispersion ($\beta_3 z$) is asymmetric broadening of the pulse and the creation of a quadratic chirp. Pulses with a combination of 2nd order dispersion and 3rd order dispersion are also illustrated in Figure 2.8 (c). As the dispersion introduced in the stretcher and compressor are much higher than the dispersion from other components such as Yb-doped fibers, a pulse stretcher and compressor with accurately matched dispersion are usually used in CPA systems.

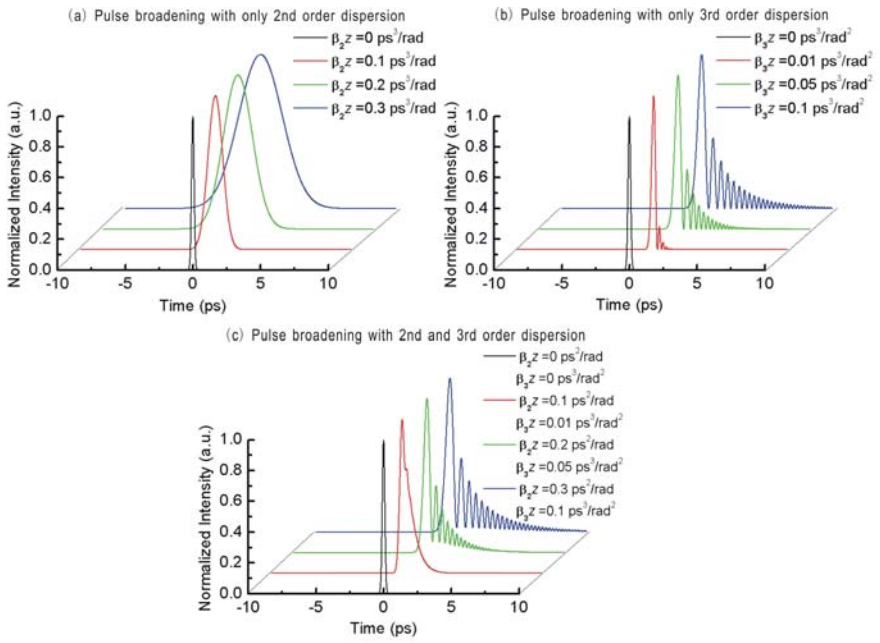

Figure 2.8: The effects of 2nd order dispersion and 3rd order dispersion on pulses

2.3.3 Self phase modulation

As discussed in section 2.3.1, when pulses are in the nonlinearity dominated region ($L_D >> L_{NL}$), the effect of dispersion is negligible. Therefore the SPM effect can be analyzed by setting $\beta_2 = 0$ in Equation (2.8)

$$\frac{\partial U}{\partial z} = i\gamma |U|^2 U \tag{2.16}$$

The solution of Equation (2.16) is

$$U(L,t) = U(0,t)\exp[i\phi_{NL}(L,t)] \tag{2.17}$$

where L is the fiber length and

$$\phi_{NL}(L,t) = |U(0,t)|^2 (\gamma P_0 L) \tag{2.18}$$

The nonlinear phase change in Equation (2.18) is referred to as SPM, which is related to the intensity dependence of the refractive index. The accumulated nonlinear phase at the pulse centre (where $t = 0$ and $|U(0,0)| = 1$) can be defined as

$$B = \int_0^L \phi_{NL}(z)dz = \int_0^L \gamma\ P_0 dz \tag{2.19}$$

which is also known as the B-integral. Pulse quality degradation in CPA systems is ordinarily expected when $B > 1$ [32].

By using Equation (2.9), the B-integral in a fiber amplifier can be written as

$$B = \frac{n_2 \omega_0}{cA_{eff}} P_0 L_{eff} \tag{2.20}$$

where $L_{eff} = [1 - \exp(-gL)]/g$ and g is the gain coefficient of the amplifier. From Equation (2.20), we can see that for pulses with a certain output peak power, P_0, the effect of SPM can be reduced by decreasing the effective fiber length L_{eff} or increasing the fiber effective mode area A_{eff}. Note that in the B-integral calculations in this thesis a constant gain coefficient is assumed, and the output pulse peak power, P_{peak}, is estimated from the measured output average power, P_{ave}, by using

$$P_{peak} = \frac{P_{ave}}{R_f * \tau_{FWHM}} \tag{2.21}$$

where R_f is the pulse repetition rate, and τ_{FWHM} is the FWHM duration of the stretched pulse.

The temporally varying phase will result in a difference in the instantaneous optical frequency across the pulse from its central value, ω_0, which is also referred to as frequency chirping

$$\delta\omega(T) = -\frac{\partial\phi_{NL}}{\partial T} \tag{2.22}$$

As can be seen from Equation (2.22), for pulses without initial chirp, new frequency components are generated continuously as the pulse propagates in fibers, which will consequently broaden the spectrum over its initial width at z = 0.

The effect of SPM on a Gaussian pulse is illustrated in Figure 2.9. The input pulse has a FWHM width of 1 ns, centered at 1055 nm. With different B-integral values, the pulse's temporal profile remains unchanged (Figure 2.9 (a)), while the spectral profiles are broadened (Figure 2.9 (b)). The chirp of the pulse is shown in Figure 2.9 (c).

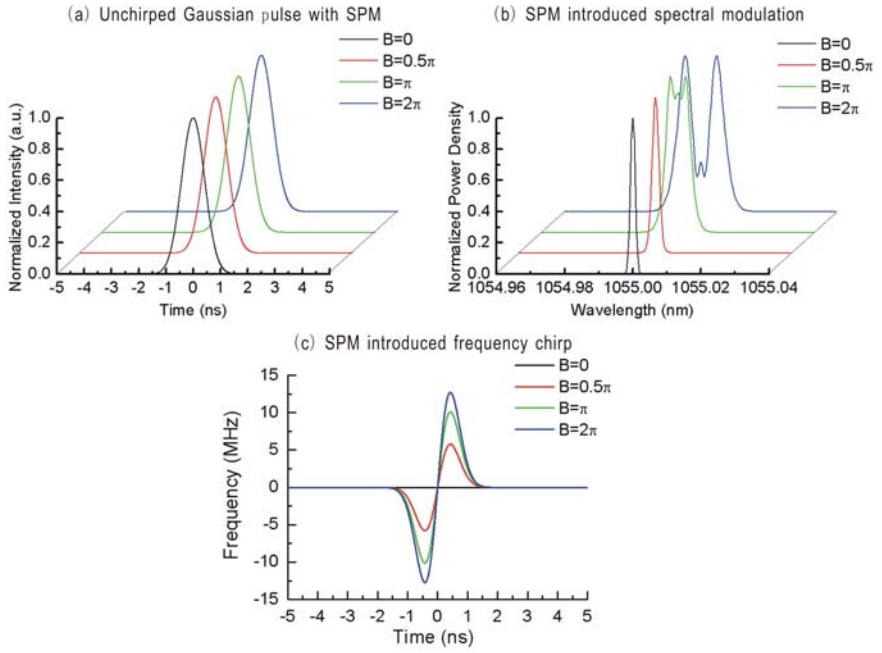

Figure 2.9: The effects of SPM on a Gaussian pulse

2.3.4 Stimulated Raman scattering

SRS originates from the scattering of photons by optical phonons. High power incident light can act as a pump for generating frequency down-shifted radiation through Raman scattering. Once the peak power of the amplified pulses reaches the Raman threshold

(described in the following paragraphs), the generated Stokes wave starts growing rapidly inside the fiber such that most of the pulse energy transfers into the Stokes component after a short propagation distance.

The Raman gain spectrum in silica fiber is very broad, extending up to 30 THz, as shown in Figure 2.10. The first peak of Stokes light in silica fiber is located at the wavelength 13.2 THz from the pump wavelength. The Raman gain peak value is approximately 1×10^{-13}m/W when the pump wavelength is at 1 μm.

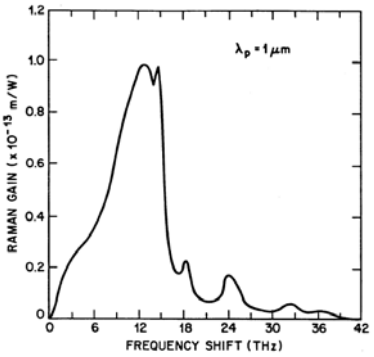

Figure 2.10: Raman gain spectrum for fused silica (from ref.[16])

The pump light intensity, I_p, and Stokes light intensity, I_s, can be described by the following equations

$$\frac{dI_s}{dz} = g_R I_p I_s - \alpha_s I_s \tag{2.23}$$

$$\frac{dI_p}{dz} = -\frac{\omega_p}{\omega_s} g_R I_p I_s - \alpha_p I_p \tag{2.24}$$

where g_R is Raman gain coefficient, and α_s and α_p are the fiber absorption coefficient at the Stokes and pump frequency, respectively.

The Raman threshold is defined as the input pump power at which the Stokes power becomes equal to the pump power at the fiber output, when there is no Stokes light at $z = 0$ and stimulated Raman scattering builds up from the spontaneous Raman scattering. From Equation (2.23) and Equation (2.24), the value of the maximum achievable pulse peak power can be estimated from [33]

$$P_0^{cr} \approx \frac{16 A_{eff}}{g_R L_{eff}} \tag{2.25}$$

For pulses propagating in passive fibers without gain, P_0^{cr} corresponds to the maximum peak power of the input pulse, and $L_{eff} = \left[1 - \exp\left(-\alpha_p L\right)\right]/\alpha_p$, whereas for the case of fiber amplifiers, P_0^{cr} corresponds to the maximum peak power of the output pulse, and $L_{eff} = \left[1 - \exp\left(-gL\right)\right]/g$. For a typical single-mode fiber amplifier with Yb-doped fiber length of ~2 m, gain of ~20 dB, A_{eff} of ~30 μm^2, and signal wavelength at ~1 μm, the predicted Raman threshold is P_0^{cr} ~11 kW, which corresponds to 11 μJ energy for 1 ns pulses. The Raman threshold increases with an increase in the fiber mode area and a decrease in the effective fiber length. The state of the art LMA fiber amplifiers can have Raman thresholds of over 1 MW [1, 3, 34].

Stimulated Brillouin scattering (SBS) can be regarded as scattering from acoustic phonons, which has a lower threshold than SRS for a narrowband CW beam. However, as the Brillouin gain spectrum is extremely narrow, with a bandwidth of ~10 MHz, SBS is not observed for pulses with a broad bandwidth (e.g. bandwidth >8 nm at a central wavelength of 1055 nm), as in all the relevant work in this thesis, and hence will not be discussed in detail.

2.4 Review of prior art

2.4.1 The development of pulse stretcher/compressor components

Gold-coated bulk gratings were first used within the stretcher and compressor in fiber CPA systems for demonstrating the amplification of pulses at low repetition rates. Average powers were limited to the 10 W level when using gold-coated bulk gratings due to their power handling ability.

One of the main advantages of Yb fiber systems is the ability to operate at higher average powers compared with conventional solid-state systems. Therefore, transmission gratings in fused silica, that can handle high average powers, were developed and applied in fiber CPA systems, allowing average output powers of 131 W to be achieved in 2005 [34]. Although such gratings had a high damage threshold, high transmission efficiency, and low absorption which enabled operation at high average power, the size of the grating was limited by the lithographic fabrication technique. As the pulse compression ratio is proportional to the grating dimension, the pulse energy that could be achieved was limited by the compression ratios with fused silica

transmission gratings. In order to achieve both a high average power and a high pulse energy in fiber CPA systems, dielectric gratings need to be used. Besides the advantages of high efficiency and high damage threshold, dielectric gratings can be fabricated in large dimensions which allow for a high stretching and compression ratio. Working with LLNL, we obtained access to the state-of-the-art gratings for our systems.

However, the use of bulk gratings did not comply with the compactness associated with fiber-based laser sources. It is desirable to replace bulk grating arrangements with more compact components. Leveraged by the strong research on optical fiber communication systems, CFBG have become available in recent years and have been successfully implemented in Er-doped fiber CPA systems prior to this research. Early work was focused on the demonstration of all fiber CPA systems by the use of both CFBG based stretchers and compressors [35-38]. However, due to the high pulse intensity at the output of the compressor, the pulse energy of such systems was limited to <1 μJ by nonlinear effects. Later CPA systems with >1 μJ level pulse energies were demonstrated by the use of LMA CFBGs [39], or by the use of a CFBG stretcher with a bulk grating compressor [40]. The ORC had the state-of-the-art facility and techniques required to fabricate CFBGs with accurate control of up to 3rd order dispersion for applications in Yb-doped fiber CPA systems (centre wavelength at ~1 μm). By using an ORC fabricated CFBG stretcher, a Yb-doped fiber CPA system providing a world record combination of high average power and high pulse energy (70 W and 7 μJ, respectively) was demonstrated in this research [41].

Besides CFBGs, research had also been focused on other compact and low cost stretchers and compressors, such as chirped volume Bragg gratings (CVBGs) [42, 43] and air core photonic band-gap fiber (PBGF) [40, 44, 45]. Fiber stretchers with up to 3rd order dispersion compensation of the compressor have been reported recently by incorporating a combination of standard single-mode fibers with anomalous 3rd order dispersion single-mode fibers [46]. The dispersion and the 3rd order dispersion of the fiber stretcher can be managed by adjusting the lengths of the two fibers. Some of these compact components could be useful for high power and high pulse energy systems in future.

2.4.2 Power scaling in CPA systems without nonlinear distortion

The investigation of high pulse energy, fiber CPA system started in the mid 1990s with Er-doped fibers. At the outset of that research, pulses with 100 nJ energies were achieved in a system using a fiber stretcher and a bulk grating compressor [47, 48]. In the

meantime, more compact CPA systems with CFBG stretcher and compressor were demonstrated with 1-20 nJ pulse energies [35-37].

The first breakthrough in the pulse energy scaling was associated with the use of LMA Er-doped fibers and the cladding-pumped technique. A pulse energy of ~10 μJ was achieved in a CPA system using ~16 μm core diameter LMA Er-doped fibers in 1996 [49]. Then pulses with up to 100 μJ energy were reported in Er/Yb-doped LMA fibers in 1997 [50].

Further progress in high power fiber CPA system was associated with the introduction of Yb-doped fiber, due to its advantages as presented in Section 2.2. Figure 2.11 shows a CPA system that was reported in 2001. The system consisted of a fiber-based 1055 nm seed pulse source, a gold coated grating stretcher, a three-stage Yb fiber amplifier chain with two optical gates between the stages and a gold coated grating compressor. The pulses were stretched to 0.8 ns by the stretcher. LMA fiber with 50 μm core diameter was used at the final amplifier stage, and this multi-mode fiber was made possible to guide light dominantly in the fundamental mode by appropriate launching of the input signal [1, 51, 52]. The stretched pulses were amplified to 1.2 mJ energy at the final amplifier stage, and they were compressed to 380 fs with 50% overall efficiency in the compressor [1, 51, 52]. The B-integral of this system was estimated to be above 10π, which indicated that this system was operating with a very high level of SPM distortion. However, this early demonstration has not been repeated by any other research groups, and it was unclear whether the quoted energies in [1, 51] had included corrections required to account for the ASE power in the output signal.

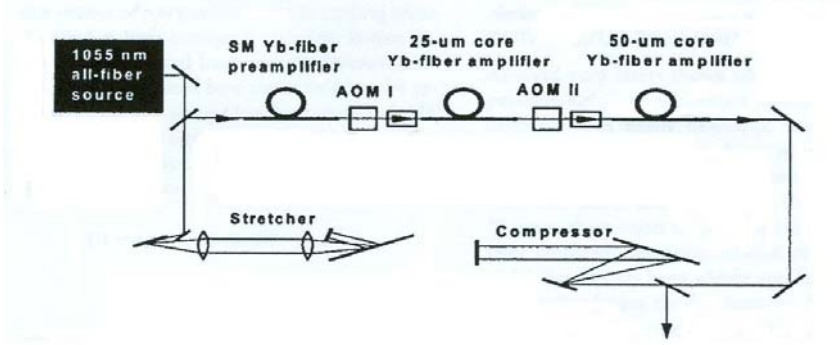

Figure 2.11: Experimental setup of a fiber CPA system from prior art (from ref.[51])

Both grating technology and fiber technology developed rapidly during the course of this thesis work. Current state of the art systems have focused on the use of dielectric gratings and short length, very large mode PCF amplifiers, to achieve >100 W average powers and >1 mJ pulse energies [22].

2.4.3 CPA systems operating with fiber nonlinearity

The increase of the available stretching ratios and the use of fibers with large effective mode area and short device lengths also resulted in an increase in the size and the cost of fiber CPA systems. Therefore, motivated by the development of a compact and low cost system, researchers investigated ways to amplify ultra-short pulses with much more restricted stretching ratios and in the presence of nonlinearity. The designs of a parabolic amplifier, a cubicon amplifier, and a nonlinear CPA are reviewed briefly in this section.

The generation of parabolic pulses in a fiber amplifier was first investigated in 2000 [53]. The analysis of the nonlinear Schrödinger equation showed that, in a fiber with normal dispersion, the interplay of dispersion, nonlinearity and gain would produce a linearly chirped pulse with a parabolic temporal and spectral shape, which could be easily recompressed. As shown in Figure 2.12, the layout of the parabolic amplifier is similar to that of a CPA system, except that no pulse stretcher and a more compact compressor are required [54]. The seed pulses were directly amplified without a stretcher, and the grating compressor was only required to compensate for the dispersion of the amplifier fiber. Pulses with 110 fs duration and 400 nJ energy have been demonstrated using this setup. A system with 240 fs 1.2 μJ output pulses has been reported recently by using PCF and a transmission grating compressor [55]. The calculated B-integral in this setup was about 2π. Further scaling of the pulse energy was limited by the gain bandwidth and SRS effect.

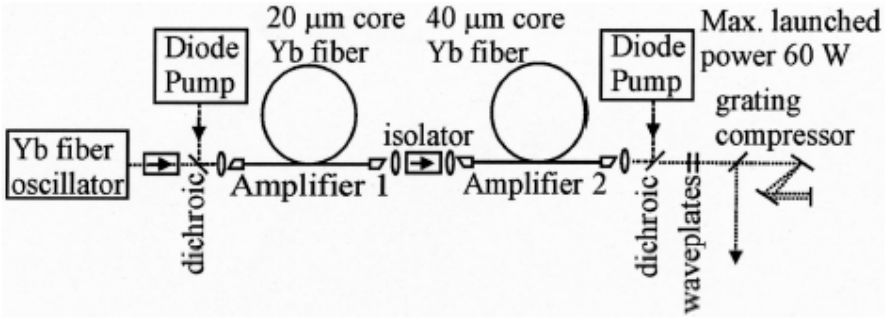

Figure 2.12: Schematic of parabolic pulse amplifier system (from ref.[54])

It was also found that SPM acting on linearly chirped pulses with asymmetric temporal and spectral profiles allowed for the compensation of large values of cubic dispersion mismatch between pulse stretcher and compressor, which was referred to as 'cubicon' amplification. Pulses with 100 μJ energy were obtained using cubicon amplifiers in 2005 [56]. The setup used a fiber stretcher and a bulk grating compressor. The estimated B-integral was ~4π.

Compensation of SPM by residual 3rd order dispersion, with a symmetric spectral profile, was also reported by Zhou et al. [57], in 2005. Compared with cubicon amplifiers, which created an asymmetric spectral profile by means of a filter, pulses in Zhou's setup generated a symmetric nonlinear phase shift during amplification, and the compensation was realized by exploiting the interplay between SPM and 3rd order dispersion. Following Zhou's work and the development of numerical models for such nonlinear CPA systems [58], Kuznetsova [59] demonstrated, in 2007, 30 μJ pulses (before compression) in fiber CPA systems with a nonlinear phase shift of up to 17 π. Most recently, ~100 μJ pulses with B-integral of ~5.5π were reported in a system incorporating both a fiber and a grating stretcher, 80 μm core diameter rod-type PCF, and a bulk grating compressor [60].

2.5 Conclusion

This chapter reviewed the history of the development of high power fiber CPA systems, as well as the key technologies developed both before and during this thesis research. This review also provided background on the various state of the art technologies that were applied in this thesis research.

Nonlinear effects are the fundamental limitation to short pulse amplification in optical fibers. This chapter reviewed the theory of pulse propagation in fibers and the main nonlinear effects limiting the power scaling of short pulse systems. The experimental observation of SPM induced pulse distortions will be presented in chapters 5 and 6.

The development of numerical models for Yb-doped fibers will be presented in Chapter 3. The experimental development of fiber CPA systems, consisting of different components and targeted at different goals, will be presented in Chapters 5 and 6.

References

[1] A. Galvanauskas, "Mode-scalable fiber-based chirped pulse amplification systems," *IEEE Journal of Selected Topics in Quantum Electronics*, vol. 7, pp. 504-517, 2001.

[2] J. H. V. Price, A.Malinowski, A.Piper, F.He, W.Belardi, T.M.Monro, M.Ibsen, B.C.Thomsen, Y.Jeong, C.Codemard, M.A.F.Roelens, P.Dupriez, J.K.Sahu, J.Nilsson, and D.J.Richardson, "Advances in high power short pulse fiber laser systems and technology," in *Photonics West*. San Jose Optical Society of America, 2005, 5709-30 (Invited).

[3] J. Limpert, F. Roser, T. Schreiber, and A. Tunnermann, "High-power ultrafast fiber laser systems," *IEEE Journal of Selected Topics in Quantum Electronics*, vol. 12, pp. 233-244, 2006.

[4] D. Strickland and G. Mourou, "Compression Of Amplified Chirped Optical Pulses," *Optics Communications*, vol. 56, pp. 219-221, 1985.

[5] C. N. Danson, P. A. Brummitt, R. J. Clarke, J. L. Collier, B. Fell, A. J. Frackiewicz, S. Hancock, S. Hawkes, C. Hernandez-Gomez, P. Holligan, M. H. R. Hutchinson, W. J. L. A. Kidd, I. O. Musgrave, D. Neely, D. R. Neville, P. A. Norreys, D. A. Pepler, C. J. Reason, W. Shaikh, T.B.Winstone, R. W. W. Wyatt, and B.E.Wyborn, "Vulcan Petawatt -an ultra high intensity interaction facility," *Nuclear Fusion*, vol. 44, pp. S239-S246, 2004.

[6] C. P. J. Barty, M. Key, J. Britten, R. Beach, G. Beer, C. Brown, S. Bryan, J. Caird, T. Carlson, J. Crane, J. Dawson, A. C. Erlandson, D. Fittinghoff, M. Hermann, C. Hoaglan, A. Iyer, L. J. II, I. Jovanovic, A. Komashko, O. Landen, Z. Liao, W. Molander, S. Mitchell, E. Moses, N. Nielsen, H.-H. Nguyen, J. Nissen, S. Payne, D. Pennington, L. Risinger, M. Rushford, K. Skulina, M. Spaeth, B. Stuart, G. Tietbohl, and B. Wattellier, "An overview of LLNL high-energy short-pulse technology for advanced radiography of laser fusion experiments," *Nuclear Fusion*, vol. 44, pp. S266-S275, 2004.

[7] E. Snitzer, "Optical maser action of Nd^{3+} in a barium crown glass," *Physical Review Letters*, vol. 7, pp. 444, 1961.

[8] S.B.Poole, D.N.Payne, and M.E.Fermann, "Fabrication of low loss ptical fibres containing rare earth ions," *Electronics Letters*, vol. 21, pp. 737-738, 1985.

[9] H. M. Pask, R. J. Carman, D. C. Hanna, A. C. Tropper, C. J. Mackechnie, P. R. Barber, and J. M. Dawes, "Ytterbium-Doped Silica Fiber Lasers - Versatile Sources for the 1-1.2 um Region," *IEEE Journal of Selected Topics in Quantum Electronics*, vol. 1, pp. 2-13, 1995.

[10] M. J. F. Digonnet, *Rare-Earth-Doped Fiber Lasers and Amplifiers*, 2nd ed, 2001.

[11] R. Paschotta, J. Nilsson, A. C. Tropper, and D. C. Hanna, "Ytterbium-doped fiber amplifiers," *IEEE Journal of Quantum Electronics*, vol. 33, pp. 1049-1056, 1997.

[12] M. K. Davis, M. J. F. Digonnet, and R. H. Pantell, "Thermal effects in doped fibers," *Journal of Lightwave Technology*, vol. 16, pp. 1013-1023, 1998.

[13] D. Kouznetsov, J. V. Moloney, and E. M. Wright, "Efficiency of pump absorption in double-clad fiber amplifiers. I. Fiber with circular symmetry," *Journal of the Optical Society of America B-Optical Physics*, vol. 18, pp. 743-749, 2001.

[14] D. Kouznetsov and J. V. Moloney, "Efficiency of pump absorption in double-clad fiber amplifiers. II. Broken circular symmetry," *Journal of the Optical Society of America B-Optical Physics*, vol. 19, pp. 1259-1263, 2002.

[15] D. Kouznetsov and J. V. Moloney, "Efficiency of pump absorption in double-clad fiber amplifiers. III. Calculation of modes," *Journal of the Optical Society of America B-Optical Physics*, vol. 19, pp. 1304-1309, 2002.

[16] G. P. Agrawal, *Nonlinear Fiber Optics*, 3rd ed. San Diego: Academic Press, 2001.

[17] A. W. Snyder and J. Love, *Optical Waveguide Theory*: Springer, 1983.

[18] J. Senior, *Optical Fiber Communications*, 2nd ed. New York Prentice Hall 1992.

[19] K. Okamoto, *Fundamentals of optical waveguides*: Academic Press, 2000.

[20] J. Limpert, A. Liem, M. Reich, T. Schreiber, S. Nolte, H. Zellmer, A. Tunnermann, J. Broeng, A. Petersson, and C. Jakobsen, "Low-nonlinearity single-transverse-mode ytterbium-doped photonic crystal fiber amplifier," *Optics Express*, vol. 12, pp. 1313-1319, 2004.

[21] F. Röser, D. Schimpf, O. Schmidt, B. Ortac, K. Rademaker, J. Limpert, and A. Tunnermann, "90 W average power 100 uJ energy femtosecond fiber chirped-pulse amplification system," *Optics Letters*, vol. 32, pp. 2230-2232, 2007.

[22] F. Röser, T. Eidam, J. Rothhardt, O. Schmidt, D. N. Schimpf, J. Limpert, and A. Tünnermann, "Millijoule pulse energy high repetition rate femtosecond fiber chirped-pulse amplification system," *Optics Letters*, vol. 32, pp. 3495-3497, 2007.

[23] J. C. Knight, T. A. Birks, R. F. Cregan, P. S. Russell, and J. P. de Sandro, "Large mode area photonic crystal fibre," *Electronics Letters*, vol. 34, pp. 1347-1348, 1998.

[24] N. A. Mortensen and J. R. Folkenberg, "Low-loss criterion and effective area considerations for photonic crystal fibres," *Journal of Optics A-Pure and Applied Optics*, vol. 5, pp. 163-167, 2003.

[25] P. Russell, "Photonic Crystal Fibers " *Science*, vol. 299, pp. 358-362, 2003.

[26] K. P. Hansen and J. Broeng, "High-power photonic crystal fiber lasers," *Photonics Spectra*, vol. 40, pp. 82, 2006.

[27] T. A. Birks, J. C. Knight, and P. S. Russell, "Endlessly single-mode photonic crystal fiber," *Optics Letters*, vol. 22, pp. 961-963, 1997.

[28] J. Limpert, N. D. Robin, I. Manek-Honninger, F. Salin, F. Roser, A. Liem, T. Schreiber, S. Nolte, H. Zellmer, A. Tunnermann, J. Broeng, A. Petersson, and C. Jakobsen, "High-power rod-type photonic crystal fiber laser," *Optics Express*, vol. 13, pp. 1055-1058, 2005.

[29] www.Crystal-Fibre.com, "Double Clad High NA Yb Fiber Data Sheet – DC·200·70·PM·Yb·rod," 2007.

[30] ISO_Standard_11146, "Lasers and laser related equipment -Test methods for laser beam widths, divergence angles and beam propagation ratios," 2005.

[31] E. Marcatili, "Improved Coupled-Mode Equations for Dielectric Guides," *IEEE Journal of Quantum Electronics*, vol. 22, pp. 988-993, 1986.

[32] M. D. Perry, T. Ditmire, and B. C. Stuart, "Self-Phase Modulation in Chirped-Pulse Amplification," *Optics Letters*, vol. 19, pp. 2149-2151, 1994.

[33] R. G. Smith, "Optical Power Handling Capacity of Low Loss Optical Fibers as Determined by Stimulated Raman and Brillouin-Scattering," *Applied Optics*, vol. 11, pp. 2489, 1972.

[34] F. Röser, J. Rothhard, B. Ortac, A. Liem, O. Schmidt, T. Schreiber, J. Limpert, and A. Tunnermann, "131 W 220 fs fiber laser system," *Optics Letters*, vol. 30, pp. 2754-2756, 2005.

[35] A. Galvanauskas, M. E. Fermann, D. Harter, K. Sugden, and I. Bennion, "All-fiber femtosecond pulse amplification circuit using chirped Bragg gratings," *Applied Physics Letters*, vol. 66, pp. 1053-1055, 1995.

[36] A. Boskovic, M. J. Guy, S. V. Chernikov, J. R. Taylor, and R. Kashyap, "All-fibre diode pumped, femtosecond chirped pulse amplification system," *Electronics Letters*, vol. 31, pp. 877-879, 1995.

[37] J. D. Minelly, A. Galvanauskas, M. E. Fermann, D. Harter, J. E. Caplen, Z. J. Chen, and D. N. Payne, "Femtosecond pulse amplification in cladding-pumped fibers," *Optics Letters*, vol. 20, pp. 1797-1798, 1995.

[38] A. Galvanauskas, P. A. Krug, and D. Harter, "Nanosecond-to-picosecond pulse compression with fiber gratings in a compact fiber-based chirped-pulse-amplification system," *Optics Letters*, vol. 21, pp. 1049-1051, 1996.

[39] N. G. R. Broderick, D. J. Richardson, D. Taverner, J. E. Caplen, L. Dong, and M. Ibsen, "High-power chirped-pulse all-fiber amplification system based on large-mode-area fiber gratings," *Optics Letters*, vol. 24, pp. 566-568, 1999.

[40] G. Imeshev, I. Hartl, and M. E. Fermann, "Chirped pulse amplification with a nonlinearly chirped fiber Bragg grating matched to the Treacy compressor," *Optics Letters*, vol. 29, pp. 679-681, 2004.

[41] F. He, J. H. V. Price, A. Malinowski, A. Piper, M. Ibsen, and D. J. Richardson, "High Average Power, High Energy, Femto-second Fiber Chirped Pulse Amplification System," presented at Conference on Lasers and Electro-Optics, Baltimore, 2007, CMEE5.

[42] K. H. Liao, K. C. Hou, G. Chang, V. Smirnov, L. Glebov, R. Changkakoti, P. Mamidipudi, and A. Galvanauskas, "Diffraction-Limited 65-μm Core Yb-doped LMA Fiber based High Energy Fiber CPA

Systems," presented at Conference on Lasers and Electro-Optics, Long Beach, 2006, CPDB4.

[43] G. Chang, C. H. Liu, K. H. Liao, V. Smirnov, L. Glebov, and A. Galvanauskas, "50-W Chirped-Volume-Bragg-Grating Based Fiber CPA at 1055-nm," presented at Conference on Lasers and Electro-Optics, Baltimore, 2007, CMEE4.

[44] J. Limpert, T. Schreiber, S. Nolte, H. Zellmer, and A. Tunnermann, "All fiber chirped-pulse amplification system based on compression in air-guiding photonic bandgap fiber," *Optics Express*, vol. 11, pp. 3332-3337, 2003.

[45] G. Imeshev, I. Hartl, and M. E. Fermann, "An optimized Er gain band all-fiber chirped pulse amplification system," *Optics Express*, vol. 12, pp. 6508-6514, 2004.

[46] I. Hartl, T. R. Schibli, A. Marcinkevicius, D. C. Yost, D. D. Hudson, M. E. Fermann, and J. Ye, "Cavity-enhanced similariton Yb-fiber laser frequency comb: 3×10^{14} W/cm^2 peak intensity at 136 MHz," *Optics Letters*, vol. 32, pp. 2870-2873, 2007.

[47] A. Galvanauskas, M. E. Fermann, and D. Harter, "High-power amplification of femtosecond optical pulses in a diode-pumped fiber system," *Optics Letters*, vol. 19, pp. 1201-1203, 1994.

[48] M. E. Fermann, A. Galvanauskas, and D. Harter, "All-fiber source of 100-nJ subpicosecond pulses," *Applied Physics Letters*, vol. 64, pp. 1315-1317, 1994.

[49] D. Taverner, A.Galvanauskas, D.Harter, D.J.Richardson, and L.Dong, "Generation of high energy pulses using a large mode area erbium doped fibre amplifier," *Technological Digest of Conference on Lasers and Electro-Optics*, pp. 102-104, 1996.

[50] J. D. Minelly, A. Galvanauskas, D. Harter, J. E. Caplen, and L. Dong, "Cladding-pumped fiber laser/amplifier system generating 100 uJ energy picosecond pulses," presented at Conference on Lasers and Electro-Optics, Baltimore, 1997.

[51] A. Galvanauskas, Z. Sartania, and M. Bischoff, "Millijoule femtosecond all-fiber system," presented at Conference on Lasers and Electro-Optics, Baltimore, 2001, paper CMA1.

[52] M. E. Fermann, A. Galvanauskas, and G. Sucha, *Ultrafast lasers : technology and applications*. New York: Marcel Dekker, 2003.

[53] M. E. Fermann, V. I. Kruglov, B. C. Thomsen, J. M. Dudley, and J. D. Harvey, "Self-similar propagation and amplification of parabolic pulses in optical fibers," *Physical Review Letters*, vol. 84, pp. 6010-6013, 2000.

[54] A. Malinowski, A. Piper, J. H. V. Price, K. Furusawa, Y. Jeong, J. Nilsson, and D. J. Richardson, "Ultrashort-pulse Yb^{3+}-fiber-based laser and amplifier system producing >25W average power," *Optics Letters*, vol. 29, pp. 2073-2075, 2004.

[55] T. Schreiber, C. K. Nielsen, B. Ortac, and J. Limpert, "Microjoule-level all-polarization-maintaining femtosecond fiber source," *Optics Letters*, vol. 31, pp. 574-576, 2006.

[56] L. Shah, Z. L. Liu, I. Hartl, G. Imeshev, G. C. Cho, and M. E. Fermann, "High energy femtosecond Yb cubicon fiber amplifier," *Optics Express*, vol. 13, pp. 4717-4722, 2005.

[57] S. Zhou, L. Kuznetsova, A. Chong, and F. W. Wise, "Compensation of nonlinear phase shifts with third-order dispersion in short-pulse fiber amplifiers," *Optics Express*, vol. 13, pp. 4869-4877, 2005.

[58] A. Chong, L. Kuznetsova, and F. W. Wise, "Theoretical optimization of nonlinear chirped-pulse fiber amplifiers," *Journal of the Optical Society of America B-Optical Physics*, vol. 24, pp. 1815-1823, 2007.

[59] L. Kuznetsova and F. W. Wise, "Scaling of femtosecond Yb-doped fiber amplifiers to tens of microjoule pulse energy via nonlinear chirped pulse amplification," *Optics Letters*, vol. 32, pp. 2671-2673, 2007.

[60] Y. Zaouter, J. Boullet, E. Mottay, and E. Cormier, "Transform-limited 100 μJ, 340 MW pulses from a nonlinear-fiber chirped-pulse amplifier using a mismatched grating stretcher-compressor," *Optics Letters*, vol. 33, pp. 1527-1529, 2008.

Chapter 3 Optimization of cascaded Yb-doped fiber amplifiers using numerical models

This chapter describes the development of numerical models that can reliably predict and optimize the performance of Yb-doped fiber amplifiers for application in high power CPA systems. In order to demonstrate the utility and accuracy of the modeling tool, as well as the complexity of the systems and amplifier properties that can be successfully modeled, this chapter presents a comparison of experimental and theoretical results for single-stage core- and cladding-pumped amplifiers and also for a multi-stage amplifier chain CPA system that is optimized to provide a broad gain bandwidth.

The chapter is organized as follows. Section 3.1 presents the motivation for, and the difficulties associated with, the development of numerical models for Yb-doped fibers. Section 3.2 describes the standard rate and propagation equations used to calculate the laser population inversion along the fiber length under steady state conditions. This section outlines the physically justifiable simplifications used in order to increase the computational efficiency. This model does not consider dynamic gain variation, and this aspect is considered separately in Appendix I. In order to apply the model to a wide variety of amplifiers, Section 3.3 shows details of the Yb-spectroscopy for two host-glass compositions relevant to this thesis, and the methods that I use to measure and calculate the cross-section data. To benchmark the accuracy of the steady state model, Section 3.4 considers single stage amplifiers with a narrow-line signal and a core-pumped amplifier. A key benefit of the modeling approach is the ability to simulate more complex amplifiers and Section 3.4 also shows results for a bi-directionally pumped cladding-pumped fiber with both a broad bandwidth signal, and a broad bandwidth pump. Having established the reliability of the simulations for single amplifiers, I then exploit the full power of the modeling tool to include coupling components, configured within cascaded amplifiers in CPA systems, where maximizing the gain-bandwidth is essential for obtaining the shortest possible pulses at the system output [1]. A gain-bandwidth optimized system operation at high repetition rates, where nonlinear effects are not significant, is first designed. Then simulations are performed to re-design the system for

operating at lower repetition rates and increased pulse energies, where gain efficiency is compromised slightly in order to minimize the nonlinear effects. Section 3.5 shows the simulation and experimental results for the CPA system. Section 3.6 contains discussions and conclusions.

3.1 Introduction

With their special properties, as presented in Chapter 2, Yb-doped fiber lasers and amplifiers are being increasingly recognized as the preferred high power sources for many industrial and scientific applications. Research on such laser systems is progressing rapidly. For example, high average power single transverse mode Yb-doped fiber lasers are now producing >6 kW in a CW format [2], and >320 W in a 20 ps pulsed MOPA configuration [3].

These achievements might give the impression that Yb-doped fiber laser technology has reached a high level of maturity and that constructing Yb-systems is a straightforward process. However, it has to be appreciated that Yb-doped fiber amplifiers are in fact quite difficult to design and optimize in practice due to the three-level nature of the Yb-system which causes the wavelength dependent gain profile to vary significantly depending on the interplay of pump and signal power, wavelength, amplifier length, and pump configuration. In order to accurately model the gain and basic characteristics of even a single Yb-fiber amplifier it is necessary to use numerical simulations to solve for the population inversion along the fiber length. This problem is further compounded when moving from the optimization of a single amplifier to the optimization of the cascaded fiber amplifier chains used in CPA systems to amplify the output from a mode-locked seed laser to high powers. In these circumstances, existing experimental and numerical approaches soon become too complex for all but the most experienced researchers. The development and availability of proven numerical modeling tools with a flexible, user-friendly, interface would thus be of immediate benefit to this thesis research, and also to other researchers in this new laser technology who may not have extensive experience in creating computationally efficient numerical models.

To address this need, I demonstrate that highly accurate simulation results for complex Yb-fiber amplifier systems can be obtained by leveraging EDFA models and commercial design tools which have previously been developed for telecommunications systems (see, e.g., [4]). Specifically, I have used a commercially produced graphical user interface

modeling tool from "VPI systems". Following my initial research [5], a module allowing for modeling of Yb amplifiers was released by VPI systems Inc. in 2004, which should allow ready access to this powerful tool to the wider research community.

3.2 Steady-state numerical model

The model of Giles and Desurvire [6, 7] is useful for optimizing the steady-state amplifier gain spectrum. This model is applicable to single-mode fibers, and approximates the transverse inversion as a flat-top profile by replacing the full radial dependence of the inversion with effective overlap integrals for signal and pump [7], and the model is available as a "standard" module in the VPI (quasi-three-level) modeling tool. The rate and propagation equations for a homogeneously broadened two-level system are shown below.

$$\frac{\partial N_2(t,z)}{\partial t} = \left[R_{12}(\lambda) + W_{12}(\lambda)\right] N_1(t,z) - \left[R_{21}(\lambda) + W_{21}(\lambda) + A_{21}\right] N_2(t,z) \tag{3.1}$$

$$\pm \frac{dP_p^{\pm}(\lambda,z)}{dz} = \Gamma_p(\lambda)\left[\sigma_e(\lambda) N_2(z) - \sigma_a(\lambda) N_1(z)\right] \rho P_p^{\pm}(\lambda,z) - \alpha_p P_p^{\pm}(\lambda,z) \tag{3.2}$$

$$\frac{dP_s(\lambda,z)}{dz} = \Gamma_s(\lambda)\left[\sigma_e(\lambda) N_2(z) - \sigma_a(\lambda) N_1(z)\right] \rho P_s(\lambda,z) - \alpha_s P_s(\lambda,z) \tag{3.3}$$

$$\begin{aligned} \pm \frac{dP_a^{\pm}(\lambda,z)}{dz} = {} & \Gamma_s(\lambda)\left[\sigma_e(\lambda) N_2(z) - \sigma_a(\lambda) N_1(z)\right] \rho P_a^{\pm}(\lambda,z) - \alpha_s P_a^{\pm}(\lambda,z) \\ & + 2\Gamma_s(\lambda)\sigma_e(\lambda) N_2(z) \rho h \upsilon_s \Delta\upsilon \end{aligned} \tag{3.4}$$

where P_s, P_p and P_a represent signal, pump and ASE power, respectively (± indicates the forward and backward directions); N_2 is the excited ion fraction; and. Γ_s and Γ_p are signal and pump mode overlap factors; the emission and absorption cross-sections are σ_e and σ_a; ρ is the ion density; and α_s, α_p represent internal loss of the amplifier for signal and pump. The spontaneous decay rate from level 2 to 1 is given by $A_{21} = \tau_{21}^{-1}$, where the characteristic fluorescence lifetime is τ_{21}. The stimulated emission rate and pumping rate, are $W_{ij} = \Gamma_S(\lambda)\sigma_{e,a}\left(P_S + P_a^+ + P_a^-\right)/h\upsilon_S A$ and $R_{ij} = \Gamma_p(\lambda)\sigma_{e,a}\left(P_p^+ + P_p^-\right)/h\upsilon_p A$ respectively. A is the fiber core area and $\Delta\upsilon$ is the amplifier homogeneous bandwidth for both polarization states.

The model imposes the steady-state condition by setting $\partial N_2(t,z)/\partial t = 0$, and then uses the conservation condition that $N_1 + N_2 = 1$ to solve for the inversion fraction at a

given position. The model then integrates the propagation equations along the amplifier using standard numerical techniques to enable the inversion fraction to be solved at each point. The light in the amplifier is considered as a number of discrete optical beams of frequency bandwidth $\Delta\upsilon_k$ centred at the optical wavelength $\lambda_k = c/\upsilon_k$, where $\Delta\upsilon_k$ equals the frequency resolution of the model. This notation describes both narrow line signals and broadband ASE. Integration over optical frequency thus becomes a summation over the index, k.

3.3 Spectroscopic data for the Yb-doped fibers

The variation of the cross-sections with host glass compositions can be significant and it is essential to use the appropriate cross-sections relevant to the particular glass host used within the fiber core, this will be highlighted in section 3.4. Figure 3.1 (b) shows the cross-section spectra of Yb/Al silicate fiber, published by Paschotta *et al.* [8]. Figure 3.1 (a) shows the measured cross-sections of the Yb/P/Al silicate fiber used in the core-pumped amplifiers and, using this data, good agreement with experimental results is obtained, as will be shown in the following sections. For simulating the Yb/Al silicate LMA fiber and PCFs used in the cladding-pumped amplifiers, cross-section data similar to Figure 3.1 (b) is used and good agreement with experimental data is obtained, as will be shown in the following sections.

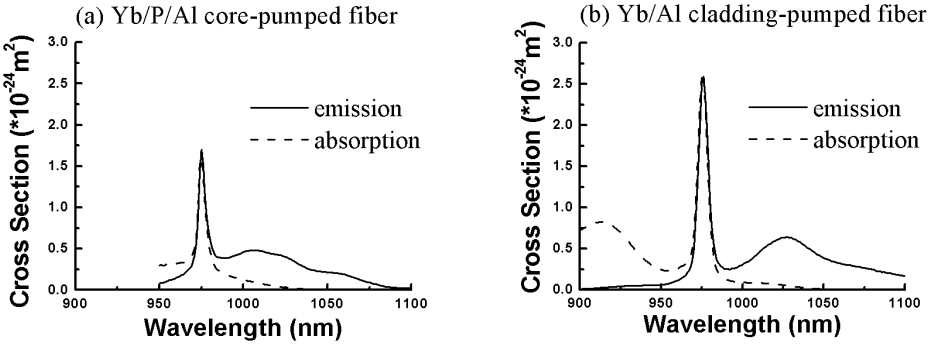

Figure 3.1: Yb absorption and emission cross-section data for different host-glass compositions

The cross-sections of the Yb/P/Al silicate fiber (Figure 3.1 (a)) are measured and calculated using the facilities at the ORC. This work starts with the measurement of the fluorescence spectra, the fluorescence lifetime and the absorption spectra. The fluorescence spectra and lifetime are measured in the experimental setup as shown in Figure 3.2. The 915 nm laser beam from a laser diode is reflected by a 915 nm high reflection and 975 nm high transmission dichroic mirror to 8 cm of the Yb/P/Al silicate

fiber. Both ends of the fiber are angle-cleaved. The backward fluorescence generated from the fiber is transmitted through the dichroic mirror and then collected by the Optical Spectrum Analyzer (OSA). Note that the fluorescence spectra are also measured from the side of the fiber. The side fluorescence measurement is believed to have less distortion from ASE. Both measurement methods provide similar fluorescence spectral shapes. The measurement method shown in Figure 3.2 is however preferred as it can provide more signal than the side measurement.

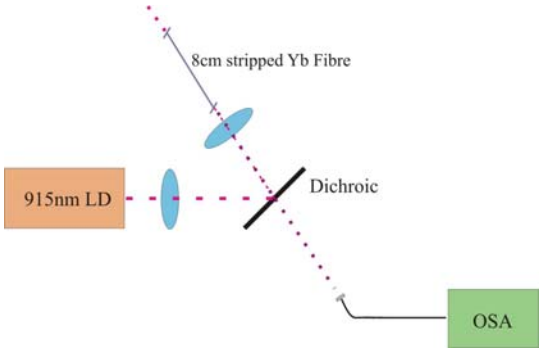

Figure 3.2: Schematic of fluorescence spectrum and lifetime measurement

The fluorescence lifetime is also measured in the setup shown in Figure 3.2, by modulating the pump laser to a 4 ms pulse width at the repetition rate of 30 Hz. The fluorescence is collected by a photodiode, instead of the OSA. Figure 3.3 shows an example of the pulse shape on the oscilloscope. A tail in the pulse is observed, which represents the fluorescence of the fiber. The lifetime can be calculated from the pulse tail and is defined by when the fluorescence has decayed to $1/e$ of its maximum. The lifetime of our Yb/P/Al silicate fiber was measured to be 1.40 ±0.05 ms.

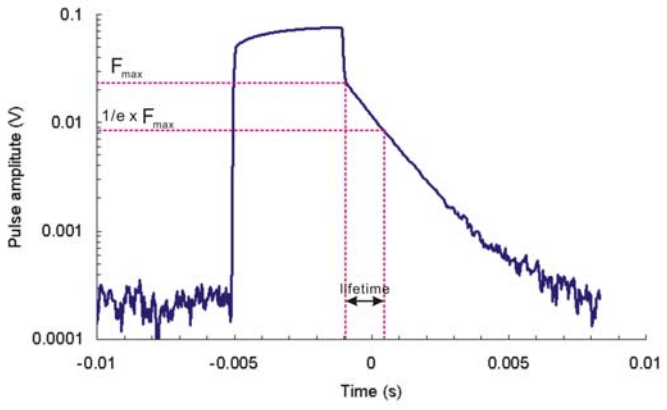

Figure 3.3: Fluorescence lifetime calculation

The absorption spectrum is measured by using the cut-back technique [4, 9]. In this method, it is critical to maintain the measurement environment during the cut-back of the

fiber. Therefore, two pieces of ~0.5 m long passive single-mode fibers are used to fix the launching conditions of white light source and the OSA, as shown in Figure 3.4. The cut-back takes place by breaking the splice between the Yb-doped fiber and the passive fiber. As the splicing of single-mode fiber has become relatively repeatable and reliable with the development of commercial splicers, the re-splice contributes ±0.1 dB error into the output spectra. The white light source contributes 0.07 dB noise when the OSA is set to 1 nm resolution and the highest sensitivity, which is the configuration used for all the absorption spectra measurements.

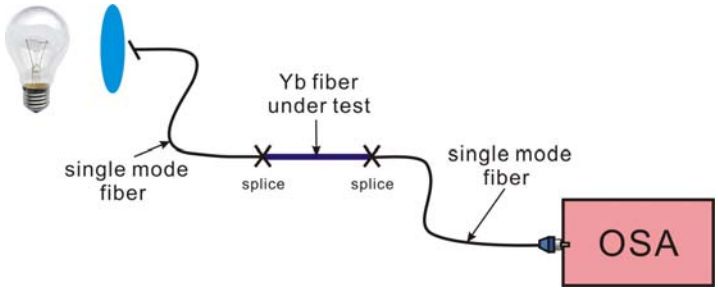

Figure 3.4: Absorption spectrum measurement

The absorption peak (~1200 dB/m at 975 nm) of the Yb-fiber is difficult to measure due to the sensitivity limitations of the OSA (noise floor for 1 nm resolution is -60 dBm/nm) and the relatively low brightness of the white light source (-40 dBm/nm after being launched into the passive fiber). Therefore, to measure the 975 nm absorption peak, a diode laser source is used, providing strong signals from 950 nm to 990 nm, instead of the white light source. The absorption spectrum is a combination of the results from the two measurements.

There is no standard method that has been defined for the cross-section calculations. The most commonly used method is the Fuchtbauer-Landenberg (F-L) equation:

$$\sigma_{a,e}(\lambda) = \frac{\lambda^5 I_{a,e}(\lambda)}{8\pi c n^2 \tau \int \lambda I_{a,e}(\lambda) d\lambda} \tag{3.5}$$

where n is the medium refractive index, τ is the fluorescence lifetime and $I_{a,e}(\lambda)$ is the absorption or fluorescence spectrum [10].

The F-L relation comes from Einstein's theory for two-level laser systems and is related only to the fluorescence and absorption spectral shapes and the fluorescence lifetime [11]. This relation is valid for rare-earth ions only if all components of the two levels are equally populated, or all the transitions have the same strength regardless of the components involved. However, none of the above requirements is satisfied for Er [12]. Therefore, it is not surprising to see that the F-L method is reported to have low

accuracy for the emission cross-section and that the value of the calculated absorption/emission cross-section ratio of Er-fiber disagrees with the experimental measurement [11-13]. As it is also a rare-earth ion, Yb is expected to have the same problem as Er although this has not been reported yet.

Provided that one of the (either emission or absorption) cross-sections is available, the other cross-section data can be calculated by using McCumber theory. McCumber theory was reported to have high accuracy (within 3%) for Er cross-section calculations, under the condition that the electronic structure of the Stark sublevels is known [10]. The only assumption required by the McCumber theory is that the time needed to establish a thermal distribution within each manifold be short compared with the lifetime of that manifold. According to the McCumber theory, the absorption and emission cross-sections are then related by:

$$\sigma_e(\lambda) = \sigma_a(\lambda) \exp\left[\left(\varepsilon - \frac{hc}{\lambda}\right) / kT\right] \tag{3.6}$$

where ε is the temperature-dependent excitation energy [14].

The value of ε can be calculated if all the sublevel energies of Yb in the host glass are known. However, as these energies are very difficult to measure, this kind of measurement has only been reported for a few glass types, and often only a partial Stark sublevel diagram could be reconstructed [15]. Miniscalco proposed an 'Approximate McCumber Method' (AMCM), that obviates the need for all the sublevel energies to be specified, in 1991 [12]. This method has been used in our calculation, which assumes that the emission and absorption cross-sections are equal at the 975 nm peak:

$$\varepsilon = \frac{hc}{\lambda_c} = \frac{hc}{975nm} \tag{3.7}$$

However, in 2002 Digonnet demonstrated that this method tends to overestimate the peak cross-section by up to 75% and predicted an emission spectrum that is erroneously depressed in the S band and inflated in the C and L bands for Er-doped glass [15].

In my approach, I first calculate the absorption and emission cross-section data by using the F-L equation (Equation (3.5)). The calculated peak value of the absorption cross-section can be inaccurate because the measurement of the absorption spectra below 950 nm is limited by the cut-off wavelength of the passive single-mode fibers used in the measurement. However, as the relative shape of the absorption cross-section data is still valid, I normalize the absorption cross-section data to the emission cross-section data at the 975 nm peak. In the meanwhile, AMCM is also used to predict the absorption cross-section data by using the emission cross-section data. Figure 3.5 shows the comparison

of the data from the two methods. The good agreement between the F-L calculation (normalization from experimentally measured absorption spectra) and the McCumber calculation (theoretical prediction from emission cross-section data) confirms the accuracy of my measurements. The absorption data from the normalized F-L calculation are used to obtain the simulation results presented in this thesis, as in general it provides simulation results that are in relatively closer agreement to the experimental results than the simulation results using the absorption data from AMCM.

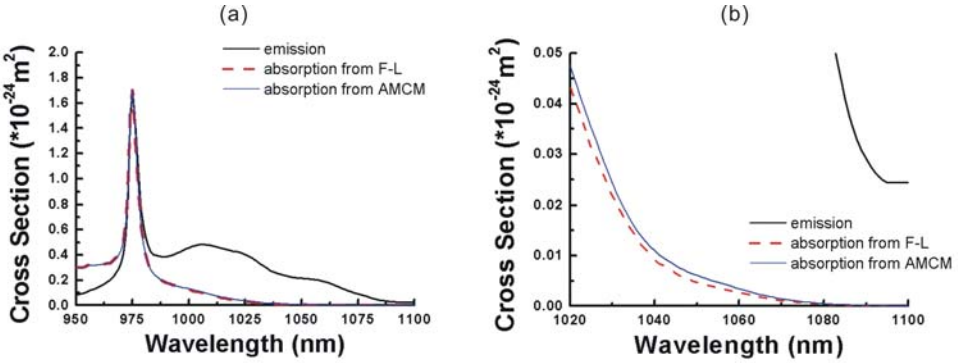

Figure 3.5: Calculated cross-section data. (a) full scale, (b) zoomed scale

3.4 Single-stage amplifier results

3.4.1 Test against other proven models

According to the manuals, the EDFA model in the VPI software uses the same equations as described in section 3.2, but some of the input parameters to the model are limited to the EDFA wavelength range (1.3~1.5 μm). Therefore, upon our request, VPI provided us with a revised EDFA model without any imposed limitations on the wavelength. The revised model has been successfully applied in the simulation of Yb-doped fiber amplifiers, as described in the following sections. Note that with our feedback, and its own investigations, VPI released a new commercial Yb-doped fiber amplifier model package in 2004.

Initial tests of the VPI model were performed by comparing it with another Yb-doped fiber amplifier model that was published in [8]. Figure 3.6 shows an example of the good agreement between the results from the VPI model and the published model. The left graph in Figure 3.6 shows the simulated gain (in dB/m) versus wavelength from the published paper, and the right graph in Figure 3.6 shows the results from the VPI model using the simulation parameters provided in the paper.

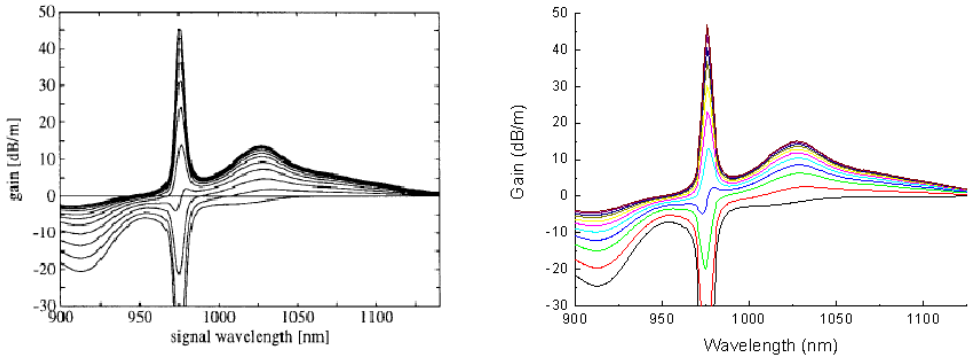

Figure 3.6: Calculated gain spectra for an Yb/Al silicate fiber for different 910 nm pump powers (in intervals of 3 mW, from 0 to 30 mW). (Left: modelling results from [8]; Right: modelling results from the developed model.)

3.4.2 Core pumped amplifier results

The modeling benchmark of my system starts from a low power, core-pumped, Yb/P/Al silicate fiber amplifier. In this case both signal and pump have a similar mode overlap with the Yb-doped core. As shown in Figure 3.7, the amplifier is a 4 m length of single mode Yb/P/Al silicate fiber, pumped with a grating-stabilized, 976.3 nm, fiber pigtailed laser diode with 280 mW output power. A 1060 nm narrow-bandwidth distributed-feedback (DFB) laser is used as the input signal.

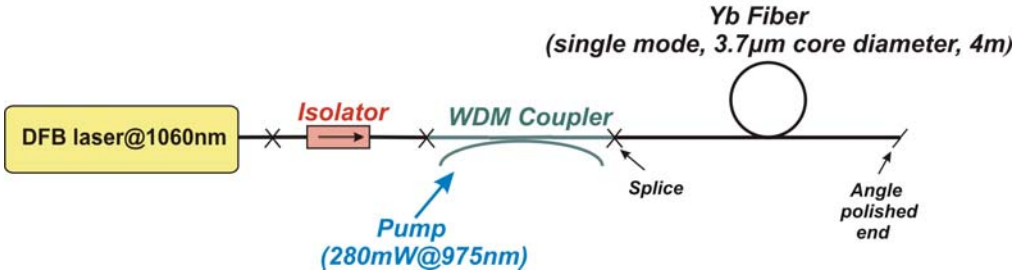

Figure 3.7: Schematic of core-pumped amplifier

The simulation parameters are shown in Table 3.1. The pump and signal wavelengths, fiber length, and spectroscopic data (Figure 3.1 (a)), are measured values. The core diameter and NA are calculated from the refractive index profile of the fiber preform, and the overlap factors are then calculated using numerical integration by assuming idealized modes for an equivalent step-index fiber with Yb-doping extending uniformly across the entire core. The background loss is estimated according to previous experience. The doping concentration is an important parameter for the model. Based on the fiber fabrication experience at the ORC, the Yb ions in the Yb/Al fiber typically have doping concentrations between a few hundred and several thousand ppm (by weight),

and the Yb ions in the Yb/P/Al can have higher doping concentrations rising up to several tens of thousand ppm (by weight). In my simulations, the doping concentration is adjusted by fitting the simulation results to the experimentally measured gain versus pump power and gain versus input signal power, as shown in Figure 3.8. The fitted doping concentration value is found by minimizing the sum of the absolute simulation errors to all the experimental data points in Figure 3.8.

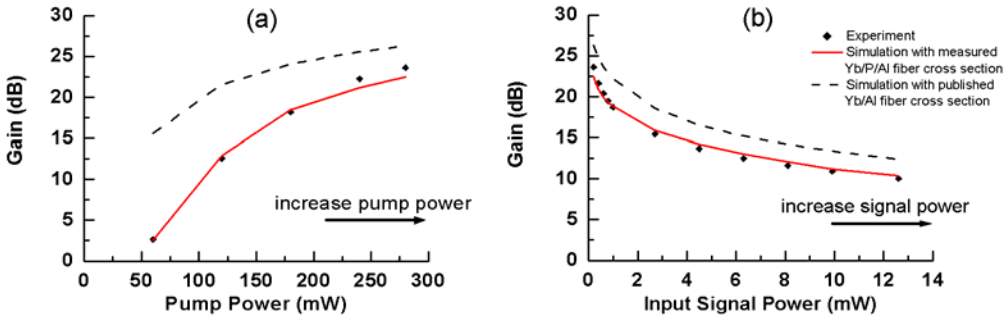

Figure 3.8: Experimental and simulation results for a single stage core-pumped amplifier using 4 m length of fiber and a 1060 nm narrow-line signal. The simulation results include the use of measured Yb/P/Al fiber cross-section and the use of published Yb/Al fiber cross-section for comparison.

Table 3.1. Core-pumped Yb-fiber amplifier parameters used in the simulation

Parameters	Value
Pump wavelength	976.3 nm
Signal wavelength	1060.0 nm
Fiber length	4.0 m
Core diameter	3.7 μm
Core Numerical Aperture (NA)	0.2
Lifetime	1.40 ms
Signal/ Pump overlap factor	0.85
Doping concentration	20000 ppm
Background loss	0.02 dB/m

Figure 3.8 (a) shows the gain with increasing pump power when using a fixed input signal power of 0.2 mW. Figure 3.8 (b) shows the gain with increasing input signal powers when using a fixed pump power of 280 mW. The data shown above clearly demonstrates the accuracy of the simulations. Note that small changes to the majority of the modeling parameters do not drastically change the simulation results and do not alter

predictions of trends in amplifier performance. However, in order to obtain close agreement between simulations and experimental results it is essential to use the appropriate cross-section data for the host glass composition, as is illustrated by the large errors in the comparison data produced with cross-section data for an Yb/Al silicate glass fiber. We conclude that the simulations are able to accurately predict the performance of the experimental amplifier in this simple case.

Compared with the simulations for the narrow-bandwidth input signal that are described above, the use of a broad-bandwidth signal from the mode-locked laser oscillator in the CPA system adds to the complexity of the simulations. This is because the simulation of the broad bandwidth signal requires a wide range of cross-sectional data to be included in the calculations (>40 nm in our simulations). This situation presents a more critical test of the accuracy of the cross-section profile data. As an example to show the predictive ability of the model, Figure 3.9 illustrates the simulated gain and spectral bandwidth (unfilled red squares and dots) with different lengths of Yb/P/Al fiber in the core-pumped amplifier. The input signal has a power of ~0.2 mW with ~20 nm FWHM bandwidth centered at 1055 nm, and the pump has a power of ~200 mW power at 976 nm. Both the input signal and the pump power were measured experimentally before the WDM coupler in the amplifier.

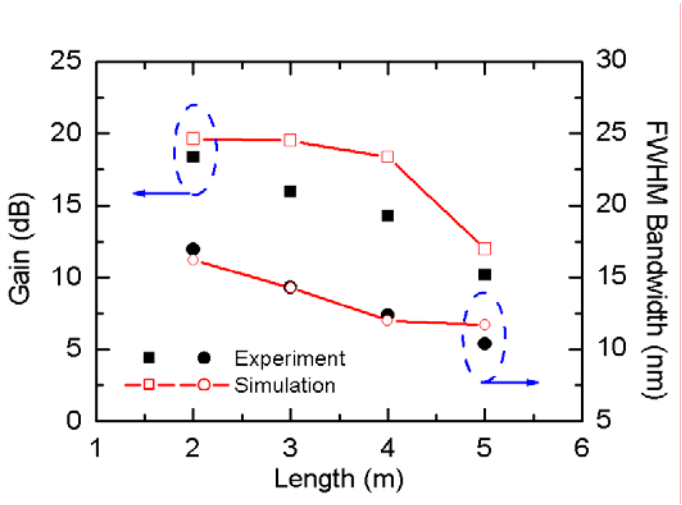

Figure 3.9: Experimental and simulation results for a single stage core-pumped amplifier with different lengths of the Yb/P/Al silicate fiber

All the corresponding experimental results are illustrated in the Figure (filled black squares and dots) for comparison. The experimental results have verified the simulations' prediction that the decrease of the fiber length from 5 m to 2 m can help increase the gain and bandwidth. Note that I applied an estimated 0.1 dB splice loss and an estimated

0.2 dB WDM coupler loss in the simulation for the signal and the pump respectively. However, such losses could be significantly higher in practice. Therefore, it is not surprising to see that the simulated gain can be 2-3 dB higher than the experimental results in Figure 3.9.

3.4.3 Cladding pumped amplifier results

This section reports how the accuracy of my simulations is verified for a more complex system with a broad-bandwidth signal and a high power broad-bandwidth pump. The possibility of high power (>1 W) amplification is one of the most attractive features of Yb-fiber amplifiers, and is enabled by double-clad fiber technology [16]. Compact, low brightness high power diodes are launched into a multimode (undoped) inner cladding and the power is then absorbed by the core [8]. Taken together, broad-bandwidth pump and signal sources, and the greatly reduced pump overlap factor in the cladding-pumping schematic require a dramatic extension of the parameter space used in the model when compared to the simple core-pumped amplifier.

In single-mode double-clad amplifier fibers, the pump overlap factor (Γ_p) can be taken as the Yb-doped core area divided by the area of the inner cladding, provided that the inner-cladding structure introduces strong inter-modal-mixing such that the pump intensity profile is kept uniform as the power is absorbed by the core. Typically $\Gamma_p \sim 0.01$ in a cladding-pumped fiber, compared to $\Gamma_p \sim 0.85$ for a core-pumped fiber. High power diode-pump sources combine several emitters so that the composite output is broad bandwidth compared to the single-emitter grating stabilized diodes used for core-pumping.

The experimental setup is shown in Figure 3.10. The short pulse laser source has ~20 nm bandwidth, centered at 1055 nm, and a repetition rate of ~50 MHz. The source can be modeled using the steady-state Giles model as a result of the Yb-fiber amplifier's long spontaneous lifetime of ~1 ms. The amplifier is a 6.5 m length of Yb-doped double-clad fiber, forward pumped with 6.2 W at 972 nm and backward pumped with 14 W at 918 nm. The pump diodes are temperature stabilized to avoid changes in pump wavelength. However, the modeling approach can easily be used to assess the effects of changes to the pump wavelength.

The parameters used in the simulations are shown in Table 3.2. The experimentally measured pump and signal powers and spectra are used in the model. The fiber length, core and cladding size, core NA, and the spectroscopic data (Figure 3.1 (b)), are also

measured values. The signal and pump overlap factors are calculated values. The background loss is estimated according to previous experiences. The doping concentration is adjusted by fitting the simulation results to the experimentally measured gain versus pump power and gain versus input signal power, as shown in Figure 3.11.

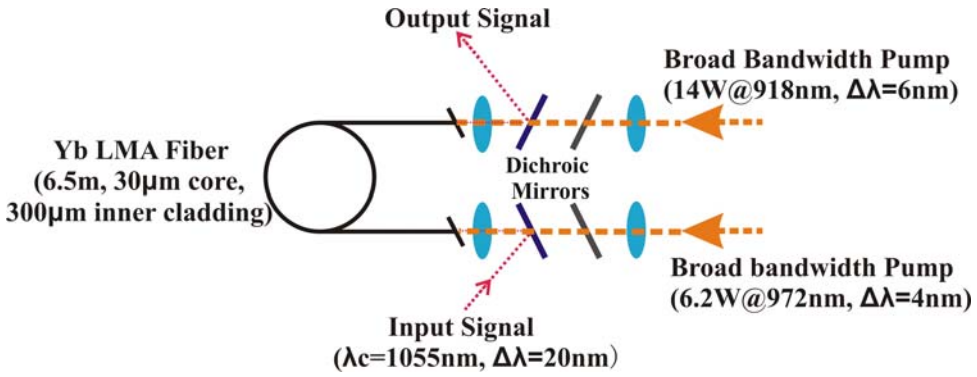

Figure 3.10: Schematic of power amplifier

Table 3.2. Cladding-pumped Yb-fiber amplifier parameters used in the simulations

Parameters	Value
Forward pump wavelength	972 nm
Forward pump bandwidth	4 nm
Backward pump wavelength	918 nm
Backward pump bandwidth	6 nm
Signal centre wavelength	1055 nm
Signal bandwidth	20 nm
Fiber length	6.5 m
Core / Inner-cladding diameter	30 μm / 300 μm
Core Numerical Aperture (NA)	0.06
Lifetime	1.40 ms
Pump overlap factor	0.01
Signal overlap factor	0.85
Doping concentration	7500 ppm
Background loss	0.02 dB/m

Figure 3.11 (a) shows the experimental output spectrum and the simulation results. Figure 3.11 (b) shows the gain with increasing backward pump power and constant 6.2 W forward power with the input signal power fixed at 55 mW. Figure 3.11 (c) shows the gain with increasing input signal power when using a constant 6.2 W forward pump

power plus 6 W of backward pump power. Good agreement has been achieved between modeling results and experiments for this more complex single-amplifier. We again conclude that the simulation results demonstrated highly-accurate predictions of the performance for this more complex cladding-pumped amplifier.

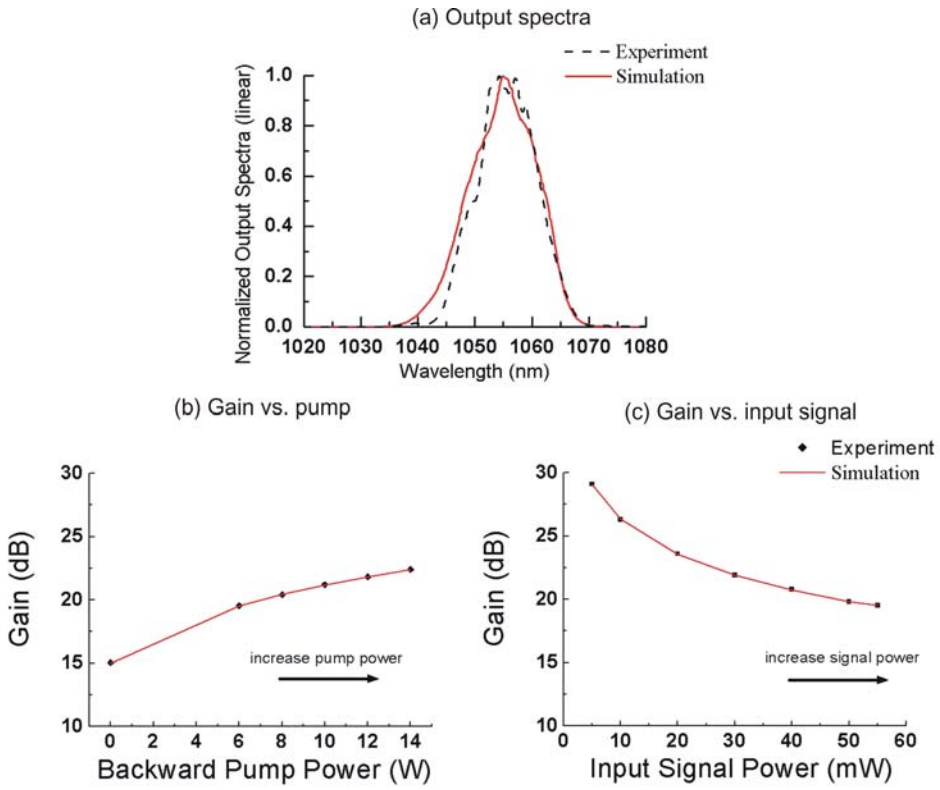

Figure 3.11: Experimental and simulation results for a single stage cladding-pumped amplifier using 6.5 m length of fiber and broad-band signal

Figure 3.12 shows an example of the usefulness for the model in the design of the LMA fibers. LMA fibers with different core:cladding diameters have been used in the model to simulate the amplifier performance. The input signal power of ~0.3 W with ~16 nm FWHM bandwidth centered at 1055 nm and a pump power of ~50 W power at 975 nm (narrow-bandwidth) are used in the simulations. For LMA fiber with core:cladding diameters of 60 μm:600 μm, 60 μm:420 μm, 60 μm:300 μm, and 60 μm:250 μm, the simulated gain and spectral bandwidth vs. the length of the Yb-doped fiber are shown in Figure 3.12.

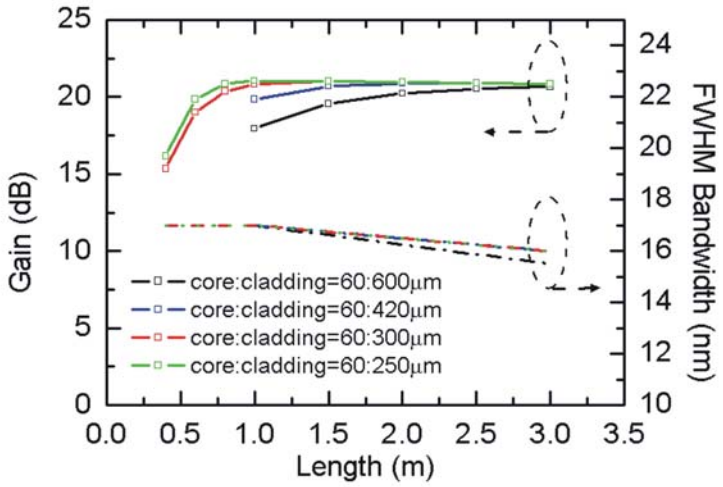

Figure 3.12: Simulation results for a single stage cladding-pumped amplifier with different core to cladding diameters.

The simulation results in Figure 3.12 show that it is possible to use only ~1 m of the Yb-doped fiber in the cladding-pumped amplifier by increasing the fiber core:cladding ratio to 60:300 or higher. With increased mode area and a shorter device length, our new LMA fiber design provides increased fiber nonlinear thresholds, thus it is useful for amplification of high intensity pulses. However, due to the ORC fire that occurred during this thesis research, the fabrication of such LMA fiber was postponed.

3.5 Multi-stage high power amplifier cascade, with broad-bandwidth signal

3.5.1 High average power amplifier cascade and optimization of the gain bandwidth

High power Yb-fiber CPA systems often combine mode-locked seed lasers and amplifier cascades which use both core- and cladding-pumped technology. This section presents the development of a four stage amplifier cascade model for application in CPA systems operating at high repetition rates. This model has been used to help design and construct the amplifier cascade of the high average power CPA system, presented in Chapter 5.

In order to obtain a compact and robust amplifier cascade for the CPA system, core-pumped fiber amplifiers (as illustrated in Figure 2.2 (a)) would be the preferred approach. However, the output power from core-pumped amplifiers, which is limited by the available power from reliable high brightness pigtailed pump diodes, is below the

requirement of our CPA system. Cladding pumped amplifiers (as illustrated in Figure 2.2 (b)) are therefore necessary for the final amplifier stage and possibly required for the penultimate amplifier.

The minimum duration of a pulse is inversely proportional to the bandwidth, so for sub-picosecond pulses a broad bandwidth is required. Although Yb-doped fiber is generally considered to be a good solution for broadband amplification, when using our Yb-doped fiber laser source (which will be presented in detail in Chapter 4) with ~20 nm broad bandwidth pulses, gain narrowing in each successive amplifier can become a limitation in a cascaded system.

When the inversion is high, as in core-pumped amplifiers pumped at the 975 nm absorption peak, the three-level nature of the Yb-ion pushes the gain spectrum to shorter wavelengths around 1030 nm. In contrast, a low inversion fraction is typical in cladding-pumped LMA fiber amplifiers because the low overlap fraction of the pump and core modes leads to slower pump transfer to the Yb ions and, as a consequence, the gain spectrum can be pushed to >1060 nm. A 1055 nm signal wavelength is therefore chosen in order to efficiently combine these technologies. I maximize the gain bandwidth to obtain the shortest pulses and compared my modeling predictions with experimental data.

In addition to the 975 nm pumping wavelength (Yb-doped fiber's main absorption peak, as shown in Figure 3.1), 915 nm pumping (Yb-doped fiber's secondary absorption peak) is also widely used for Yb-doped fiber amplifiers. The merit of using a 915 nm pump comes from the broad absorption peak around 915 nm, so that the pump diodes do not require wavelength stabilization. However, a longer device length has to be used when pumping at a wavelength with lower absorption. Also, the increase of device length will result in an increase of the nonlinear effects introduced to the amplified pulses which must be avoided. Therefore, this thesis research focuses on the use of 975 nm pumps, which provide high pump absorption and allow the use of a short device length, but the diodes have to be wavelength stabilized to avoid power drifts when the diode wavelength is rolling off the peak.

The amplifier cascade is shown in Figure 3.13. The system incorporates optical coupling components between the amplifiers, such as isolators to prevent backward ASE, and these components are all included in the model. The mode-locked fiber laser seed source provides < 150 fs pulses with ~50 MHz repetition rate, and has a ~20 nm bandwidth centered at 1055 nm [17]. Approximately 1 km of Corning HI1060 single-mode fiber is used to stretch the pulses to ~0.8 ns duration, and the pulses are then

amplified in two core-pumped pre-amplifiers and two cladding-pumped power amplifiers. The experimental parameters used in the modeling are shown in Tables 3.1-3.2.

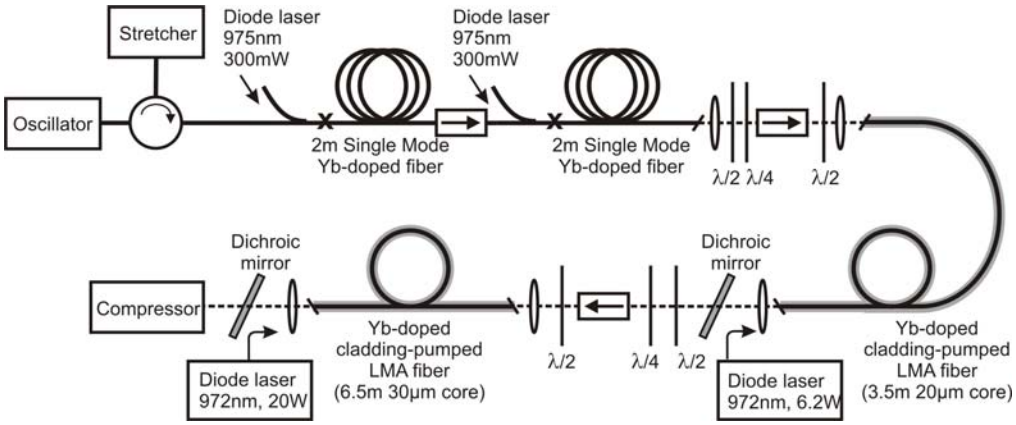

Figure 3.13: Amplifier system schematic for the high average power fiber CPA system

The design optimization starts from the first pre-amplifier. The experimentally measured input signal power, signal spectrum, and pump spectrum are used in the model as fixed parameters. The Yb-fibers used in the amplifiers are chosen based on the availability and the consideration of nonlinear effects. The pump powers and amplifier lengths are treated as variables in the model. The model simulates the amplifier output powers and spectra by varying the pump power from 0-400 mW in 50 mW intervals and the amplifier length from 0-4 m in 0.25 m intervals. The amplifier output powers and spectra are also simulated with different pumping configurations including forward pumping, backward pumping, and mid pumping [18]. The optimization criteria are to find the values of the above two variables to provide the broadest amplifier gain bandwidth and a relatively high signal gain at the same time. According to the simulation results, the design of the first pre-amplifier uses 2 m Yb-fiber with 200 mW pump power in the same propagation direction as the signal. The design was a mid-pumping scheme whereby the WDM coupler is placed after 0.5 m of Yb-fiber such that 1.5 m of Yb-fiber is pumped directly and the initial 0.5 m of Yb-fiber is pumped by backward propagating ASE. This design provides signal output bandwidths of >16 nm with > 23 dB gain. Due to the gain saturation, further increase of the pump power to 400 mW will not effectively increase the signal gain, but will mostly contribute to the ASE noise. In addition, further increase of the fiber length to 4 m reduces the gain bandwidth. After the simulation, the amplifier was constructed and the predicted output spectrum was confirmed

experimentally. Note that for simplicity the detailed schematic of the first pre-amplifier is not shown in Figure 3.13.

The second pre-amplifier is then included and optimized using the same procedure as the first pre-amplifier. According to the simulation results, the design of the second pre-amplifier uses 2 m Yb-fiber, forward pumped by 300 mW pump power. This design provides signal output bandwidth of >14 nm with > 13 dB gain. Note that simulation also predicts that further increase of the pump power to 400 mW will benefit the signal gain, however a 400 mW pump diode was not available when the experiment was performed. The amplifier was constructed and the predicted output spectrum confirmed experimentally before the next step.

The two power amplifiers were then included and optimized in cascaded simulations. In the simulation of cladding-pumped power amplifiers, the amplifier output powers and spectra were simulated with different variable tolerances (the pump power varied from 0-30 W in 0.5 W intervals and the amplifier length from 0-10 m in 0.25 m intervals). The amplifier output powers and spectra were also simulated with different pumping configurations including forward pumping, backward pumping, and bi-directional pumping. The design optimization applies the same optimization criteria as for the pre-amplifiers. According to the simulation results, the design of the first power amplifier uses 3.5 m 20 μm core diameter Yb-fiber, backward pumped by 6.2 W pump power. This design provides a signal output bandwidth of >14 nm. The design of the final power amplifier uses 6.5 m 30 μm core diameter Yb-fiber, backward pumped by 20 W pump power. This design provides a signal output bandwidth of >12 nm. Finally, simulations were performed for the whole system and, by modeling the effects of small changes to the individual amplifier lengths, it is confirmed that achieving good system-wide performance did not require significant re-optimization of the amplifier stages.

Figure 3.14 shows the experimental and simulation results for the bandwidth-optimized cascade at an output power of 10 W (~33 dB net gain, corresponding to ~69 dB total gain considering all the losses associated with the system). The modeled gain profile g(λ) in Figure 3.14 (a), shows that the high gain pre-amplifier designs provided a profile peaked at 1030 nm after the two core-pumped amplifiers (gain1=26 dB, gain2=14 dB). However after the two power amplifiers (gain3=17 dB, gain4=12 dB), the overall system gain is more closely matched to suit the pulse spectrum centered at 1055 nm. Figure 3.14 (b) shows that a good agreement was achieved between the modeled and experimental pulse spectra after the two core-pumped amplifiers. Figures 3.14 (c) and 3.14 (d) show good agreement between the modeled and experimental pulse spectra after the whole system, using both dB and linear scales.

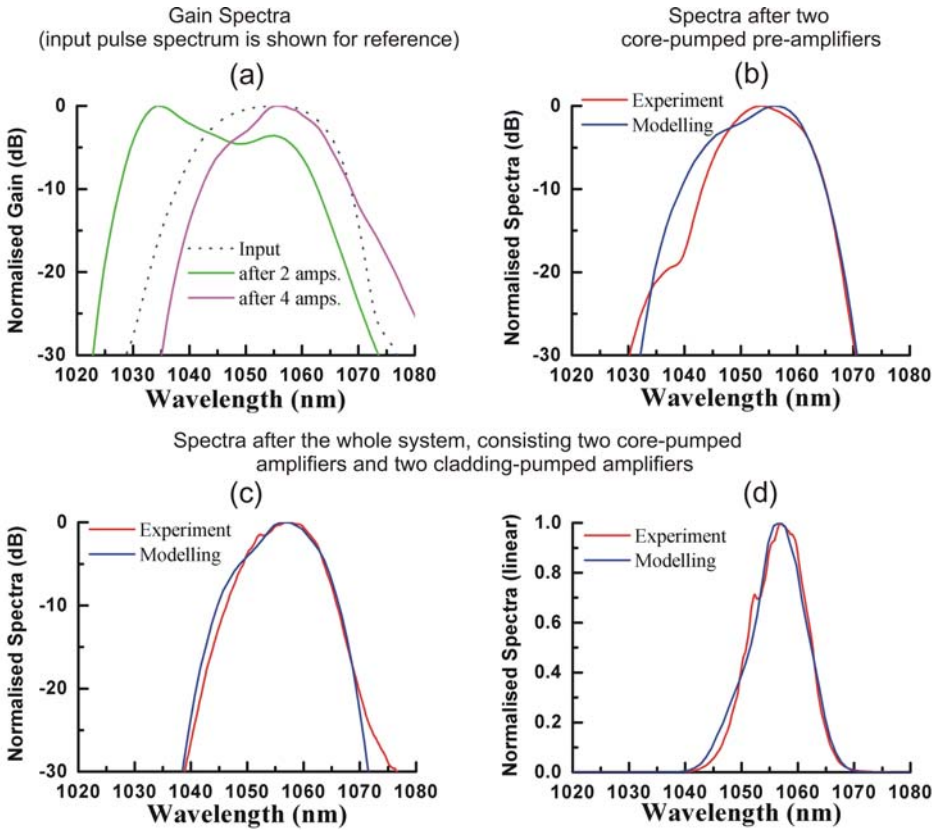

Figure 3.14: Results for a broad bandwidth amplifier cascade. a) Gain spectrum from simulation. (The input pulse spectrum is shown for reference.) b)-d) Simulation results and experimental data for output pulse spectra. b) After core-pumped amplifiers on a dB scale. c)-d) After the whole system on dB and linear scales respectively.

As a measure of the usefulness of the model, it is noted that prior to optimization of the amplifier cascade, the output pulses had a bandwidth of 8 nm, and after optimization, the output bandwidth was increased to 12 nm, i.e. an increase of ~50 % in bandwidth, corresponding to a 33 % reduction in the minimum achievable pulse duration. The amplifier cascade model and the gain bandwidth optimization process presented in this section have been applied to the development of the high average power CPA system in Chapter 5.

Note that the simulated ASE level of the amplifier cascade is generally 20-30 dB lower than the experimental observations. The simulation accuracy of ASE can be improved by incorporating the experimentally measured noise, especially the noise introduced by the seed source, into the model. However, compared with communication systems, the accuracy of the ASE simulation is less important for high power CPA systems. Therefore, this issue is not fully investigated due to the practical difficulties of the noise measurements and its low priority in the project.

3.5.2 High pulse energy amplifier cascade and optimization of the gain bandwidth

Here I demonstrate a high pulse energy amplifier cascade incorporating a PCF in the final amplifier in order to reduce the nonlinear interactions. As presented in Chapter 2, nonlinear effects can become important in the final amplifier where the pulse energies are highest [19, 20]. The nonlinear limit can be increased by either decreasing the effective fiber length or increasing the fiber mode area. Simply cutting back the amplifier fiber length would lead to reduced pump absorption, and reduced gain. Therefore in high energy systems, it is necessary to design new fibers with large cores and smaller inner-cladding diameters so as to increase the pump-overlap fraction. Either conventional LMA fibers or PCF technology can be used for this purpose [21].

The PCF used in the final amplifier has an increased core diameter of 40 μm, and NA of ~0.03, which also provides near diffraction-limited output beam quality. The fiber has an inner cladding diameter of 170 μm, and NA of ~0.62, which is suitable for pump-coupling from our 200 μm, NA of 0.22, fiberised pump diode. The pump absorption at 976 nm is ~13 dB/m. Compared with the 30 μm diameter core fiber used in section 3.5.1, the core mode area of the new fiber is increased by a factor of ~2 and the pump overlap factor is increased by a factor of ~5. Hence a ~1 m length of the PCF would absorb most of the pump, and such a fiber would increase the nonlinear threshold by nearly an order of magnitude compared to the 20 μm core diameter LMA fiber shown earlier.

The cross-section data and the doping concentration are not provided by the PCF manufacturer. In order to acquire the doping concentration parameter, I construct a model to simulate the pump absorption at 975 nm, and then fit the doping concentration parameter by matching the simulated pump absorption to the specification provided by the manufacturer's datasheet. As the PCF is based on Yb/Al silicate host, the PCF amplifier model uses the same cross-section data as used in the LMA fiber amplifier model. Modeling is performed to choose the length of the PCF in the final amplifier following the procedure described in section 3.5.1. Simulations show that short fiber length (1-2 m) can provide good gain (>16 dB), but not the best gain bandwidth of the amplified pulses. However, based on the consideration of nonlinear effects, a 1.2 m long, 40 μm core diameter PCF is used in the design.

A total of 70 dB net gain is required in the high pulse energy amplifier cascade in order to amplify the pulses from the seed source from 100 pJ to ~1 mJ pulse energy. Considering the losses of the stretcher, the compressor, and all other passive components in the system, it is estimated that at least 100 dB total gain is required from all the amplifiers. Based on the consideration of maintaining a high nonlinear threshold and low

ASE noise, it is predicted that it is necessary to develop an amplifier cascade that consisted of three pre-amplifiers and two power amplifiers.

Figure 3.15 shows the bandwidth-optimized cascade for a high pulse energy application. A pre-amplifier, which consisted of a ~1 m Yb-doped single mode fiber, pumped by a 100 mW laser diode at 975 nm, is used to compensate for the loss of average signal power due to the pulse selection when operating the CPA system at low repetition rates such as 50 kHz. The first pre-amplifier is followed by another two pre-amplifiers and one power amplifier, which are similar to the first three amplifiers in the four stage amplifier cascade developed previously for the high average power CPA system (Figure 3.13). The final amplifier consists of a 1.2 m PCF with 40 μm core diameter, and is backward pumped by a 20 W laser diode at 972 nm. EOM and AOMs are used as pulse selectors in this setup, and those components will be discussed in detail in Chapter 4.

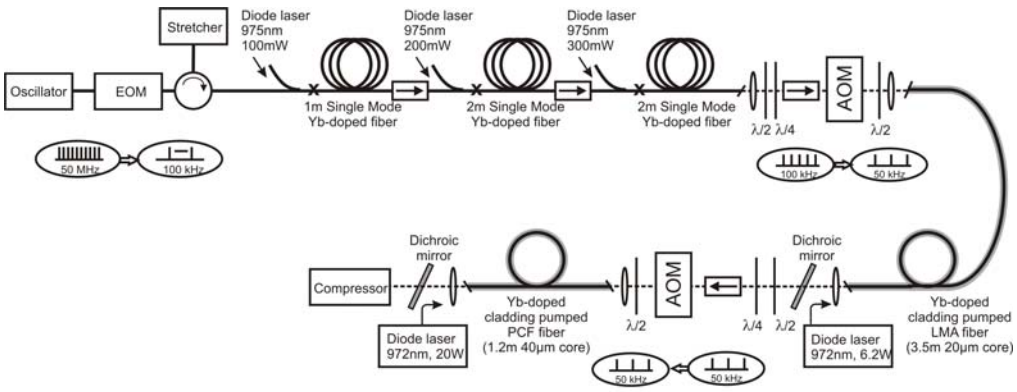

Figure 3.15: Schematic of amplifier cascade for a high pulse energy CPA system

In order to avoid damage to the output facet of the fiber, the output power is limited to 2 W at a pulse repetition rate of ~50 kHz (corresponding to a pulse energy of 0.04 mJ) in the modeling verification and gain bandwidth optimization experiments presented in this section. A CFBG stretcher is used to avoid nonlinear effects in the final amplifier, and provides a ~15 nm spectral window to the input spectrum of the amplifier cascade.

The system spectra are shown in Figure 3.16 (a) and (b). The graphs show the good agreement between the modeled and experimental pulse spectrum at the input and output of the final PCF amplifier. The spectrum at the input of the final amplifier, in Figure 3.16 (a), is still well matched to the spectrum from the CFBG output thus demonstrating the successful minimizing of gain narrowing in this setup. Figure 3.16 (b) shows that the

pulse spectrum has been pushed slightly towards a shorter wavelength in the PCF amplifier even after the gain bandwidth optimization. The modeling results show that the gain efficiency and gain bandwidth have to be slightly compromised when incorporating PCF in our amplifier cascade in order to increase the nonlinear limit.

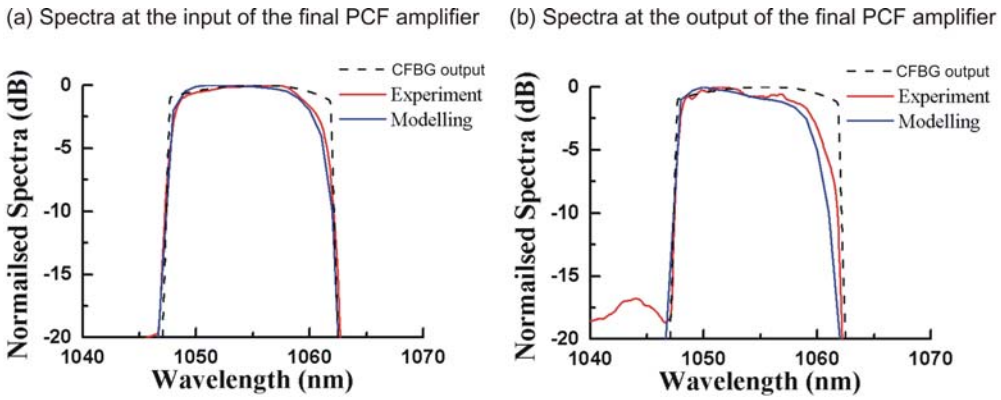

Figure 3.16: Simulation results and experimental data for the output pulse spectra after the amplifier cascade with 40 µm core diameter PCF fiber. (Spectrum from the CFBG output was also shown for comparison)

To show the predictive ability of the model, Figure 3.17 presents a simulation example for an amplifier cascade operating at a different central wavelength. The simulations are based on the use of a seed source with increased pulse energy of 0.5 nJ and a different central wavelength of 1045 nm, compared with the one used in previous simulations. The design criteria are to amplify the seed pulses to 1 mJ (63 dB net gain) by using a cascade of two core-pumped amplifiers and two cladding-pumped amplifiers. LMA fiber with 60 µm core diameter and 250 µm cladding diameter is used in the final amplifier for the amplification of high intensity pulses. With the assumption that the total losses of the system are -18 dB, the total gain required for the amplifier cascade is 81 dB. The same gain bandwidth optimization procedures, as described in section 3.5.1, have been applied for this simulation. The schematic of the bandwidth-optimized amplifier cascade is showed in Figure 3.17 (a). The simulated gain of each amplifier is 26 dB, 17 dB, 21 dB, and 17 dB, respectively. Figure 3.17 (b) shows the input and output spectra of the amplifier cascade.

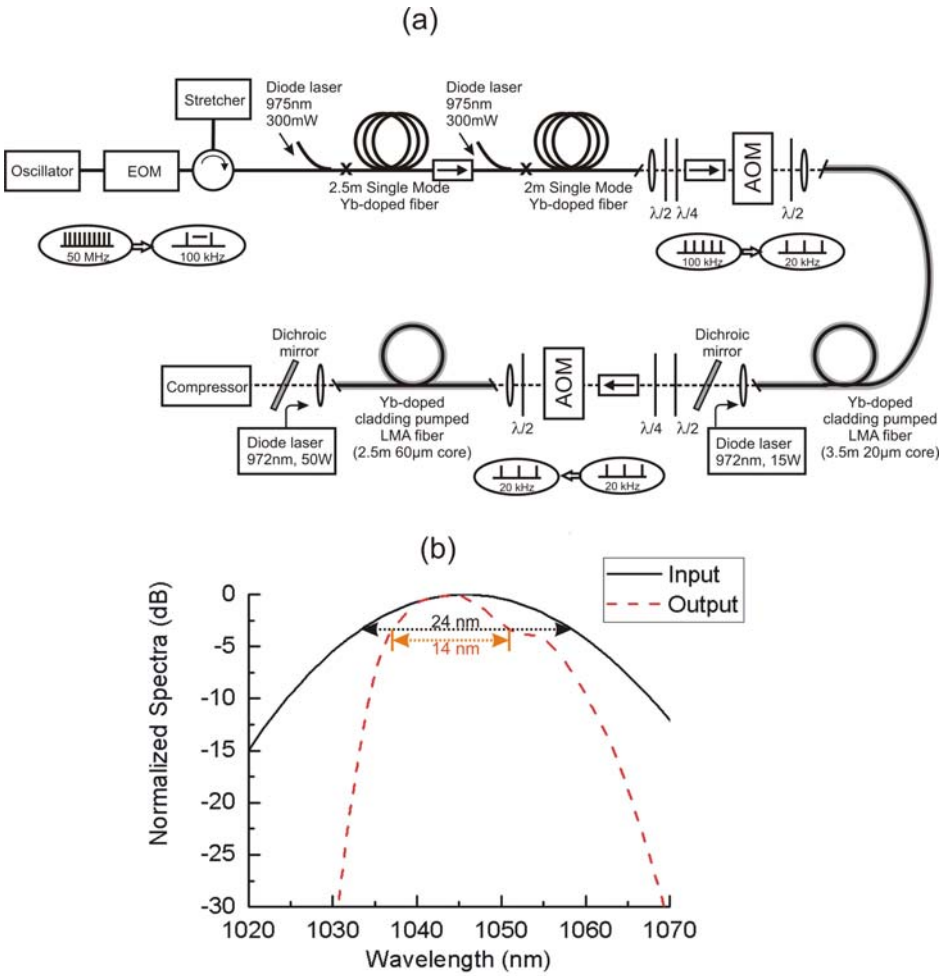

Figure 3.17: Simulation results for a high pulse energy CPA system with central wavelength of 1045 nm

The simulation results in Figure 3.17 provide useful information of a CPA system operating at a shorter central wavelength. Without performing the complex experiments, it can be seen from the simulation predictions that the use of shorter central wavelength may not help to maintain the spectral bandwidth. The simulations predict gain dragging towards the shorter wavelength, which can originate from the rising slope towards 1020 nm wavelength in the emission cross-section data. This simulation example demonstrates how modeling can provide rapid feedback when assessing the performance of a variety of fiber designs against the constraints imposed by specific applications.

3.6 Conclusion

This chapter presented the development and verification of modeling tools for various types of Yb-doped fiber amplifiers. An existing EDFA model, developed originally for

modeling telecommunication devices and systems, had been modified as the platform for this research. The spectroscopic data of the Yb-doped fiber was measured, and was input to the models. The simulation and experimental characterization of single stage amplifiers was first performed to provide a solid level of confidence for the predictions of the models. Then the gain bandwidth of a four stage cascaded amplifier system was modeled and optimized, which enabled a 50 % increase in gain bandwidth to be obtained. This thesis research also investigated the optimization of another amplifier cascades with the use of PCF amplifiers. In all cases the simulation results were found to be in good agreement with experimental results.

In pulsed applications of Yb-doped fiber amplifiers, the high peak powers posed unique challenges, not fully addressed by existing models, and future work could be usefully directed towards the release of additional modeling tools to address these specific challenges. For example, whilst the use of single mode fibers enables the effective overlap integral approach to be used in order to reduce the computations required, for high power Yb amplifiers it may be helpful to develop new models for multi-mode fibers. Other challenges include the incorporation of nonlinear and dispersive effects within fully spectrally-resolved and dynamic-gain models.

References:

[1] D. Strickland and G. Mourou, "Compression Of Amplified Chirped Optical Pulses," *Optics Communications*, vol. 56, pp. 219-221, 1985.

[2] B. Shiner, "The all-around performer," *Nature Photonics*, vol. 2, pp. 24-25, 2008.

[3] P. Dupriez, A. Piper, A. Malinowski, J. K. Sahu, M. Ibsen, Y. Jeong, L. M. B. Hickey, M. N. Zervas, J. Nilsson, and D. J. Richardson, "321 W average power, 1 GHz, 20 ps, 1060 nm pulsed fiber MOPA source," in *Optical Fiber Communications Conference*. Anaheim: Optical Society of America, 2005, PDP3.

[4] E. Desurvire, *Erbium-doped fiber amplifiers: principles and applications*: New York: Wiley, 1994.

[5] F. He, J.H.V.Price, K.T.Vu, A.Malinowski, J.K.Sahu, and D.J.Richardson, "Optimisation of cascaded Yb fiber amplifier chains using numerical-modelling," *Optics Express*, vol. 14, pp. 12846-12858, 2006.

[6] C. R. Giles and E. Desurvire, "Propagation of Signal and Noise in Concatenated Erbium-Doped Fiber Optical Amplifiers," *Journal of Lightwave Technology*, vol. 9, pp. 147-154, 1991.

[7] C. R. Giles and E. Desurvire, "Modeling Erbium-Doped Fiber Amplifiers," *Journal of Lightwave Technology*, vol. 9, pp. 271-283, 1991.

[8] R. Paschotta, J. Nilsson, A. C. Tropper, and D. C. Hanna, "Ytterbium-doped fiber amplifiers," *IEEE Journal of Quantum Electronics*, vol. 33, pp. 1049-1056, 1997.

[9] H. M. Pask, R. J. Carman, D. C. Hanna, A. C. Tropper, C. J. Mackechnie, P. R. Barber, and J. M. Dawes, "Ytterbium-Doped Silica Fiber Lasers - Versatile Sources for the 1-1.2 um Region," *IEEE Journal of Selected Topics in Quantum Electronics*, vol. 1, pp. 2-13, 1995.

[10] M. J. F. Digonnet, *Rare-Earth-Doped Fiber Lasers and Amplifiers*, 2nd ed, 2001.

[11] W. L. Barnes, R. I. Laming, E. J. Tarbox, and P. R. Morkel, "Absorption and emission cross-section of Er^{3+} doped silica fibers," *IEEE Journal of Quantum Electronics*, vol. 27, pp. 1004-1010, 1991.

[12] W. J. Miniscalco and R. S. Quimby, "General procedure for the analysis of Er^{3+} cross-sections," *Optics Letters*, vol. 16, pp. 258-260, 1991.

[13] P. R. Morkel and R. I. Laming, "Theoretical modeling of Erbium-doped fiber amplifiers with excited-state absorption," *Optics Letters*, vol. 14, pp. 1062-1064, 1989.

[14] D. E. McCumber, "Theory of Phonon-Terminated Optical Masers," *Physical Review*, vol. 134, 1964.

[15] M. J. F. Digonnet, E. Murphy-Chutorian, and D. G. Falquier, "Fundamental limitations of the McCumber relation applied to Er- doped silica and other amorphous-host lasers," *IEEE Journal of Quantum Electronics*, vol. 38, pp. 1629-1637, 2002.

[16] E. Snitzer, H. Po, F. Hakimi, R. Tumminelli, and B. C. McCollum, "Double Clad, Offset Core Nd Fiber Laser," *Proceedings, OFS conference, New Orleans*, pp. Post-deadline paper PD5, 1988.

[17] L. Lefort, J. H. V. Price, D. J. Richardson, G. J. Spuhler, R. Paschotta, U. Keller, A. R. Fry, and J. Weston, "Practical low-noise stretched-pulse Yb^{3+}-doped fiber laser," *Optics Letters*, vol. 27, pp. 291-293, 2002.

[18] R. I. Laming, M. N. Zervas, and D. N. Payne, "Erbium-doped fiber amplifier with 54 dB gain and 3.1 dB noise figures," *IEEE Photonics Technology Letters*, vol. 4, pp. 1345-1347, 1992.

[19] G. P. Agrawal, *Nonlinear Fiber Optics*, 3rd ed. San Diego: Academic Press, 2001.

[20] A. Galvanauskas, "Mode-scalable fiber-based chirped pulse amplification systems," *IEEE Journal of Selected Topics in Quantum Electronics*, vol. 7, pp. 504-517, 2001.

[21] J. Limpert, A. Liem, M. Reich, T. Schreiber, S. Nolte, H. Zellmer, A. Tunnermann, J. Broeng, A. Petersson, and C. Jakobsen, "Low-nonlinearity single-transverse-mode ytterbium-doped photonic crystal fiber amplifier," *Optics Express*, vol. 12, pp. 1313-1319, 2004.

Chapter 4 Overview of femtosecond fiber CPA technology

Chapters 4-7 present the experimental investigation of fiber CPA systems. Chapter 4 starts with a general schematic for the systems developed in this thesis. This is followed by the descriptions of the performance of individual components, taken in the order in which they appear in the system, from the seed pulse source at the input to high power amplifiers at the output. A high average power version of the CPA system is investigated in Chapter 5 and a high pulse energy version of the system in Chapter 6. Chapter 7 gives details of experiments carried out with an active pulse shaping device incorporated in the high pulse energy CPA system.

4.1 CPA system schematics

A general schematic representation of all the specific CPA systems developed in this thesis research is shown in Figure 4.1. A passively mode-locked Yb-doped fiber oscillator, producing ~100 fs pulses, is used as the seed for the system. The seed pulses are stretched by a pulse stretcher. Three types of pulse stretchers have been incorporated in our systems, including a CFBG (Chapter 5), a dielectric grating (Chapters 6-7), and a single-mode passive fiber (Chapter 7). As presented in Chapter 3, a multi-stage amplifier cascade is designed, and then optimized, for maximum output pulse spectral bandwidth, by using modeling tools. A dielectric grating which has a high efficiency, a high power handling capability, and a high compression ratio (to support the high average power and high pulse energy), is used as a pulse compressor in the system. The design and characterization of each individual component in the system will be presented in sections 4.3-4.5.

High pulse energies are achieved and realized at reduced pulse repetition rates by including a high extinction ratio (>40 dB) EOM for pulse selection. ASE build-up is prevented by incorporating isolators and AOM time gating between amplifier stages

(synchronized to the arrival of each pulse). The pulse selection method, and the characterization of the pulse selectors will be discussed in section 4.5.

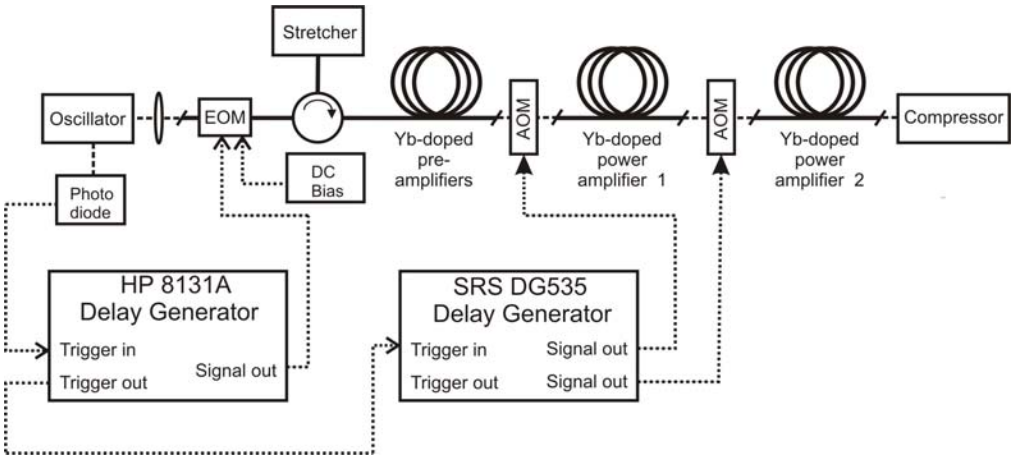

Figure 4.1: A general schematic for the CPA systems in this thesis research

4.2 Oscillator

A compact and stable mode-locked Yb-doped fiber oscillator has been developed as the seed laser for the CPA system before the start of this thesis research [1]. A schematic of the oscillator is shown in Figure 4.2. The oscillator uses a Fabry-Perot cavity design, which contains a grating based dispersive delay line, ~1.0 m of high-concentration, moderately birefringent, Yb-doped fiber with angle polished ends, and a semiconductor saturable absorber mirror (SESAM) to initiate self-start mode locking. The oscillator uses nonlinear polarization rotation switching to sustain mode-locking. Two polarizing beam splitters (PBS) and associated wave plates are included to control the bias of the polarization switch and to adjust the output coupling.

The output is extracted from either PBS1 or PBS2. The rejected part of the pulse appears at Port 1, as PBS1 acts as the polarization switch. The half-wave plate between PBS1 and PBS2 provides adjustable output coupling. Negatively (the instantaneous frequency decreases linearly with time) chirped pulses are output from PBS1 at Port 2. Positively chirped pulses are output from PBS2 at Port 3, which are used as the seed to the CPA system. Pumped by a 976 nm laser diode, with 60 mW power through a 976/1050 nm WDM coupler, the oscillator has robust, reliable self starting, single pulse, mode-locked operation with no Q-switching instabilities. The maximum average power at Port 3 is 3 mW, which corresponds to a 60 pJ pulse energy (the pulse repetition rate is approximately 50 MHz).

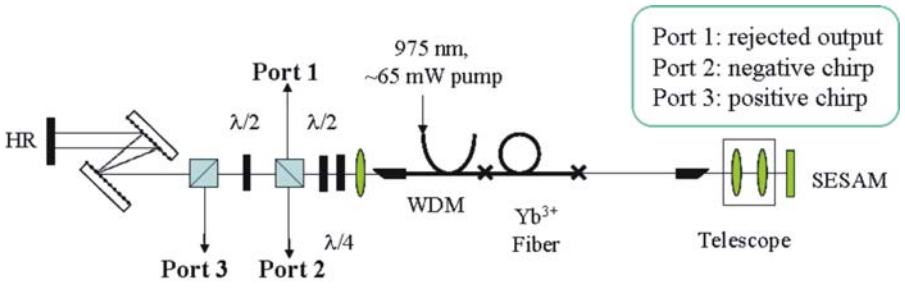

Figure 4.2: Schematic of mode-locked fiber oscillator (from Ref. [1])

The output spectrum from Port 3 is centered at 1056 nm, with a spectral bandwidth of 18.6 nm, as shown in Figure 4.3 (a). The output pulses directly from Port 3 have a strong temporal chirp, and the pulse duration is measured, using second harmonic generation (SHG) autocorrelation, to be ~2.4 ps. The linearly chirped pulses from Port 3 can be compressed by use of a diffraction grating pair. Figure 4.3 (b) shows the autocorrelation of the compressed pulses, after which the pulses have an estimated FWHM of 108 fs (assuming a Gaussian pulse shape). The corresponding time bandwidth product of the compressed pulses is ~0.54. By comparison, the time bandwidth product for a transform-limited Gaussian pulse is 0.44.

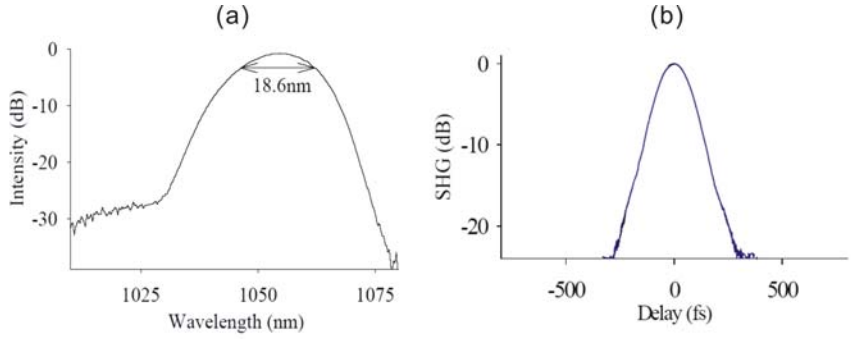

Figure 4.3:(a) Spectrum of pulses from Port 3; (b) Autocorrelation of compressed pulses from Port 3 [1]

A commercial, femtosecond, Nd:glass laser system (Time-Bandwidth Products, GLX-200) is used as the seed source in the CPA system presented in Chapter 7. This CPA system incorporates a pulse shaping device, and the increased seed pulse energy from the GLX-200 enables the shaper's insertion loss to be accommodated without the addition of new amplifier stages. The laser provides ~200 mW average power with a repetition rate of 80 MHz, corresponding to a pulse energy of 2.5 nJ. As shown in Figure 4.4, the output spectrum is centered at 1053.8 nm, with 3.7 nm FWHM spectral bandwidth, and the autocorrelation FWHM duration is ~ 650 fs.

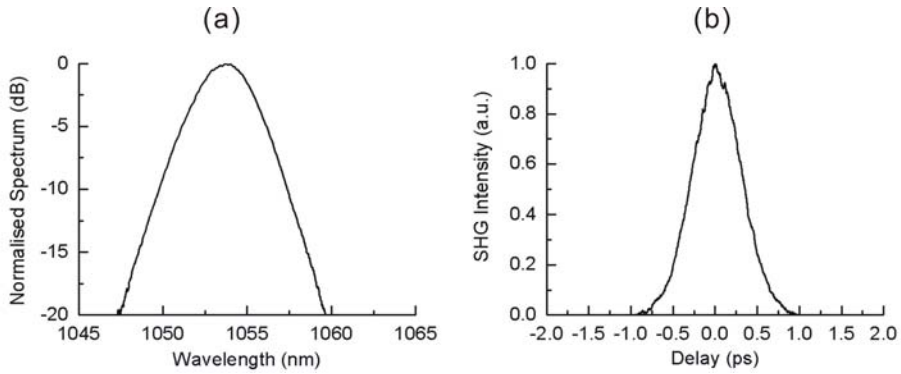

Figure 4.4: (a) output spectrum and (b) autocorrelation of commercial glass laser oscillator.

4.3 Stretcher and compressor

The CPA technique avoids high peak intensities occurring in the amplifiers, and hence avoids the limiting effects of nonlinearity (SPM, SRS, and self-focusing). Therefore, the design criterion for the stretcher/compressor is to provide a stretched pulse with duration as long as possible within the constraints created by the dimensions of the selected pulse stretcher and compressor components.

Diffraction grating stretchers and compressors are widely used in high energy solid-state CPA systems. The broad spectral bandwidth, which is one of the characteristics of ultrashort pulses, makes it relatively easy to stretch and compress such pulses by large factors, of up to 10^4, by using angular dispersion in diffraction grating based pulse stretching and compression arrangements [2]. As discussed in Chapter 2, dielectric gratings have the advantage of high power handling, compared to gold gratings, but without the size constraints associated with fused silica transmission gratings. Therefore, a dielectric grating stretcher and compressor is used in the higher pulse energy CPA experiments in Chapter 6.

Diffraction grating arrangements are typically large and require precise alignment because the pulse stretching/compression techniques rely on spatial effects. Therefore, diffraction grating components are not compatible with the targeted compactness and robustness required for fiber based CPA systems. This creates the need to use compact alternatives to the conventional bulk grating components; especially for compact stretchers because diffraction grating compressors are usually required due to the high peak power of the recompressed pulses.

A CFBG provides a robust, compact, and alignment-free pulse stretcher, which can provide suitable time delays in only centimeter lengths of fiber. The highly flexible CFBG writing technology, developed at the ORC [3], has enabled us to fabricate a

CFBG with both the 2nd and 3rd order dispersion required to match the bulk-grating compressor. The combination of a CFBG stretcher and a dielectric grating compressor has been used in the high average power CPA system in Chapter 5.

Fiber stretchers were not used in earlier CPA systems because the 3rd order dispersion from the fiber stretcher has the same sign as that from the grating compressor, which leads to recompressed pulses with accumulated 3rd order dispersion. This results in degraded pulse quality, as shown in the simulations for pulses with uncompensated 2nd and 3rd order dispersion in Chapter 2. Therefore, additional components or technological approaches are required. In Chapter 7, I demonstrate a CPA system incorporating a fiber stretcher, a grating compressor and a pulse shaper. The unmatched dispersion from the stretcher/compressor and the nonlinear phase shift in the system are compensated by the pulse shaper.

4.4 Fiber amplifier cascade

The amplifier cascades have been designed by using numerical modeling tools, as presented in Chapter 3. This section provides a summary of the characteristics of the fibers that are used in this thesis research, as shown in Table 4.1.

Table 4.1: Characteristics of the fibers used in this thesis research

	Single-mode fiber	**LMA fiber**	**PCF**	**Polarizing PCF**
Core diameter (μm)	3.7	20	40	40
Core NA	0.2	0.06	0.03	0.03
Inner cladding diameter (μm)	-	180	170	200
Inner cladding NA	-	0.5	0.62	0.55
Outer cladding diameter (μm)	125	400	620	450
Dopants and host glass materials	Yb/P/Al/Si	Yb/Al/Si	Yb/Al/Si	Yb/Al/Si
V	2.20	3.57	3.57	3.57
Pump absorption at 976 nm (dB/m)	1000	3	13	10
Slope efficiency	75%	77%	60%	60%
Effective mode area (μm^2)	10	200	750	650
Typical device length (m)	1-2	3-5	1-2	1-2
Bending diameter (cm)	5	20	30	30
Measured M^2 in amplifier configuration	1.0	1.1	1.2	1.2

The Yb-doped single-mode fiber was fabricated at the ORC prior to this thesis research, and used in the core-pumped pre-amplifiers. The LMA fiber was utilized in the early stage of this thesis research before the work was stopped by the fire at the ORC. The PCF, a commercial product from Crystal Fibres A/S, was used in the later development of the high pulse energy CPA systems.

The normalized frequency V (Equation 2.1) can be employed to estimate the number of modes supported by the fiber [4]. The core-pumped fiber only supports the fundamental mode as V<2.405. The 20 μm core diameter LMA fiber and the PCFs support up to 4 modes, according to the calculations in [4, 5]. As discussed in Chapter 2, quasi-single-mode operation in LMA fibers can be realized by ensuring that the launch condition and the mode quality of the seed beam are carefully matched to the fundamental mode, although this approach is difficult and sensitive to perturbations in practice. As fiber coiling can induce significant bend loss for all but the fundamental mode in multimode fibers [6], it has been used, in combination with the launch condition approach, for mode filtering.

Table 4.1 shows the measured output beam M^2 values of the LMA fiber and PCFs with the corresponding coiling diameters. This good beam quality (M^2<1.2) from the fiber amplifier cascade is required for the pulse compression stage and is essential for most applications including X-ray generation. As an example, Figure 4.5 shows the effect of fiber bending on the output mode quality. The measurement is for 5 m of ORC fabricated LMA fiber in an amplifier setup. The LMA fiber has a core diameter of 25 μm and a NA of 0.06, and a cladding diameter of 210 μm. The results in Figure 4.5 show that the output mode quality can be improved by using appropriate bending of the LMA fibers.

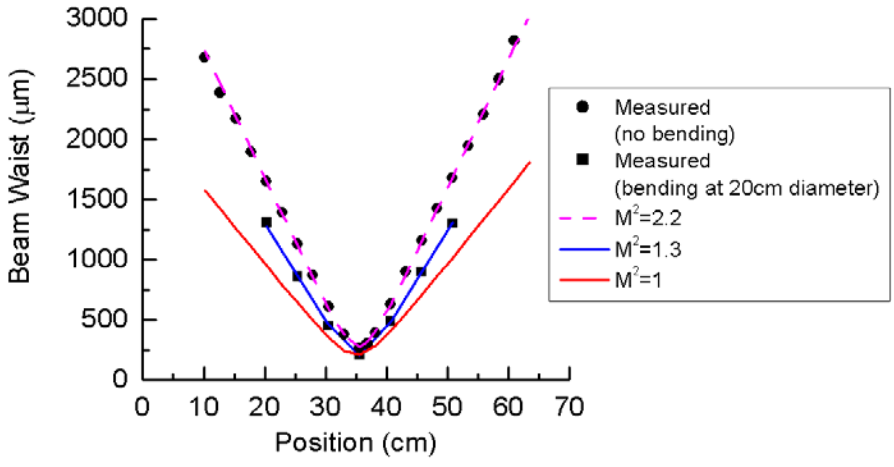

Figure 4.5: The effect of fiber bending on output mode quality of 25 μm core diameter LMA fibers

Table 4.1 summarizes fiber parameters that relate to the nonlinear thresholds, such as the physical core diameter, the effective mode area, and the typical device length parameters. Compared with the 20 μm core diameter LMA fiber, the PCF has a larger effective mode area and a reduced device length, which leads to a reduction in nonlinearity by an order of magnitude. Therefore PCF is used in the high pulse energy CPA systems for the amplification of high intensity pulses.

Both the LMA fiber and the PCF provide high slope efficiency when used in our system. I measured the slope efficiency of 77% for the LMA fiber and 60% for the PCF with respect to launched pump power.

A type of polarizing PCF, which acts as a PM fiber for wavelengths longer than the polarizing cut-off, has also been used in the final stage of the amplifier cascade [7]. When the fiber bend radius is correctly set, the polarizing PCF has a differential loss between the fiber polarization axes over a certain wavelength range. As discussed in Chapter 2, the use of polarizing PCF avoids nonlinear polarization rotation that is related to the high pulse intensities and which usually exists in the final amplifiers. The polarization extinction ratio of the final amplifier, using 2 m polarizing PCF, is measured to be ~10 dB in our systems.

4.5 Pulse selection and time gating between amplifiers

Mode-locked fiber lasers have a typical cavity length of several meters, which leads to pulse repetition rates of ~50 MHz. Therefore, in order to achieve high pulse energies at moderate average powers, the pulse repetition rates are usually reduced by pulse selection before amplification in fiber CPA systems. In practice, an Yb-doped fiber amplifier can be operated with CW pumping at repetition rates as low as 10 kHz, due to Yb-doped fiber's long upper-level lifetime.

A high speed (>3 GHz), high extinction ratio (>40 dB), lithium niobate ($LiNbO_3$) based Mach-Zehnder interferometer EOM is utilized for pulse selection of the seed pulses. In such configuration, the input signal is equally split into two waveguides. An electric field is applied to one of (or sometimes both of) the two waveguides to provide a phase change to the signals, and finally the signals from the two waveguides are re-combined at the output. The modulator transfer function is given by the following expression [8]:

$$\Gamma(V) = \cos^2\left(\frac{\phi_0}{2} - \frac{\pi}{2}\frac{V}{V_\pi}\right) \tag{4.1}$$

where ϕ_0 is dependant on the optical path difference and DC bias. The retardation half-wave voltage V_π is the applied voltage necessary to obtain a phase retardation of π. The intensity modulation of the input pulse train is obtained by the phase modulation in one (or sometimes both) of the arms of the Mach-Zehnder interferometer. The DC bias is adjusted such that ϕ_0 is a multiple of π. In this case $\Gamma(V=0)=1$ and $\Gamma(V=V_\pi)=0$, so that the modulator switches the light 'on' and 'off' as V is switched between 0 and V_π. A pulse delay generator (HP 8131A) is used to provide the signal to the EOM, and a fast photodiode at Port 2 in the oscillator provides the trigger for the pulse delay generator. Note that the device may be operated as a linear intensity modulator by adjusting the $\phi_0 = \pi/2$ and operating in the nearly linear region around $\Gamma = 0.5$.

Two commercial EOMs, from Crisel Instruments, labeled as EOM1 and EOM2, are available for the CPA system. EOM1 is an earlier product which is used for most of the work in this thesis. However, degradation of EOM1 with respect to broadband performance was observed in 2007. Figure 4.6 (a) shows the EOM1 output spectra at different temperatures after the performance degradation. The changes of spectra with temperature can introduce variations of the pulse spectrum at the output of the CPA system and, as a consequence, the durations of the re-compressed pulses. Therefore, EOM1 was replaced by EOM2, which was a new 20 GHz product with broad and stable spectral transmission, as shown in Figure 4.6 (b). The measured extinction ratios of EOM1 and EOM2 are shown in Figure 4.6 (c). The measured insertion losses of EOM1 and EOM2 are -4 dB and -5 dB respectively.

When the CPA system is operated at low repetition rates, ASE build-up along the amplifier cascade can be a significant problem. Isolators are inserted between each amplifier to prevent backward ASE, and polarization controllers are used to ensure maximum throughput from the isolators. AOMs are inserted between each amplifier to suppress the forward ASE. The AOMs are commercial products, from AA Sa. (model number AA ST110_1.06), which are made from TeO_2 (acoustic velocity 4200 m/s) with a specified rise time of 160 ns/mm. The AOMs are aligned such that the first order diffracted beam is launched into the following amplifier stage. A signal generator (Stanford Research Systems DG 535) triggered by the pulse delay generator (HP 8131A), provides modulation signals for the AOMs, to allow the pulses through but to block the ASE background. With a beam diameter ~1.5 mm, the experimentally determined

optimum time window (to just avoid clipping of the transmitted pulse) is found to be 320 ns. The schematic of the system timing control is illustrated in Figure 4.1.

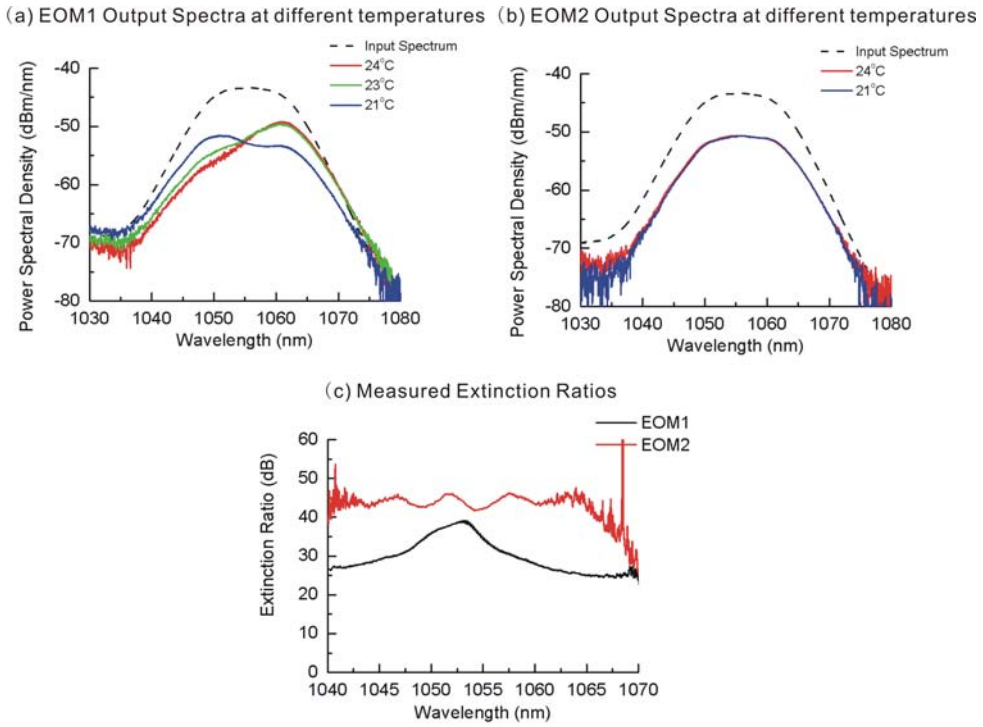

Figure 4.6: Characteristics of EOM1 and EOM2. (a) and (b) show output spectra at different temperatures (input spectrum is shown as reference), (c) shows the extinction ratios.

4.6 Technological challenges and limitations in fibers

There are various technological challenges and limitations involved in the development of fiber laser and amplifier systems. This section starts with a brief summary of the most critical limitations that relate to this thesis research, such as the nonlinear effects and the limited spectral bandwidth. This section then presents technological challenges that require additional engineering considerations, such as thermal and optical damage. Finally, this section summarizes other technological challenges and limitations that have been observed in the development of fiber lasers and amplifiers, but have a minor relation to this thesis research. Such issues include self-focusing, energy-saturation, and photo-darkening.

4.6.1 Nonlinear effects

The two nonlinear effects that have the most important consequences in fiber amplifiers are SPM and SRS. As presented in Chapter 2, SPM affects the phase of the pulses with high peak intensities. In high power CPA systems, the SPM induced nonlinear phase on the amplified stretched pulses will result in pulse shape distortions after recompression, which influences both the pulse duration and quality. In addition to the review presented in Chapter 2, detailed analysis of SPM effects in CPA systems has been covered by a number of research papers [9-11].

SRS constitutes a limitation for the extractable pulse energy from fiber amplifiers. As discussed in Chapter 2, when the peak power of the amplified pulse has reached the Raman threshold, most of the pulse energy starts transferring into the new Stokes components. Therefore the recompressed pulse energy is limited by the onset of SRS.

In all our CPA systems, significant SPM phase (B-integral > 2π) is introduced onto the pulse at a pulse intensity below the SRS threshold. Therefore, since achieving good quality pulses is required for X-ray generation, SPM is the main nonlinear limitation in practice in this thesis work to date.

4.6.2 Spectral limitations

Although Yb-doped fiber has a broad gain bandwidth, thus being good for amplification of broadband signals, gain narrowing in the amplifiers is still a factor that limits the minimum pulse duration of the recompressed pulses. A detailed study on the avoidance of gain narrowing has been presented in Chapter 3.

The CPA system output spectrum is also affected by the bandwidth and the spectral window of each passive component in the system, especially the stretcher and the compressor. The term “spectral window” is usually used to distinguish whether a particular wavelength is, or is not, reflected by the stretcher and compressor. The bulk grating stretcher and compressor used in this thesis research both have ~12 nm spectral windows, which is the wavelength range that is transmitted through the stretcher/compressor optics without clipping the edges of the grating. The spectral window of the CFBG stretcher is ~14 nm, which is determined by the range of the grating period written within the core of the fiber.

4.6.3 Optical damage

Below the critical peak power for self-focusing, optical damage can still be created via multi-photon absorption. This is the standard damage mechanism for nanosecond pulses incident on transparent materials, and the damage threshold for fused silica is dependent on both the pulse duration and wavelength [12]. For one nanosecond pulses at 1055 nm, the bulk damage threshold of silica fiber is estimated to be ~40 J/cm^2 [13].

Due to surface dirt or scratches on the fiber facet, the surface damage threshold of fused silica fiber is significantly lower than the bulk damage threshold inside the fiber, and is a critical limit for high pulse energy amplification. In practice, fiber facet damage can be relieved by the proper treatment of the fiber ends, such as using end-caps. As shown in Figure 4.7, an end-cap is a short piece of coreless fiber that is spliced to the end of the fiber. The length of the end-cap is set to ensure that the fiber input/output beam has a significantly larger area on the glass-to-air interface than on the fiber itself. Therefore, the use of an end-cap ensures a low intensity at the glass-to-air interface, while the high intensity focusing spot is maintained inside the glass.

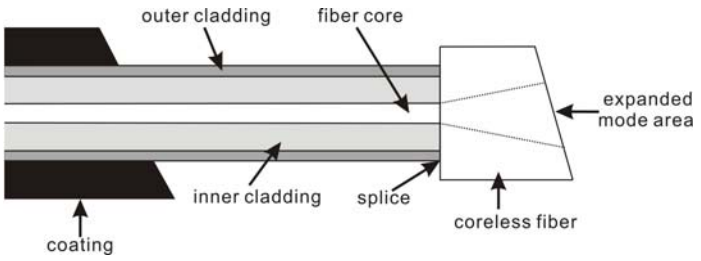

Figure 4.7: Fiber endcap

4.6.4 Thermal damage

Yb-doped fibers have excellent thermal properties due to their high quantum efficiency and geometry. However, if there are localized areas of the cladding that cause pump light leakage, heating can lead to thermal damage, such as damage to the coating and fiber end melting, which can readily occur at average power levels above 100 W. Figure 4.8 shows some examples of thermal damage experienced during this thesis research, including fiber coating burning due to fabrication defects (Figure 4.8 (a)), damage to an imperfect fiber cladding (Figure 4.8 (b)), damage to the fiber coating (Figure 4.8 (c)), and damage due to excessive bending and local leakage of light (Figure 4.8 (d)).

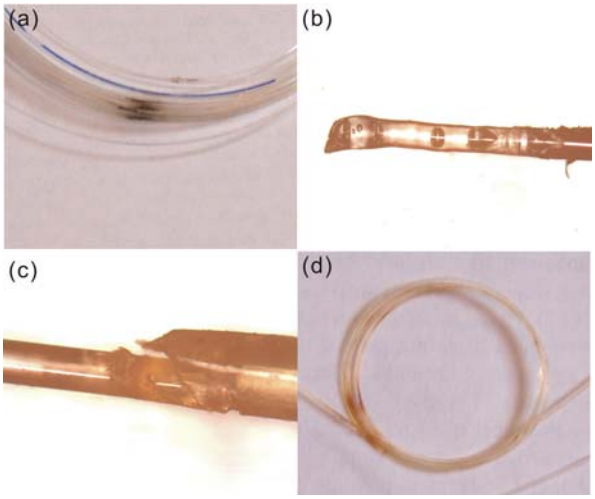

Figure 4.8: Examples of thermal damage to fibers

In practice, thermal damage to optical fibers can be managed by using a suitable heat-sink arrangement and optimization of the pump launch efficiency. In this research, I avoided thermal damage in CPA systems that could generate more than 150 W of average power.

4.6.5 Self-focusing

Self-focusing occurs due to the intensity dependence of the refractive index, which ultimately limits the pulse peak power in fiber amplifiers. Self-focusing is characterized by a critical power above which the optical beam will collapse, creating very high peak intensities and causing damage to the fiber. The critical power for self-focusing is not spot-size dependant, so the effect is unchanged whatever fiber core size is used. For an optical silicate fiber, the critical power of self-focusing is estimated to be ~4 MW according to [14] and [15]. In our fiber amplifiers, where the stretched pulse duration is ~1 ns, the corresponding pulse energy for self-focusing threshold is ~4 mJ. Self-focusing was not observed in any of the experiments in this thesis research.

4.6.6 Energy-saturation

The extractable pulse energy from a fiber amplifier is limited to a few times (~10) the saturation energy, given by

$$E_{sat} = \frac{h\upsilon A}{\sigma_e + \sigma_a} \tag{4.2}$$

where h is the Planck constant, υ is the signal frequency, A is the fiber effective mode area, σ_e and σ_a are the emission and absorption cross-section of the signal. It can be estimated from Equation (4.2) that the saturation energies of the 20 μm core diameter LMA fiber and the 40 μm core diameter PCFs are approximately 0.1 mJ and 0.4 mJ, respectively. As the saturation energies of the fibers are beyond the threshold of nonlinear effects, this is not a limitation for the results presented in this thesis.

4.6.7 Photo-darkening

Photo-darkening presents itself as a long term temporal decay of output power, which could be attributed to the formation of color centers or other photo-induced structural transformations in the silica glass host associated with defects [16]. Photo-darkening is usually regarded as a limiting factor for the long-term stability of fiber laser systems. This was not a limitation for the results presented in this thesis, due to the careful choice of glass hosts and Yb concentrations of the fibers that we used, and the time scale over which our systems were run.

4.7 Conclusion

The detailed development work on the fiber CPA system has formed the major part of this PhD thesis research. This Chapter provided an overview of the fiber CPA systems in this thesis research, including a system schematic, component characteristics, and other technological challenges that are common to both the high average power and the high pulse energy versions of the CPA system.

The following Chapters will provide details of these systems designed for different technological approaches. Chapter 5 describes the design and realization of a high average power CPA system using a CFBG stretcher and dielectric compressor. The development of a high pulse energy system using a dielectric grating stretcher and compressor are described in Chapter 6. Next, a fiber CPA system incorporating adaptive phase control is reported in Chapter 7.

Reference:

[1] L. Lefort, J. H. V. Price, D. J. Richardson, G. J. Spuhler, R. Paschotta, U. Keller, A. R. Fry, and J. Weston, "Practical low-noise stretched-pulse Yb^{3+}-doped fiber laser," *Optics Letters*, vol. 27, pp. 291-293, 2002.

[2] M. E. Fermann, A. Galvanauskas, and G. Sucha, *Ultrafast lasers : technology and applications*. New York: Marcel Dekker, 2003.

[3] M. Ibsen, M. K. Durkin, M. J. Cole, M. N. Zervas, and R. I. Laming, "Recent Advances in Long Dispersion Compensating Fiber Bragg Gratings," *IEE Colloquium on Optical Fiber Gratings, (Ref. No.1999/023)*, pp. 6/1-7, 1999.

[4] A. W. Snyder and J. Love, *Optical Waveguide Theory*: Springer, 1983.

[5] J. Senior, *Optical Fiber Communications*, 2nd ed. New York Prentice Hall 1992.

[6] J. P. Koplow, D. A. V. Kliner, and L. Goldberg, "Single-mode operation of a coiled multimode fiber amplifier," *Optics Letters*, vol. 25, pp. 442-444, 2000.

[7] T. Schreiber, F. Röser, O. Schmidt, J. Limpert, R. Iliew, F. Lederer, A. Petersson, C. Jacobsen, K. Hansen, J. Broeng, and A. Tünnermann, "Stress-induced single-polarization single-transverse mode photonic crystal fiber with low nonlinearity," *Optics Express*, vol. 13, pp. 7621-7630 2005.

[8] B. E. Saleh and M. C. Teich, *Fundamentals of photonics*. New York: Wiley-interscience publication, 1991.

[9] Y.-H. Chuang, D. D. Meyerhofer, S. Augst, H. Chen, J. Peatross, and S. Uchida, "Suppression of the pedestal in a chirped-pulse-amplification laser," *Journal of Optics Society of America B*, vol. 8, pp. 1226-, 1991.

[10] M. D. Perry, T. Ditmire, and B. C. Stuart, "Self-Phase Modulation in Chirped-Pulse Amplification," *Optics Letters*, vol. 19, pp. 2149-2151, 1994.

[11] T. Schreiber, D. Schimpf, D. Muller, F. Roser, J. Limpert, and A. Tunnermann, "Influence of pulse shape in self-phase-modulation-limited chirped pulse fiber amplifier systems," *Journal of the Optical Society of America B-Optical Physics*, vol. 24, pp. 1809-1814, 2007.

[12] A. C. Tien, S. Backus, H. Kapteyn, M. Murnane, and G. Mourou, "Short-Pulse Laser Damage in Transparent Materials as a Function of Pulse Duration," *Physical Review Letters*, vol. 82, pp. 3883-3886, 1998.

[13] B. C. Stuart, M. D. Feit, S. Herman, A. M. Rubenchik, B. W. Shore, and M. D. Perry, "Optical ablation by high-power short-pulse lasers," *Journal of Optics Society of America B*, vol. 13, pp. 459-468, 1996.

[14] R. W. Boyd, *Nonlinear Optics*, 2nd ed: Academic Press, 2002.

[15] G. Fibich and A. L. Gaeta, "Critical power for self-focusing in bulk media and in hollow waveguides," *Optics Letters*, vol. 25, pp. 335-337, 2000.

[16] J. J. Koponen, M. J. Soderlund, H. J. Hoffman, and S. K. T. Tammela, "Measuring photodarkening from single-mode ytterbium doped silica fibers," *Optics Express*, vol. 14, pp. 11539-11544, 2006.

Chapter 5 High average power femtosecond fiber CPA system

Due to the outstanding thermal-optical properties, and other advantages presented in Chapter 2, Yb-doped fibers offer a promising technology for generating high energy femtosecond pulses at repetition rates that extend beyond the limits of conventional solid-state laser sources. For example, milliJoule, femtosecond laser sources that are capable of operating at 100 kHz - 1 MHz repetition rates, and hence at high average powers of 100 W - 1 kW, could benefit many industrial and scientific applications. Therefore, the demonstration of average power scaling of CPA systems with Yb-doped fiber and diode pump technology is potentially very significant and useful.

This Chapter presents the development of an Yb-fiber CPA system, incorporating several state-of-the-art technologies, for producing high quality femtosecond pulses at high average powers. A critical component in the system is the dielectric grating compressor which has the advantages of high power handling, compared to gold gratings, but without the size constraints associated with fused silica transmission gratings. This dielectric grating was loaned by LLNL while we were waiting for our own grating to be fabricated in their facilities. A compact stretcher, based on CFBG technology, was used in the system, and high quality recompressed pulses were obtained by the careful design and characterization of the CFBG stretcher to match up to 3rd order dispersion of the compressor. The Yb-fiber amplifier chain was designed to optimize the output bandwidth using the modeling tools described in Chapter 3. The system produced 135 W after the amplifier chain, at 10 MHz pulse repetition rate (13.5 μJ pulse energy), and the recompressed pulse duration was 360 fs.

This Chapter is organized as follows. The system schematic is introduced first in section 5.1, followed by the description of the design and characterization of the CFBG stretcher in section 5.2. The development of the power amplifier, with high output average power, is presented in section 5.3. Section 5.4 describes the design and experimental setup of the dielectric grating based compressor. The experimental results achieved in this system are shown in section 5.5. Finally, section 5.6 provides a brief summary.

5.1 Experimental setup

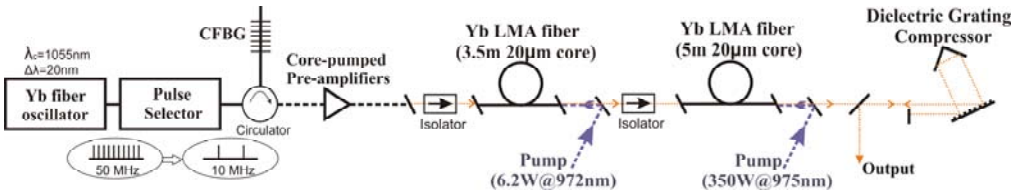

Figure 5.1: Fiber CPA system schematic

The schematic of the fiber CPA system is shown in Figure 5.1 [1]. The passively mode-locked, diode-pumped, Yb-doped fiber seed laser provided < 150 fs pulses, with ~20 nm bandwidth, centered at 1055 nm, and was presented in detail in Chapter 4. An EOM was used as a pulse selector to reduce the pulse repetition rate from 50 MHz to 10 MHz. The pulses were then coupled into a CFBG, using a commercial fiberized circulator from General Photonics Inc. The CFBG, which was designed, fabricated, and characterized in the ORC, is described in Section 5.2. Pulses were stretched to ~1.8 ns duration, with 0.01 mW average power, after the CFBG.

Two core-pumped pre-amplifiers were used to increase the pulsed signal average power to ~0.1 W before launching into the high power, cladding-pumped, amplifiers. The two pre-amplifiers consisted of ~2 m Yb-doped single-mode fiber, forward pumped by ~300 mW laser diodes at 976 nm. Two stages of power amplifier were used with the double-clad fibers (core diameter 20 μm, NA 0.06; inner cladding diameter 180 μm, NA 0.5) that were fabricated in ORC. The first power amplifier consisted of a 3.5 m fiber and was backward pumped by a 972 nm, 6.2 W laser diode with 100 μm core diameter, 0.22 NA, delivery fiber. The final amplifier used 5 m of fiber and was backward pumped by a 975 nm, 350 W laser diode with 400μm core diameter, 0.22 NA, delivery fiber. Isolators were incorporated between the amplifiers to prevent backward ASE. Finally, a dielectric, grating-based compressor with a Treacy configuration was used in the system [2]. The grating compressor setup was aligned and characterized at the ORC, which is presented in detail in Section 5.4.

5.2 CFBG design and characterization

To design the dispersion characteristics of the CFBG, I first calculated the dispersion of the grating compressor by using a ray-tracing method provided by LLNL. The calculated dispersion ($D \times Length$) and 3rd order dispersion ($dD/d\lambda \times Length$) terms of the compressor are 191.75 ps/nm and 5.34 ps/nm^2 respectively, based on the use of a grating

incident angle of 76.5° as recommended by LLNL for high efficiency operation, and an effective grating separation of 154.6 cm. The simulation assumes that there is no dispersion or nonlinear phase shift in any of the amplifiers because these contributions are <0.5% of the grating compressor dispersion. Therefore, the required dispersion parameters in the CFBG are then simply matched with those from the compressor.

Three CFBGs, labeled as CFBG1, CFBG2 and CFBG3, were fabricated at the ORC by Dr. M. Ibsen, according to my design requirements. To test the accuracy and quality of the CFBGs, I characterized the reflectivity and dispersion for all of the CFBGs, which will be discussed in the following sections.

5.2.1 Characterization of CFBG reflection spectra

The reflection spectra of the CFBGs were measured by using pulses from the mode-locked oscillator as a broadband source, as shown in Figure 5.2.

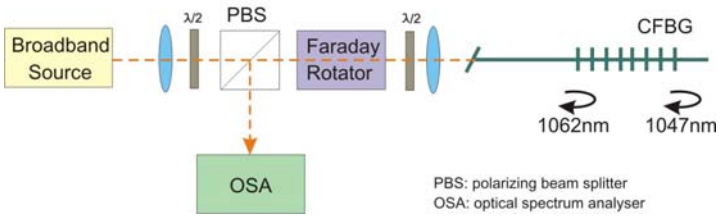

Figure 5.2: Schematic of CFBG reflection spectrum measurement

When using the CFBG as a pulse stretcher to match grating compressor, low frequency (red) components will be coupled into the backward core mode at the beginning of the CFBG, while high frequency (blue) components will be coupled into the backward mode at the end of the CFBG. The high frequency (blue) components suffer from power transfer to cladding modes during their propagation in the CFBG [3]; therefore high frequency (blue) components have a weaker reflection than low frequency (red) components, which results in an uneven reflection spectra across the transmission window of the CFBG when it is oriented to provide normal dispersion as shown in the figure.

In order to control the cladding mode loss, Dr. M. Ibsen reduces the CFBG reflectivity by annealing the grating after writing. A weaker grating scatters less of the high frequency (blue) power to the cladding modes, and should therefore give a generally flatter spectral response [4]. Figure 5.3 shows the results of my measurements. Figure 5.3 (a) shows the normalized reflection spectra. The measurement resolution of the OSA

is 0.01 nm, and the reflectivity of the three CFBGs is ~70%. CFBG1 gives a narrower spectral window with more variations than the other two CFBGs. The polarization sensitivities of the three CFBGs are measured in the setup shown in Figure 5.2. Figure 5.3 (b) illustrates the change of the reflection spectrum of CFBG2 with three different input polarization angles, controlled by adjusting the half wave plate before the CFBG. The strong spectral modulations, observed with the input polarization at 45 degrees to the CFBG fiber axis, are due to the high birefringence of the fiber. Similar performance is observed for CFBG1 and CFBG3. Therefore, special care about the input polarization is taken when using these CFBGs.

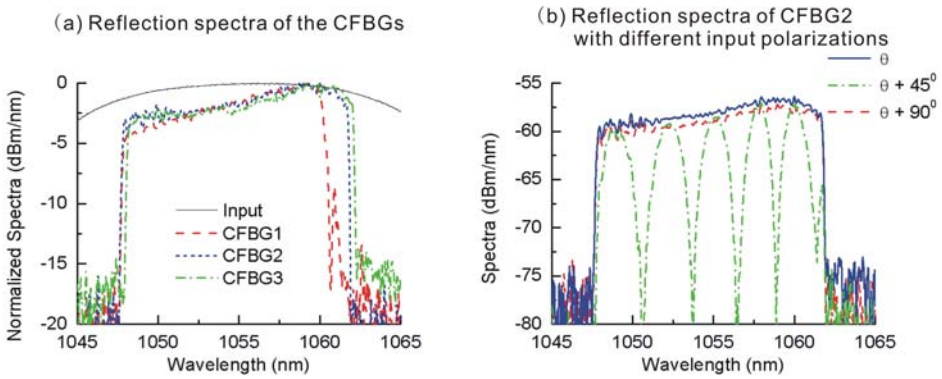

Figure 5.3: (a) normalized reflection spectra of three CFBGs used in CPA system (the input spectrum is showed for reference), and (b) reflection spectra of CFBG2 with three input polarization angles.

5.2.2 Tunable source for CFBG dispersion characterization

In order to measure the dispersion, I developed a wavelength tunable source operating around ~1 μm. Figure 5.4 shows the schematic of the 1034-1075 nm tunable source. The 2 m Yb-doped fiber is pumped by a ~280 mW diode laser, at 977 nm, through a WDM coupler. The backward ASE (~30 mW), generated by the Yb-doped fiber, is filtered by the Acousto-Optic Tunable Filter (AOTF) and then reflected back by a high reflectivity (HR) mirror. The filtered signal is then amplified as it propagates through the pumped Yb-doped fiber. An angle-polished end is used as the output end, to prevent the 4% Fresnel reflection which would otherwise cause pulsed lasing in the system.

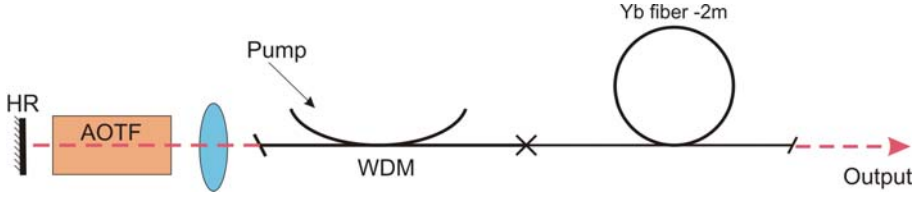

Figure 5.4: Schematic of wavelength tunable source

The performance of this tunable source is shown in Figure 5.5. Stable CW output with 1~12 mW power, tunable in the range of 1034nm-1075nm, is produced (the typical spectral window of the CFBGs is 1044-1064 nm).

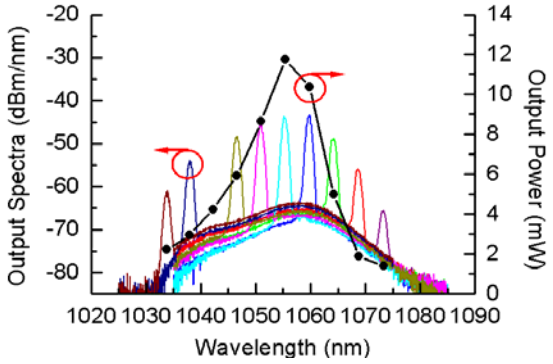

Figure 5.5: Output power and spectra of the ASE based wavelength tunable source

5.2.3 CFBG dispersion measurements

A network analyzer is used to measure the phase shift with different input wavelengths, as illustrated by Figure 5.6. The CW beam from the tunable source is first modulated at 1 GHz by the EOM. The modulated signal then passed through an optical circulator, with the CFBG inserted, and the reflected signal is collected by a photo-diode at the output. The network analyzer then measures the phase shift between the driving carrier frequency and the received signal after the circulator as a function of wavelength.

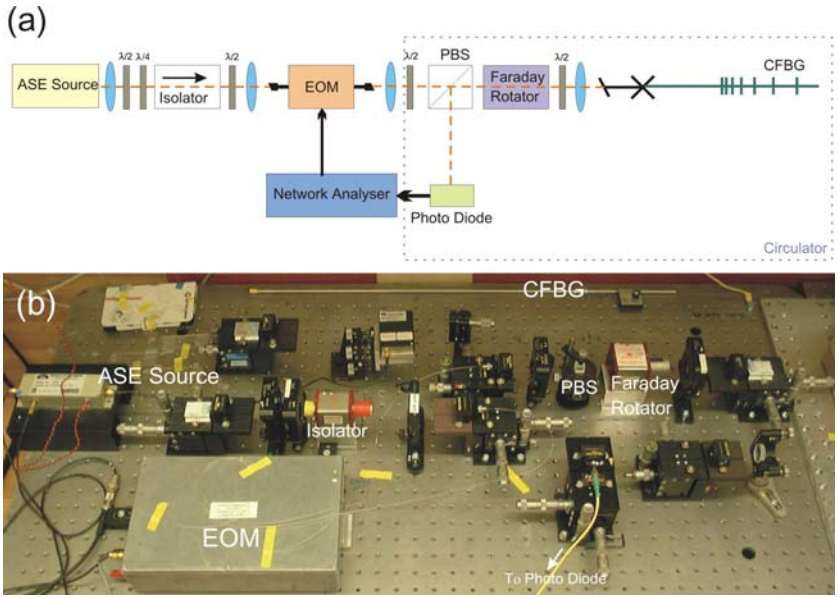

Figure 5.6: (a) Schematic of dispersion measurement and (b) corresponding experimental setup in the lab

The group delay is calculated from the measured phase shift data using the following relation

$$\Delta\tau = (\Delta\phi / 360)(1 / F_{carrier}) \tag{5.1}$$

where $\Delta\phi$ is the measured phase shift in degrees, $F_{carrier}$ is the carrier frequency modulated by the EOM.

The noise of the dispersion measurement setup is characterized by replacing the CFBG with a HR mirror. Figure 5.7 shows the measured delay across the wavelength tuning range. The results show that the experimental setup (Figure 5.6) can contribute ±7 ps error to the measurement of CFBG dispersion.

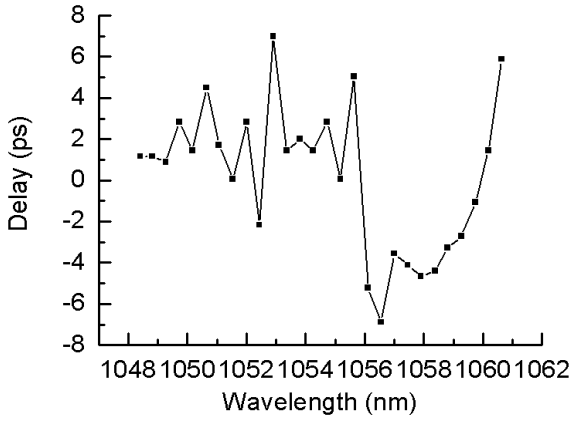

Figure 5.7: Delay measurement results with a high reflection mirror in the setup

The dispersion can be calculated by analyzing group delay vs. wavelength data. The effects of the dispersion ($D \times Length$) and the 3rd order dispersion ($dD / d\lambda \times Length$) can be calculated using the following equations

$$D \times Length = \frac{dDelay}{d\lambda} \quad (ps / nm) \tag{5.2}$$

$$\frac{dD}{d\lambda} \times Length = \frac{d^2 Delay}{d\lambda^2} \quad (ps / nm^2) \tag{5.3}$$

Table 5.1 summarizes the measured dispersion values of the three CFBGs, and small variations from the design can be seen from the table. Both the effects of the dispersion ($D \times Length$) and the 3rd order dispersion ($dD / d\lambda \times Length$) of a bulk grating compressor are proportional to the grating separation, which can be easily adjusted by moving the compressor roof mirror position in our compressor (with the Treacy configuration). Therefore, the differences in the dispersion ($D \times Length$) between the CFBG stretchers and the compressor can be compensated by adjusting the compressor

separation. However, it is not possible to totally compensate both the dispersion ($D \times Length$) and the 3rd order dispersion ($dD/d\lambda \times Length$) differences by changing the compressor separation, unless the ratios of these are matched to the compressor. Note that, although possible, it is not practical to adjust the ratios between the dispersion ($D \times Length$) and the 3rd order dispersion ($dD/d\lambda \times Length$) of the compressor by changing the compressor layout. In the three CFBGs listed in Table 5.1, CFBG1 is expected to provide the lowest residual 3rd order dispersion ($dD/d\lambda \times Length$) when the compressor separation is adjusted to match the chromatic dispersion.

Table 5.1: CFBG design and characterization results

Label	**Dispersion (ps/nm)**	**3rd order dispersion (ps/nm^2)**	**Ratio between dispersion and 3rd order dispersion values**	**Operating spectral window (nm)**
Design	-191.75	-5.34	35.908	1048.0-1062.0
CFBG1	-195.41	-6.65	29.385	1048.5-1060.5
CFBG2	-194.18	-6.92	28.601	1047.7-1061.9
CFBG3	-194.38	-6.99	27.808	1048.0-1062.2

Figure 5.8 summarizes the reflection spectra and dispersion characteristics (left column of graphs) of the three CFBGs. Measured points are shown as blue squares and are compared with the design which is illustrated as a red solid line. Reflection spectra are shown as black lines. Output pulses of the CPA system have been characterized by incorporating these three CFBGs as the stretchers and using the dielectric grating compressor. The experiments are performed when the CPA system is operating at a relatively low power (~1 W), with full repetition rates (~50 MHz), to avoid nonlinear distortions from the amplifiers. The compressor grating has a groove density of 1778.5 groove/mm. With an incident angle of 76.5° and an effective separation of 154.6 cm, the compressor provides the dispersion ($D \times Length$) and the 3rd order dispersion ($dD/d\lambda \times Length$) parameters of 191.75 ps/nm and 5.34 ps/nm^2 respectively. The autocorrelation traces of the recompressed pulses are measured and are presented in Figure 5.8 (central column of graphs). The grating separation is adjusted slightly to maximize the autocorrelation peak in the measurements. The spectra measured before and after the compressor are shown in Figure 5.8 (right column of graphs).

As shown in Figure 5.8, pulse pedestals appears in the recompressed pulses with the use of the three CFBG stretchers; the pedestals originate from a combination of mismatched 3rd and 4th order dispersion from the stretcher and the compressor, the phase errors introduced by the CFBG, and the accuracy of the CFBGs and dielectric grating characterization.

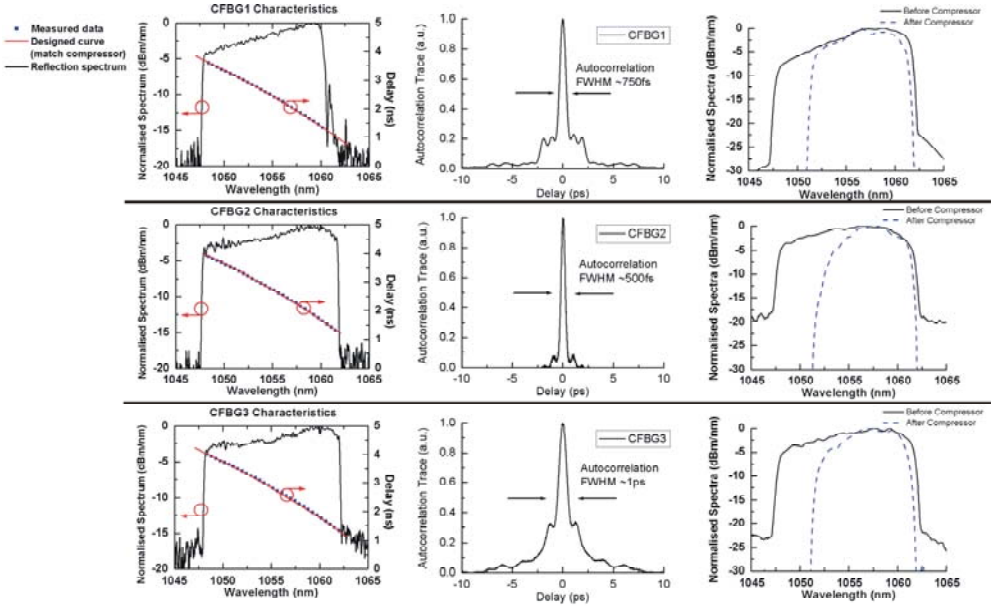

Figure 5.8: Experimentally measured CFBG characteristics (left column), autocorrelation traces of the recompressed pulses (central column), and spectra before and after compression (right column).

Of the three CFBGs, CFBG1 provides the best dispersion characteristics with respect to the ratio between the dispersion ($D \times Length$) and the 3rd order dispersion ($dD/d\lambda \times Length$) (Table 5.1), but the worst spectral characteristics with respect to the spectral window and the variation across the window (Figure 5.3). CFBG2 and CFBG3 have similar spectral characteristics, but CFBG2 provides better dispersion characteristics than CFBG3. Therefore, although difficult to predict with high precision, it is not surprising to see that CFBG2 provides the recompressed pulse with the shortest width and minimum pedestal in the experiment. Hence CFBG2 has been used in the following high power experiments. The pulses after the CFBG2 stretcher are measured to be approximately 1.8 ns (FWHM) by using a Tektronix 10 GHz fast photo detector and a Tektronix CSA 803A communications signal analyzer which is designed for viewing optical pluses up to 50 GHz.

5.3 High average power LMA fiber amplifier

This section will present the performance of the final stage power amplifier, and discuss issues specifically related to the realization of high average output power from this amplifier. General properties of fiber amplifiers have been presented in Chapter 3 and 4.

5.3.1 High average power pump diodes

High output average power from the fiber amplifiers in this system is realized by the use of a 975 nm, 350 W laser diode. The pump laser is a commercial product from Laserline Inc., as shown in Figure 5.9. Pump power from the diode stacks is coupled into a 400 μm diameter multimode delivery fiber, with NA of 0.22. Collimation lenses, focusing lenses, and a protective glass window are mounted in a metal tube, which is connected to the output end of the delivery fiber and avoids the hotspot at the fiber end being exposed to contamination. The output beam is focused to a 400 μm diameter spot, with NA of 0.2, at a distance of 85 mm from the front of the beam delivery package.

Figure 5.9: 350 W diode laser module from Laserline Inc. Rack-mountable integrated fiber coupled diode stack and power supply unit (below) and beam delivery package (above). (photo from www.laserline-inc.com)

5.3.2 Zemax simulations of pump-coupling

In my applications, the pump power from the Laserline laser diode module is going to be coupled into the inner cladding of the LMA fiber, which has diameter of 180 μm and NA of 0.5. High launching efficiency is required; otherwise un-launched pump power will cause thermal damage.

A number of issues have to be considered in the launching optical system design. Firstly, two dichroic mirrors have to be placed in the pump launching path. One of the

dichroic mirrors is used for coupling the signal beam into the fiber core, as the high power LMA fiber amplifier is designed to be forward pumped. The other dichroic mirror is used for protection of the pump diode from the backward ASE of the amplifier. Secondly, an aspheric lens should be used for coupling the pump and signal beam into the LMA fiber, due to its advantage over a conventional lens regarding spherical aberrations [6]. Therefore, the optical design becomes a complex problem because the aperture of the lens and the dichroic mirrors, as well as the amount of pump power on their mounts, has to be considered. Also it is not possible to practice the launching in an experiment at a low power mode because the pump laser threshold power is ~5 W. In addition, the rapidly diverging beam adds to the experimental difficulty of aligning the delivery optical package. Therefore, simulations are required in the designs for the pump launching optics.

Zemax is a program that can be used to assist the design of various optical systems, including lens design, illumination, laser beam propagation, stray light, and fiber optics. Zemax has a powerful optimization tool, which is capable of improving multi-element lens designs given a reasonable starting point and a set of variable parameters. The optimization uses an actively damped least squares method, in which the algorithm is capable of optimizing a merit function composed of weighted target values [7].

Zemax has been used in my optical launch system design. My first step was to create an optical system in Zemax. As shown in Figure 5.10, the system consisted of three lenses and two dichroic mirrors. A negative lens was used to collimate the beam to avoid a pump focus, an aspheric lens was used for coupling pump and signal light into the fiber, and an additional lens used to reduce the beam size onto the aspheric lens. A ray-tracing simulation was used in my application. Note that Zemax also provides physical optics propagation simulations which could be more suitable for my application. However, at the time when I did the work, I found that such simulations were not straight forward to set up for a highly multimode Gaussian input beam, therefore it was not used in my application.

After the system was created, I used the optical beam from the Laserline pump diode as the input. For a close match to the experimentally measured beam profile of the pump light (high order super-Gaussian shape), a uniform distribution of the pump beam profile was used in the simulations. As shown in Figure 5.10, five traces were used in Zemax model to represent the optical beam, with the top (green) and bottom (red) traces representing the input beam with the highest divergence (NA of 0.22). The position and the focal length of the lenses in the system were set as variables (the range for each variable was set to ensure that the optimized values are reasonable). The Zemax merit

function was set to minimizing the focused beam size to the inner-cladding size of the Yb-doped LMA fiber (180 μm), and to minimizing the divergence of the focused beam to the NA of the Yb-doped LMA fiber (0.5). The same weight was used for the beam size and divergence optimizations in the merit function, as they were both important to the coupling efficiency. The optimized lens parameters and position were predicted by the simulations.

In the next step, I chose lenses from Thorlabs Inc. (www.thorlabs.com) with a close match to the optimized parameters. The lenses that have been chosen were input into the model, and their parameters were treated as fixed parameters. The positions of the lenses (as variables) were re-optimized using the same Zemax merit function as described above. A number of issues were considered in further simulation investigations. The mounts for the optical components were included in the model. The overall length of the optical launching setup was minimized for compactness. The sensitivity of the position of each component was also investigated to assist experimental alignment.

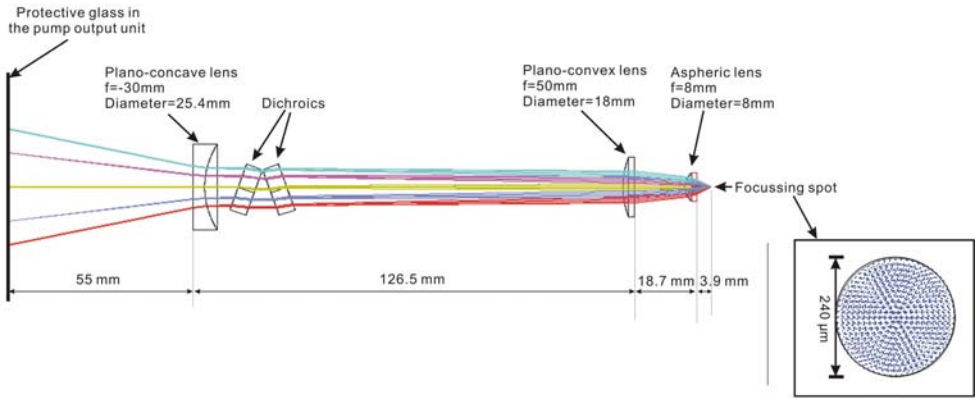

Figure 5.10: Schematic of the pump launching optics

Figure 5.10 shows the simulation output after the optimization described above. The optimized parameters of each component are illustrated in the figure. The simulations predicted that the pump beam from the diode laser can be focused into a fiber with a diameter >240 μm and NA >0.3 in such a setup. Limited by the commercial lens choice, further reduction of focused beam size to 180 μm (Yb-doped LMA fiber core diameter) is predicted to be not feasible.

The design was verified experimentally by using 0.5 m of multimode passive fiber with a core diameter of 200 μm and a NA of 0.22. Relatively low launch efficiency was expected due to the fact that core size of the fiber is smaller than the size of the focused pump beam, and also because the acceptable angle of the fiber is lower than the

divergence of the focused pump beam. The measured launching efficiency was ~65%, as expected. The Yb-doped LMA fiber used in the final amplifier has a smaller inner cladding diameter (180 μm) than the diameter of the focused pump beam (240 μm), but the acceptance angle of the fiber (NA~0.5) is larger than the divergence of the focused pump beam (NA~0.3). The pump launching efficiency into the Yb-doped LMA fiber is measured to be ~70%. Note that the fiber end is water cooled, and that I observed melting/burning of the fiber ends and/or fiber coatings when the pump launching was not optimized.

5.3.3 Fiber properties

The power amplifier used 5 m of 20 μm core LMA fiber, which was fabricated at the ORC, with the index profile and doping distribution design as presented in Chapter 2. Table 4.1 lists the detailed parameters of this fiber. The fiber is coiled to a 20 cm diameter and the input signal launch is optimized to provide the near diffraction limited output beam quality. Figure 5.11 shows the measured beam waist, after the output beam was focused by a plano-convex lens, with a 500 mm focal length. The M^2 value is calculated to be 1.06.

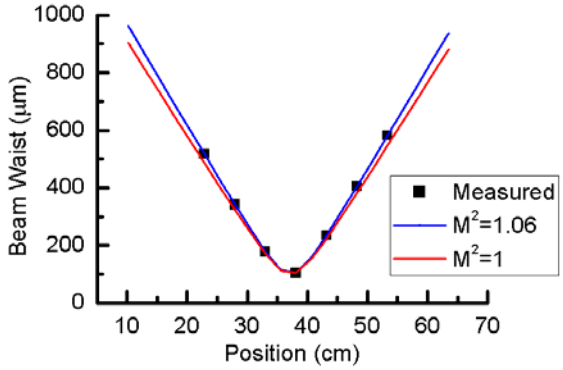

Figure 5.11: Mode quality measurement of the Yb-doped fiber used in the final amplifier

The inner cladding diameter of the double-clad fiber, which has to be sufficiently large to allow for efficient pump coupling, is 180 μm. The low overlap ratio (~1.2%), of the cross sectional area between the pump and the signal, leads to the pump absorption of ~7 dB/m at 975 nm. Therefore, 5 m of the fiber is used in the final amplifier to provide sufficient pump absorption for the 350 W pump power.

Figure 5.12 shows the output power versus the launched pump power in the amplifier. The maximum power of 135 W corresponds to a slope efficiency of 77 %, with respect to

the launched pump power. The launched signal has an average power of ~0.5 W, pulse repetition rate of 10 MHz, and spectral bandwidth of ~10 nm centered at 1055 nm. The gain is ~24 dB at the maximum output power.

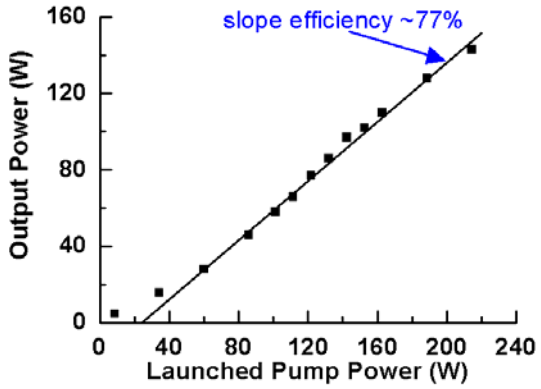

Figure 5.12: Output power characterization of the final Yb-fiber amplifier in the CPA system

5.4 Dielectric grating compressor

The grating in the compressor is exposed to the full beam average power and pulse energy in the ultrashort pulse regime. The optimal technology for high power, short pulse, grating compressors is the multilayer dielectric grating. A brief introduction to dielectric gratings is provided in Appendix II.

Figure 5.13 (a) shows the layout of the compressor. The design is based on a single dielectric grating in a double-pass, folded, Treacy configuration, in which the beam diffracts from the grating four times [2]. Horizontal and vertical roof mirrors have been used to translate the beam to enable only one grating to be used. The setup has the advantage that, with the roof mirrors carefully aligned, the grating "pair" is always parallel, and therefore the grating separation parameter can be adjusted by sliding the horizontal roof mirror forward or backward in relation to the grating. The experimental setup can be seen in Figure 5.13 (b). The grating has surface dimensions of 20x10 cm. The groove density is 1778.5 grooves/mm, which corresponds to a Littrow angle of 69.9 degrees for a 1056 nm input beam. The designed incident angle is 76.5 degrees in the compressor setup, which gives a diffracted angle of 64.9 degrees for an input signal at 1056 nm.

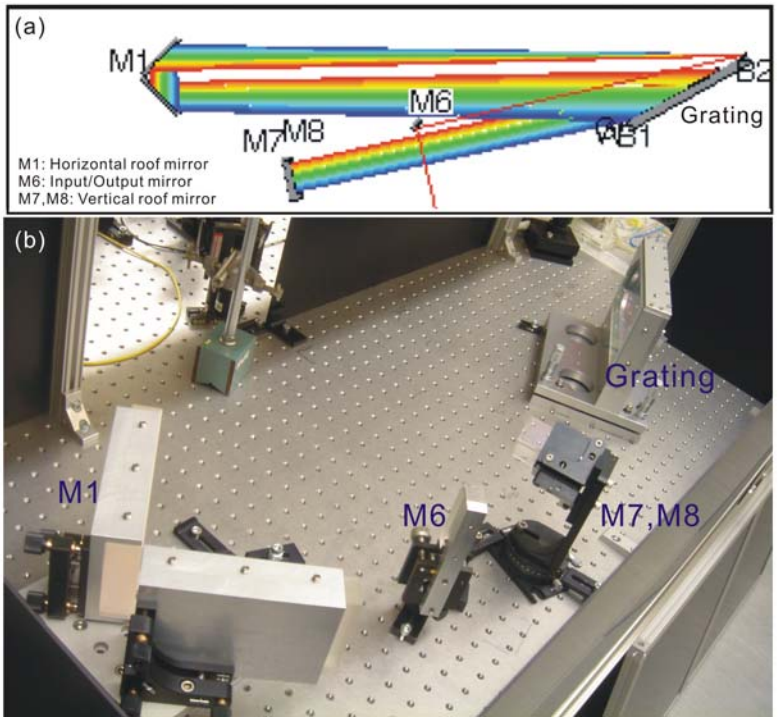

Figure 5.13: (a) compressor design layout and (b) compressor setup in the experiment

A narrow bandwidth (<0.01 nm, FWHM), tunable (1025-1080 nm), CW laser from Sacher Lasertecknik Group is used for compressor alignment. The grating was mounted and then the tip (orientation of the grating surface) and tilt (orientation of the grating grooves) adjustments are performed [8]. The roof mirrors are first aligned separately to ensure that the output beam is parallel to the input beam. The designed propagation lines for the desired laser beam, centered at 1055.30 nm, are scribed onto the optical bench. The tunable laser is then set to 1055.30 nm center wavelength, and the beam aligned on the input beam line. The grating and the roof mirrors can therefore be aligned in the setup according to the real beam and the scribed lines. The spatial chirp of the compressor is measured by tuning the input beam wavelength while monitoring the output position with a camera. Figure 5.14 (a) shows that, before the adjustment, the short wavelength (1049 nm) output beam is in a different position, with respect to the long wavelength (1061 nm) beam. This far-field difference can only be due to a diffractive error. To first order, a horizontal (i.e. in the reference, or dispersion plane) angular dichroic difference is due to a misalignment of the grating surface parallelism, however, a vertical difference (i.e. perpendicular to the reference plane) is a groove parallelism error (due to small variation in the tip/tilt adjustments of the two gratings) [9]. After careful adjustment of the horizontal roof mirror, the spatial chirp is minimized, as shown in Figure 5.14 (b).

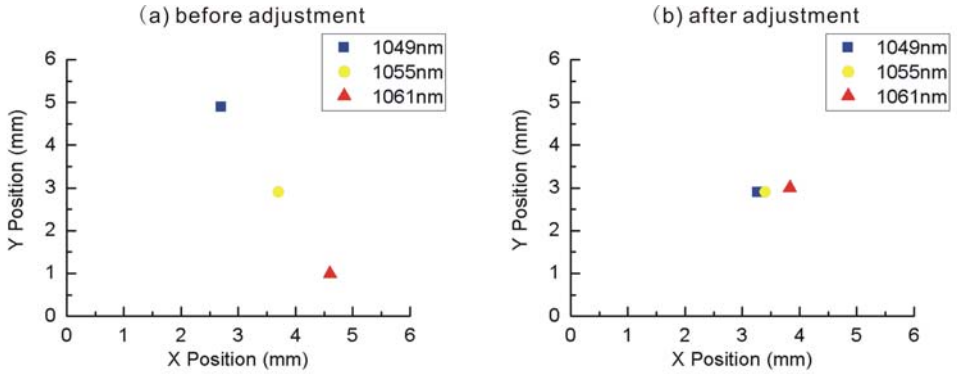

Figure 5.14: Grating compressor spatial chirp minimization

The quality of the compressor output beam was measured as further evidence of good alignment of the compressor. Figure 5.15 shows the measured beam waist, after the output beam was focused by a plano-convex lens with 1 m focal length. The M^2 value is calculated to be 1.2. The inset of Figure 5.15 illustrates the beam profile near the focus.

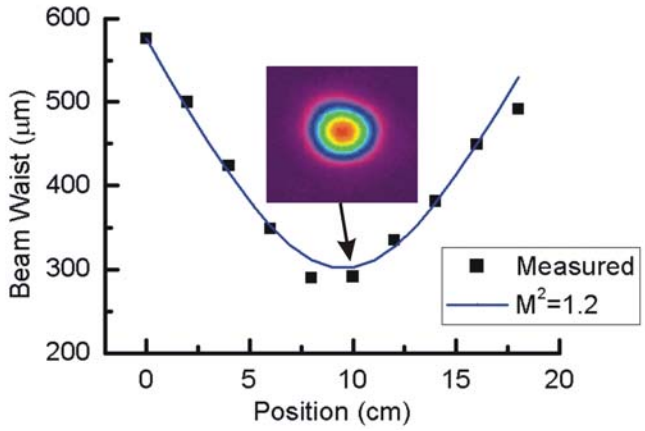

Figure 5.15: Mode quality measurement of the CPA system output

The 20 cm long grating is designed to provide a 10 nm spectral window in the compressor, which fitted our initial expectations of the output pulse spectra. However, the gain bandwidth optimization then progressed such that the signal spectral window from the amplifiers is more than 13 nm, and thus a 26 cm grating would then be necessary. As a consequence, spectral clipping is observed due to the limited grating size, of 20 cm, in the setup. Therefore, although the grating provides diffraction efficiency as high as 95% for a single pass, the measured overall transmission of the compressor is 52%. However, spectral clipping can easily be removed in my system by using larger gratings, because further scaling of the dielectric grating size is not limited at 20 cm (meter-scale dielectric gratings have been used in some high power laser facilities [10-12]). In addition, scaling of the grating size provides the ability to apply a larger

stretching/compressing ratio in the CPA system. In Chapter 6 and 7, I will present the application of a 35 cm dielectric grating, with ~95% single pass diffraction efficiency, which provides an overall compressor efficiency of ~65% in the CPA system together with larger stretching/compressing ratios than the current setup.

5.5 Experimental results

In order to achieve high average powers with a good pulse quality, and at the same time the highest possible pulse energy, the CPA system is operated at the point where the pulse energy is just below the nonlinear threshold of the fiber amplifiers. Therefore, the pulse repetition rate of the oscillator is tuned down to 10 MHz, by using the EOM pulse selector, before the fiber amplifiers. Figure 5.16 shows the autocorrelation traces at different pulse energies, measured by using an autocorrelator (FR-103 from Femtochrome Research Inc.) with a 300 μm thickness BBO crystal. The autocorrelation width remains constant at 510 fs, corresponding to a pulse width of 360 fs, assuming a Gaussian shape. The measured time bandwidth product ($\Delta\nu\Delta\tau$) was ~0.6. An increase of the autocorrelation pedestal is observed with the increase of pulse energy to 13.5 μJ (pulse average power of 135 W at 10 MHz repetition rate) in the final amplifier, but the majority of the energy remained in the central peak. The estimated B-integral is ~π at full power. The measured compressor transmission efficiency of 52% indicates maximum compressed output pulse energy of 7 μJ with an average power of 70 W.

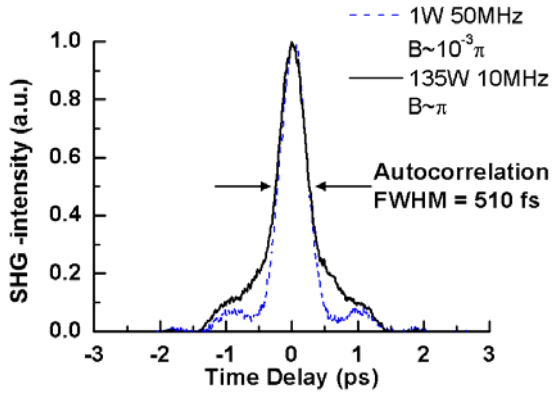

Figure 5.16: CPA system output pulse autocorrelation traces at low and high pulse energies.

The spectral characteristics of the CPA system are shown in Figure 5.17 (a). The CFBG stretcher provides a 14 nm spectral window. The pulse spectrum FWHM is about 12 nm after the stretcher, and most of the bandwidth is maintained through the amplifier

chain. At 135 W output power, the signal remains 20 dB above the ASE level. The compressed pulse spectrum had a FWHM width of 6.2 nm. Calculated autocorrelation traces, made by using a fast Fourier transform (FFT) of the spectra before and after the compressor with a flat phase, are shown in Figure 5.17 (b), together with the experimental data. Good agreement between experimental data and the calculation from the FFT of the output spectra confirms the well matched dispersion between stretcher and compressor in the CPA system without nonlinear distortions. The FFT of the compressor input spectrum implies that pulse widths as short as 210 fs could be achieved if spectral clipping in the compressor was avoided.

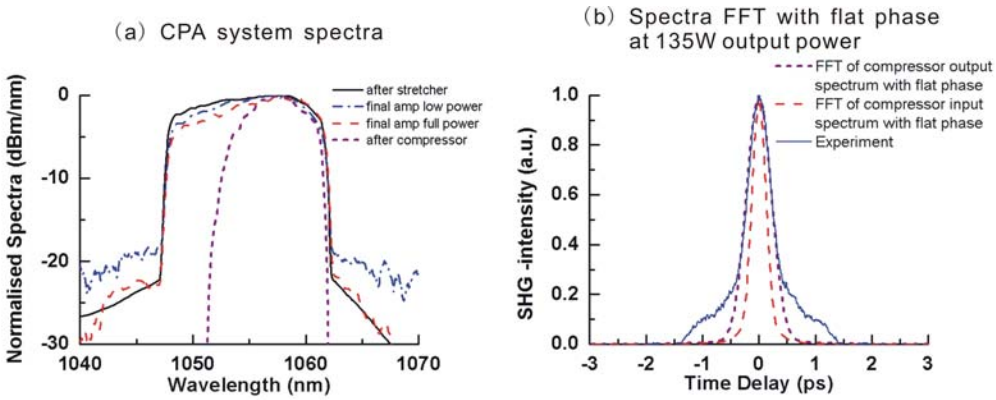

Figure 5.17: (a) spectra of the pulses before and after the grating compressor at 135 W output power; (b) measured and calculated autocorrelation traces (using FFT of spectra with flat phase)

Figure 5.18 shows the temporal and spectral characteristics of the pulses at reduced repetition rates. More severe pulse distortions at pulse energies above 40 μJ (before compression) are evident in Figure 5.18 (a). The estimated threshold for stimulated Raman scattering is ~100 μJ (before compression), and the Raman pulse is observed experimentally at a pulse energy of ~ 200 μJ (before compression), as shown in Figure 5.18 (b).

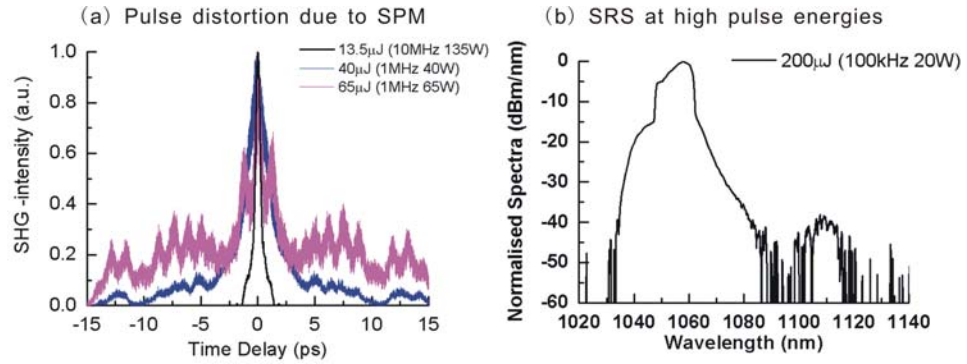

Figure 5.18: (a) Temporal and (b) spectral characteristics of the pulses at reduced repetition rates (increased pulse energies)

5.6 Conclusion

I have demonstrated an Yb-fiber chirped pulse amplification system incorporating a CFBG stretcher, bandwidth optimized amplifiers and a dielectric grating compressor. The system produces 135 W average power with a pulse energy of 13.5 μJ. The recompressed pulse duration is 360 fs. The high power pump coupling arrangement is optimized using numerical ray-tracing simulations to maximize the output power and avoid thermal damage to the amplifier fiber ends. This system demonstrates the operation of femtosecond fiber-based CPA systems, at high repetition rates, with high average powers, as well as high pulse energy without nonlinear distortions. At the time when it was developed, this system provided the highest combined average power and pulse energy when compared to either high average power systems with lower pulse energies [13], or high pulse energy systems with lower average powers [14].

References

[1] F. He, J. H. V. Price, A. Malinowski, A. Piper, M. Ibsen, and D. J. Richardson, "High Average Power, High Energy, Femto-second Fiber Chirped Pulse Amplification System," presented at Conference on Lasers and Electro-Optics, Baltimore, 2007, CMEE5.

[2] E. B. Treacy, "Optical Pulse Compression with Diffraction Gratings," *IEEE Journal of Quantum Electronics*, vol. QE-5, pp. 454, 1969.

[3] T. Erdogan, "Fiber Grating Spectra," *Journal of Lightwave Technology*, vol. 15, pp. 1277-1294, 1997.

[4] J. H. V. Price, "The Development of High Power, Pulsed Fiber Laser Systems and Their Applications," in *PhD Thesis, Optoelectronics Research Centre*: University of Southampton, 2003.

[5] G. P. Agrawal, *Nonlinear Fiber Optics*, 3rd ed. San Diego: Academic Press, 2001.

[6] E. Hecht, *Optics*, 3rd ed: Addison Wesley Publishing Company, 1997.

[7] Zemax, *Zemax User's Guide, May 3 2004*.

[8] C. Palmer, *DIFFRACTION GRATING HANDBOOK*, 6th ed: NEWPORT CORPORATION 2008.

[9] C. N. Danson, P. A. Brummitt, R. J. Clarke, J. L. Collier, B. Fell, A. J. Frackiewicz, S. Hancock, S. Hawkes, C. Hernandez-Gomez, P. Holligan, M. H. R. Hutchinson, W. J. L. A. Kidd, I. O. Musgrave, D. Neely, D. R. Neville, P. A. Norreys, D. A. Pepler, C. J. Reason, W. Shaikh, T.B.Winstone, R. W. W. Wyatt, and B.E.Wyborn, "Vulcan Petawatt -an ultra high intensity interaction facility," *Nuclear Fusion*, vol. 44, pp. S239-S246, 2004.

[10] M. D. Perry and G. Mourou, "Terawatt to Petawatt Subpicosecond Lasers " *Science*, vol. 264, pp. 917-924, 1994.

[11] M. D. Perry, D. Pennington, B. C. Stuart, G. Tietbohl, J. A. Britten, C. Brown, S. Herman, B. Golick, M. Kartz, J. Miller, H. T. Powell, M. Vergino, and V. Yanovsky, "Petawatt laser pulses," *Optics Letters*, vol. 24, pp. 160-162, 1999.

[12] D. N. Fittinghoff, B. Wattellier, and C. P. J. Barty, "Advanced Compressor Designs for High Energy Petawatt Pulse Generation," in *3rd International Conference on Inertial Fusion Science and Applications*. Monterey, 2003.

[13] J. Limpert, F. Roser, T. Schreiber, and A. Tunnermann, "High-power ultrafast fiber laser systems," *IEEE Journal of Selected Topics in Quantum Electronics*, vol. 12, pp. 233-244, 2006.

[14] A. Galvanauskas, "Mode-scalable fiber-based chirped pulse amplification systems," *IEEE Journal of Selected Topics in Quantum Electronics*, vol. 7, pp. 504-517, 2001.

Chapter 6 High pulse energy femtosecond fiber CPA system

This chapter presents the development of the high pulse energy CPA system for applications in X-ray generation. In this system, the output average power was maintained at a moderate level (1~10 W) and high pulse energies were achieved by reducing the seed pulse repetition rate from ~50 MHz to ~10 kHz. Note that several issues have already been addressed in previous Chapters. For example, the amplifier cascade design was described in Chapter 3, some general issues of fiber CPA systems were discussed in Chapter 4, and the possibility of operating the fiber CPA system at high repetition rates to achieve high average powers was demonstrated in Chapter 5.

The key challenge for developing this system was to avoid nonlinear distortions of pulses at high pulse energies. Therefore PCF has been used in this system due to its advantages, as discussed in Chapter 2 and 3. Other essential components in the system were the stretcher and the compressor. The system output pulse characteristics were investigated with a CFBG stretcher and a dielectric grating compressor, and then with a dielectric grating stretcher with a dielectric grating compressor. I am grateful to Dr. J. W. Dawson, B. Pyke, Dr. C. W. Siders, Dr. J. A. Britten, and Dr. C. P. J. Barty from LLNL for the design, for the grating supply, and for the assistance with the stretcher alignment. I also gratefully acknowledge the contributions from Dr. J. H. V. Price, S. Butler, T. McIntyre from the ORC for designing and machining the mechanical mounts.

This chapter is structured as follows. The system design is first described in section 6.1, and then the challenges arising from operating the system at such low repetition rates are described in section 6.2. In section 6.3, results of the system with a CFBG stretcher and dielectric grating compressor are presented. The results of the system with the dielectric grating stretcher and compressor are described in section 6.4, and finally section 6.5 presents the conclusions.

6.1 Experimental setup

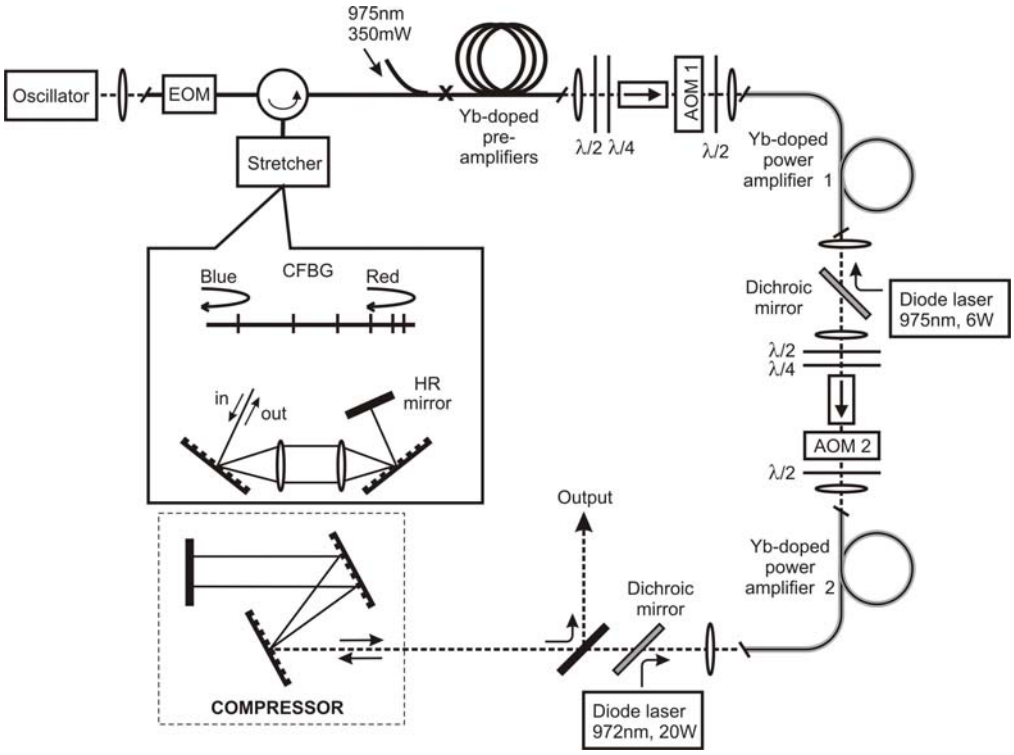

Figure 6.1: Detailed schematic of the high pulse energy CPA system

The detailed schematic of the high pulse energy CPA system is shown in Figure 6.1. The seed laser pulses (~ 100 fs, λ_0=1055 nm, $\Delta\lambda$ ~ 18 nm) from the mode-locked fiber laser presented in Chapter 4, were first passed through a EOM to reduce the repetition rate from 50 MHz to 100 kHz. The pulses were then stretched in duration using either a CFBG stretcher or a bulk grating stretcher. The stretched pulses were amplified in three stages of core-pumped Yb-fiber pre-amplifiers and two stages of cladding-pumped amplifiers. Yb-doped single-mode fiber was used in the first three stages of the pre-amplifiers, and the detailed parameters are presented in Chapter 3. The first cladding-pumped amplifier consisted of 3.5 m of LMA fiber (core diameter 20 μm, NA 0.06; inner cladding diameter 180 μm, NA 0.5), backward pumped by fiber pigtailed 975 nm laser diodes with 6 W power. The final cladding-pumped amplifiers comprised ~2 m of polarizing PCF (core diameter 40 μm, NA 0.03; inner cladding diameter 170 μm, NA 0.6), backward pumped by fiber pigtailed 972 nm diodes with 20 W power. AOMs have been used before each cladding-pumped amplifier to prevent ASE build-up and reduce the final repetition rate to as low as 10 kHz. Finally, a dielectric grating compressor has been used to recompress the pulses. As presented in Chapter 4, the 20 cm dielectric

grating loaned by LLNL was used in the early stage of this thesis research, and then it was replaced by the 35 cm dielectric grating in the final setup.

6.2 Challenges at low pulse repetition rates

6.2.1 Schematic of pulse selection system

The 50 MHz pulse repetition rate is reduced in order to achieve high output pulse energy. A low pulse repetition rate is useful to avoid the use of high power pumps, therefore the output average power of our system was maintained at ~10 W level with the use of a 20 W pump diode in the final amplifier in order to avoid the thermal effects associated with the high average output powers and the use of the large and cumbersome pump lasers. However, the minimum pulse repetition rate is constrained by the Yb ions' lifetime, which is in the millisecond scale. According to the two constraints described above, the system is designed to operate at ~10 kHz output pulse repetition rates.

To avoid the amplification of unnecessary pulses, it is desirable to reduce the repetition rate to ~10 kHz using the EOM. However, the average signal power is scaled down with the pulse repetition rate, which results in an extremely low input average signal power (e.g. ~0.2 μW at 100 kHz, and ~0.02 μW at 10 kHz) to the amplifier cascade. Such low input signal powers can lead to the generation of strong ASE, and its amplification in the following amplifiers. For example, Figure 6.2 shows the output pulse spectra of the pre-amplifiers when they are operating at 50 MHz and 100 kHz repetition rates. As shown in the figure, ASE at 1030 nm is generated at 100 kHz repetition rates. However, the spectral peak of the ASE is still maintained 10 dB below the spectral peak of the signal. When the pulse repetition rate is reduced further to 10 kHz, the spectral peak of the ASE can be equivalent to, or even higher than, the spectral peak of the signal.

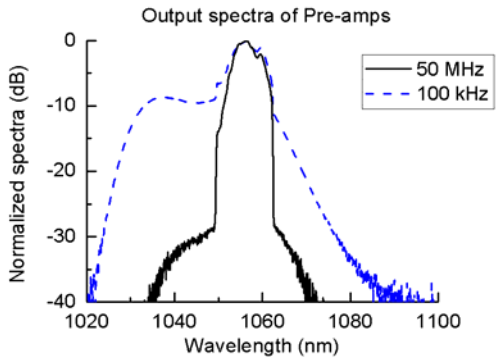

Figure 6.2: Output spectra of the pre-amplifiers with pulses at different repetition rates

The ASE generated in the pre-amplifiers can reach a high gain if it is input into the next amplification stage together with the signal. As the ASE and signal pulse can be separated by using amplitude modulation in the time domain, an AOM was inserted before each power amplifier stage to reduce the ASE. The detailed pulse gating method is discussed in Chapter 4. The AOMs can also be used to reduce the pulse repetition rates.

I experimentally measured the output spectra of the amplifier cascade with different combinations of the pulse gating rates at the EOM and the AOMs. The system schematic is similar to Figure 6.1, except that 5 m of LMA fiber (core diameter 20 μm, NA 0.06; inner cladding diameter 180 μm, NA 0.5) was used in the final amplifier. CFBG2 is used as the pulse stretcher. The final LMA amplifier is operated at 10 kHz pulse repetition rates, and an output power of approximately 1 W. As described above, the gating rate of the EOM has a substantial effect on the ASE generated in the amplifier cascade. A high (>100 kHz) EOM gating rate means more pulses will be rejected by the AOMs in order to reach the final pulse repetition rate of 10 kHz. This leads to a low input signal power to the power amplifiers, which results in the generation of strong ASE in the power amplifiers. To reduce the ASE that is generated in both the pre-amplifiers and the first power amplifier, and the pulse repetition rate is reduced to 100 kHz by the EOM and to as low as 10 kHz by the AOM prior to the final amplifier, although a repetition rate of 16.67 kHz was used for the experiment presented here. Table 6.1 provides an example of the pulse gating design for the system using dielectric gratings as the pulse stretcher and compressor, and PCF in the final amplifiers.

Table 6.1: Pulse repetition rates used in the CPA system

Components	**Repetition rate**	**Gain (dB)**	**Loss (dB)**	**Energy**	**Power**
Oscillator	50 MHz			60 pJ	3 mW
EOM	100 kHz		8		
Stretcher (bulk grating)			7		
Pre-amplifiers		60	7	0.4 μJ	40 mW
AOM1	33.33 kHz		2		
Power amplifier 1		19	3	9 μJ	300 mW
AOM2	16.67 kHz		2		
Power amplifier 2		19	3	200 μJ	3.33 W

6.2.2 ASE suppression at the PCF amplifier input

At the output of the first power amplifier in the system, the spectral peak of the ASE can be maintained 20 dB below the spectral peak of the signal with the pulse gating scheme in Table 6.1. However, the PCF that is used in the final amplifier provides high gain to the ASE at ~1030 nm. Figure 6.3 shows an example of the input and output spectra of the final PCF amplifier. The mode-locked glass oscillator (described in detail in Chapter 4) is used in this experimental investigation, but its output pulse energy is tuned down to be the same as the mode-locked fiber oscillator to be suitable for its future replacement. The pulse repetition rate has been tuned down to 16.67 kHz at the system output. The output of the PCF amplifier has 1.67 W output average power.

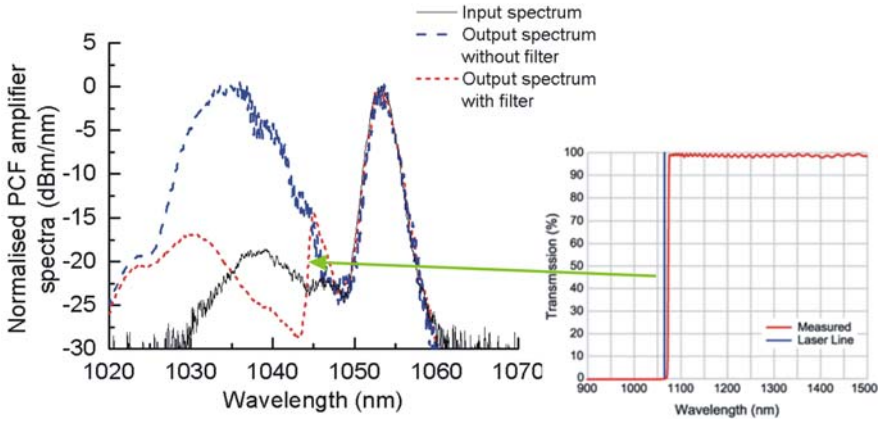

Figure 6.3: Output spectra of the PCF amplifier with and without an edge pass filter (inset: the transmission spectrum of the Semrock edge filter)

The PCF's high core/cladding overlap ratio has enabled the use of a short device length to minimize the nonlinear effects. However, it also results in high inversion in the amplifier, which leads to high gain at 1030 nm. As a consequence, a strong ASE peak at 1030 nm can be observed experimentally at the amplifier output even with a relatively low level of ASE at the amplifier input, as shown in Figure 6.3. In order to minimize the system ASE, a long wavelength edge-pass filter has been used to further reduce the input ASE to the PCF amplifier. The transmission spectrum of the filter, from Semrock Inc., is shown in the inset of Figure 6.3. The cut-off wavelength of the filter can be adjusted in the 1064~1030 nm range by changing the incident angle of the input beam from 0-30°. By comparing the output spectra, with and without the filter, it can be seen from Figure 6.3 that the ASE at the amplifier output can be significantly reduced by using the filter before the amplifier.

6.3 Experimental results of system with CFBG stretcher and dielectric grating compressor

6.3.1 CFBG stretcher and 20 cm dielectric grating compressor

The first experimental approach for the high pulse energy CPA system followed the schematic in Figure 6.1. This high pulse energy system used the CFBG2 stretcher and the 20 cm dielectric grating compressor, in the same setup as described in Chapter 5.

Figure 6.4 shows the output spectra of the final amplifier and the autocorrelation traces of the recompressed pulses when the system is operating at 50 kHz. The autocorrelator that is used in the measurements is an APE PulseCheck. The EOM is used to gate down the seed pulses from 50 MHz to 100 kHz, and the two AOMs are used to gate down the pulse repetition rates further to 50 kHz. A ~2 m length of polarizing PCF was used in the final amplifier. The edge filter, that was presented in section 6.2, is not installed in this setup. The output average power of the final amplifier can be as high as 5 W by increasing the pump power. As discussed in Chapter 5, spectral clipping was observed in the compressor, resulting in the overall transmission efficiency of 52%.

Figure 6.4 (a), (c), and (e) show the autocorrelation traces of the recompressed pulses when the output average power of the final amplifier is 1 W, 3 W, and 5 W, corresponding to 20 μJ, 60 μJ, and 100 μJ pulse energies respectively. The FWHMs of the autocorrelation traces were 650 fs at energies up to 100 μJ, corresponding to a pulse width of 460 fs assuming that the pulses have a Gaussian shape. However, pulse pedestals have increased with the increase of the pulse energies, which is believed to be due to the nonlinear effects. The estimated B-integrals at 20, 60, and 100 μJ pulse energy are 0.3 π, 0.9 π, and 1.5 π, respectively.

The output spectra of the final amplifier, with the increase of the pump power, are shown in Figure 6.4 (b), (d), and (f). Spectral ripples were observed on the high energy spectra. The modulation depth of the ripples was minimized by adjusting the half-wave plate at the input to the final PCF amplifier, but it was not possible to eliminate these features. Measurements showed that 90% of the output power from that amplifier was along one polarization axis. The depth of the spectral modulations increased with increased output pulse energy, so it is believed that the modulation is due to a combination of polarization and nonlinear interactions in the final amplifier fiber [1]. The saturation energy of the amplifier is calculated to be 300 μJ, and no gain saturation has been observed at pulse energies up to 100 μJ. ASE peaked around 1040 nm has increased with the increase of the pump power, as shown in Figure 6.4 (b), (d), and (f). Spectral

clipping was observed at the compressor due to the size of the 20 cm dielectric grating, similar to the results presented in Chapter 5. According to the data shown in Figure 5.17, the predicted minimal pulse duration, obtained by using the FFT of the compressor output spectra with flat phase, is approximately 360 fs (compared to the experimentally achieved 460 fs pulse duration in Figure 6.4). A combination of gain shaping due to the high inversion levels in the PCF amplifier, and dispersion mismatch between the stretcher and compressor, has resulted in somewhat longer pulses than were shown by the results in Chapter 5.

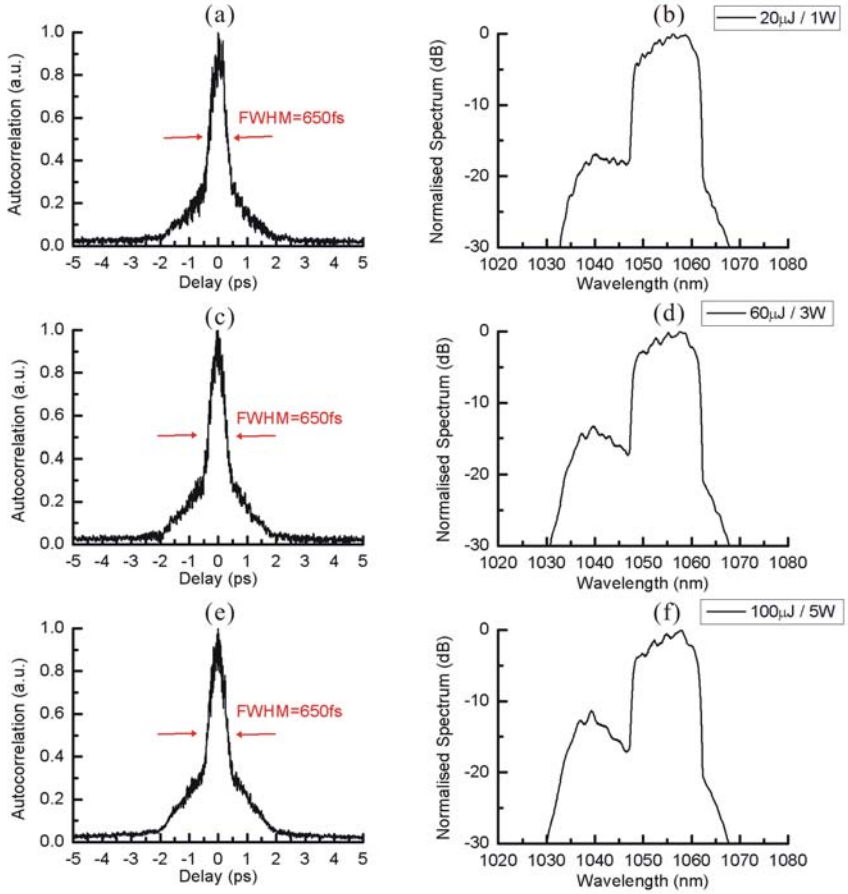

Figure 6.4: Output pulse and spectra of system with the CFBG2 based stretcher and the 20 cm dielectric grating based compressor, operating at a 50 kHz repetition rate. The FWHM of the autocorrelation traces are illustrated in (a), (c) and (e). The average power and the corresponding pulse energy of the final amplifier (before compression) are showed in (b), (d) and (f).

Pulses with higher pulse energy have been measured by tuning the pulse repetition rate further down to 10 kHz at the two AOMs. Figure 6.5 shows the output spectra of the final amplifier at 0.02 W, 1.7 W, and 4.9 W average powers, and the corresponding autocorrelation traces of the recompressed pulses. Note that the pulse at 490 μJ energy

was significantly distorted which makes it very difficult to measure, therefore it is not illustrated in the figure.

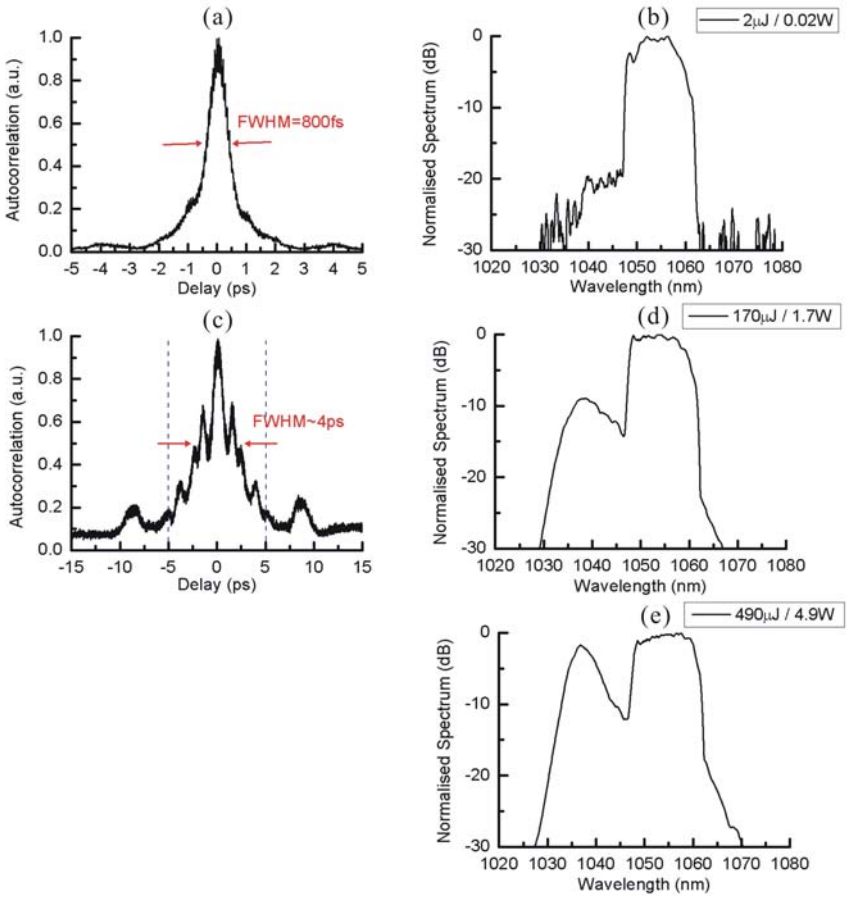

Figure 6.5: Output pulse and spectra of system with the CFBG2 based stretcher and the 20 cm dielectric grating based compressor, operating at 10 kHz repetition rate. The FWHM of the autocorrelation traces are illustrated in (a) and (c). The average power and the corresponding pulse energy (including ASE) of the final amplifier (before compression) are showed in (b), (d) and (e).

As shown in Figure 6.5 (a), high quality pulses with an autocorrelation FWHM of 800 fs (corresponding to 560 fs for Gaussian pulses) can be achieved at a low pulse energy (2 μJ) when the system is operating at 10 kHz. At the same time, the signal is approximately 20 dB above the ASE in the spectrum, as shown in Figure 6.5 (b). Figure 6.5 (c) shows the distorted pulses, at energies of 170 μJ, due to the fiber nonlinear effects when the B-integral is above 2.5 π. ASE also became significant at this output power level, as shown in Figure 6.5 (d). Further increase of the pump power led to a maximum output average power of 4.9 W, and at that power level, the spectral peak of the ASE became equivalent to the spectral peak of the signal, as shown in Figure 6.5 (e).

Integration of the spectral power indicated that the signal and the ASE in the spectrum represent 72% and 28% of the total power respectively.

6.3.2 CFBG stretcher and 35 cm dielectric grating compressor

In the Treacy compressor configuration, the maximum pulse compression ratio in the time domain is proportional to the size of the spatially expanded beam, which is ultimately limited by the width of the dielectric grating. For example, when the grating is smaller than the spatially expanded beam, spectral clipping will take place, and result in loss of power. If the grating is larger than the spatially expanded beam, the horizontal roof mirror can be moved further away from the grating to create more chirp on the pulses. Therefore, in the following experiments, the 20 cm grating was replaced by a 35 cm dielectric grating in this compressor. The compressor setup used the Treacy configuration that was described in Chapter 5. The grating has dimensions of 35x10 cm. The groove density is 1739.5 grooves/mm, (which corresponds to a Littrow angle of 66.45 degrees for a 1054.0 nm input beam). The designed incident angle is 73.5 degrees in our compressor setup, which gives a diffracted angle of 61.0 degrees for an input signal at 1054 nm. The effective grating separation is 230.0 cm, which corresponds to dispersion ($D \times Length$) and the 3rd order dispersion ($dD/d\lambda \times Length$) of 208.16 ps/nm and 4.24 ps/nm^2 respectively.

Both the 20 cm and 35 cm gratings provide diffraction efficiency as high as 95% for a single pass. Compared with the 20cm grating, the 35 cm grating covers the entire input spectrum, and thus results in an overall transmission efficiency as high as 65%. Figure 6.6 compares the output spectra of the two gratings, and the input spectrum is also shown for reference. The spectra are measured at low pulse energy (~20 nJ) and high pulse repetition rates (~50 MHz), hence the ASE is low in the input spectrum. Note that the overall transmission efficiency of the 35 cm grating compressor was measured to be as high as 75% for a linearly polarized (polarization extinction ratio >20 dB), narrow linewidth (<0.01 nm) CW signal (tunable laser from Sacher Lasertecknik Group) at 1055 nm. The amount (<10%) of the amplifier output signal on the wrong polarization axis and the residual ASE from the amplifier output that is outside the compressor transmission window have reduced the effective compressor transmission efficiency by approximately 10%.

Two CFBGs, that were designed to match the dispersion of the 35 cm grating compressor, and were fabricated at the ORC. Table 6.2 summarizes the measured dispersion values of the two CFBGs, labeled as CFBG21 and CFBG22. Table 6.2 also

lists the measured dispersion values of another four CFBGs, labeled from CFBG11 to CFBG14, that were designed to be connected as pairs in series to provide the same dispersion as CFBG21 and CFBG22. The values that are listed in Table 6.2 were measured using the methods as described in Chapter 5.

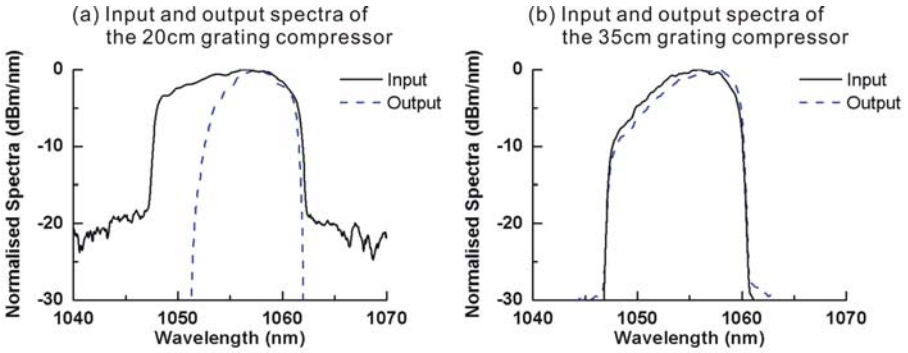

Figure 6.6: Input and output spectra of the grating compressor with gratings of different widths

Table 6.2: CFBGs designed for 35 cm grating compressor

Label	**Dispersion (ps/nm)**	**3rd order dispersion (ps/nm^2)**	**Ratio between dispersion and 3rd order dispersion values**	**Operating spectral window (nm)**
Design	-208.16	-4.24	49.09	
CFBG21	-210.74	-6.73	31.31	1047.1-1060.1
CFBG22	-210.89	-5.14	41.03	1047.1-1060.1
Design2	-104.08	-2.12	49.09	
CFBG11	-107.35	-2.80	38.34	1046.0-1062.1
CFBG12	-105.69	-2.98	35.47	1047.2-1062.2
CFBG13	-107.22	-2.13	50.43	1045.8-1062.3
CFBG14	-106.99	-2.12	50.46	1045.8-1062.0

As discussed in Chapter 5, the dispersion ($D \times Length$) and the 3rd order dispersion ($dD/d\lambda \times Length$) of the compressor can be tuned slightly by moving the horizontal roof mirror, but the ratio between them determines whether they can be simultaneously matched to the dispersion values of the stretcher. Therefore, it can be estimated from Table 6.2 that CFBG21 will have higher residual 3rd order dispersion than CFBG22 when the grating compressor is tuned to minimize the system chromatic dispersion. Moreover,

Table 6.2 can be used to select two CFBGs to be used in series. For example, when the compressor separation was adjusted to match dispersion ($D \times Length$), the use of CFBG13 and CFBG14 as stretcher would have residual 3rd order dispersion ($dD/d\lambda \times Length$) of ~0.1 ps/nm^2, and the use of CFBG11 and CFBG12 would have residual 3rd order dispersion ($dD/d\lambda \times Length$) of ~-1.4 ps/nm^2.

Figure 6.7 (left column of graphs) summarizes the reflection spectra and dispersion characteristics of the CFBGs. Figure 6.7 (right column of graphs) shows the system output autocorrelation traces with four different CFBG stretchers. The experiments were performed with the 35 cm dielectric grating compressor when the CPA system was operating at ~1 W average power, with ~50 MHz repetition rates (corresponding to 0.02 μJ pulse energy), to avoid nonlinear distortions from the amplifiers. The compressor grating separation was adjusted to give the highest peak in the autocorrelation trace for each CFBG stretcher.

For comparison, Figure 6.7 (right column of graphs) also shows the calculated autocorrelation traces by using the FFT of the compressor output spectra with flat phase. The increase of pulse pedestal and duration may originate from the system's residual dispersion. According to the dispersion data, shown in Table 6.2, the use of CFBG21 as stretcher would generate residual 3rd order dispersion ($dD/d\lambda \times Length$) of ~ -2.3 ps/nm^2, when the compressor separation was adjusted to match the dispersion ($D \times Length$). Therefore, it was not surprising to see that large pulse pedestals are associated with CFBG21. As a comparison, the use of CFBG22 corresponds to a lower residual 3rd order dispersion ($dD/d\lambda \times Length$) of ~ -0.8 ps/nm^2.

The figure shows that the experimentally measured pulses generally have a higher pulse pedestal and duration than the calculated data. The recompressed pulse autocorrelation trace, using the CFBG22 stretcher, has approximately 900 fs FWHM duration, corresponding to 640 fs FWHM duration for Gaussian pulses. However, the calculated autocorrelation trace from the FFT of the spectra with flat phase has 370 fs FWHM duration, corresponding to 260 fs FWHM duration for Gaussian pulses. The pulses after the CFBG22 stretcher have been measured to be approximately 2.0 ns (FWHM), by using the same method as described in Chapter 5. Note that by tuning the pulse repetition rate down to 100 kHz, the output pulses were measured at higher pulse energies with the system using the CFBG22 stretcher and the 35 cm grating compressor. It was also found that the output pulse autocorrelation shapes were maintained from the low energy of 20 nJ (as shown in Figure 6.7) to a high energy of 20 μJ.

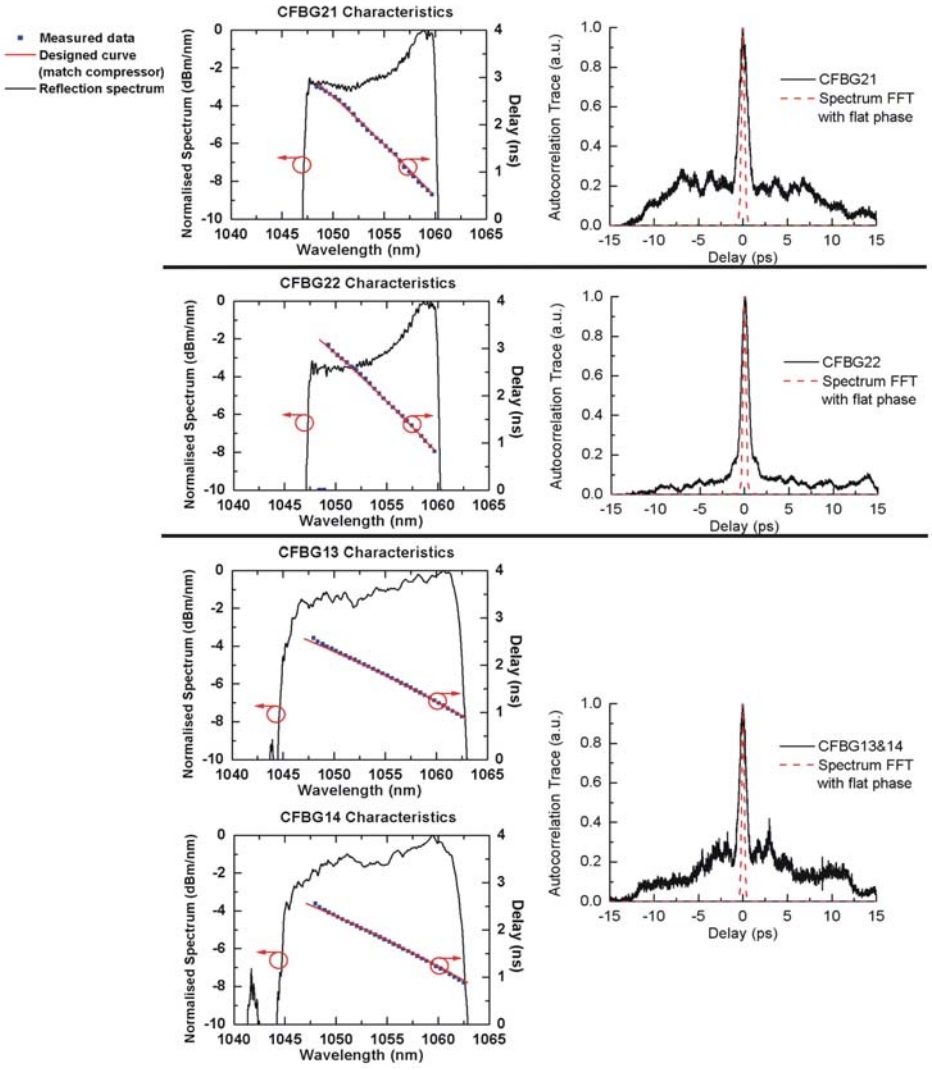

Figure 6.7: Experimentally measured CFBG characteristics (left column) and autocorrelation traces of the recompressed pulses (right column).

The use of two CFBGs connected in series as the stretcher has also been investigated. The benefit of using CFBGs in series is the creation of a broader spectral window. With the four CFBGs, that are designed to be used in pairs, the combination of the CFBGs to provide a close match to the dispersion/3rd order dispersion ratio of the compressor can be chosen. Figure 6.7 shows an example of the results using the combination of CFBG13 and CFBG14 as a stretcher. The pulse quality is not as good as expected because there are two difficulties associated with the use of CFBGs in series. The first one is the difficulty in the control of the input polarization to the two CFBGs, which results in the degradation of the pulse quality. The second difficulty is the additional loss associated with the use of two CFBGs, which results in the increase of the ASE at the system output. Therefore, this stretcher option is not used in the following experiments.

As described in this section, the output pulses are characterized with different CFBG stretchers and the 35 cm grating compressor. However, in general, the measured output pulse duration is more than 2 times higher than the theoretical prediction, and the measured output pulses have more pedestal than expected. The differences could have originated from the mismatched dispersion, polarization and the spectral characteristics of the CFBGs. It is planned that our group will acquire FROG (frequency-resolved optical gating) data of the output pulse to check this in the future. Therefore, in order to achieve the high quality pulses that are required for applications such as X-ray generation, a dielectric grating stretcher was applied in the following experiments which had matched dispersion to the 35 cm dielectric grating compressor. The details will be described in the following section.

6.4 Experimental results of system with dielectric grating stretcher and compressor

Bulk grating stretchers and compressors are widely used in conventional glass or crystal laser systems using the CPA technique to achieve high peak power femtosecond pulses [2, 3]. A typical pulse stretcher consists of a pair of antiparallel diffraction gratings separated by a one-to-one magnification refractive telescope, and the pulse compressor generally consists of a pair of parallel diffraction gratings. Provided that the stretcher grating has the same groove density and input angle as the compressor grating, the stretcher produces dispersion equal and opposite to that of the compressor, to all orders, when the telescope of the stretcher is modeled paraxially and the lens material dispersion is neglected.

The conventional 'Martinez' stretcher configuration described above does not permit compensation of the material dispersion, and can produce a spatially non-uniform output chirp if any component is not aligned with high precision. In order to minimize the spherical and chromatic aberration, and to allow compensation of the material dispersion of the fiber amplifiers, a stretcher configuration designed by LLNL was used. The design minimizes spatial inhomogeneities and up to 5^{th} order phase errors by using a dispersive ray-tracing analysis that includes the effects of finite beam diameter and beam divergence [4]. The stretcher design is shown schematically in Figure 6.8. The setup consists of a pair of cylindrical mirrors (M4, M5), which have a radius of curvature of ~1915 mm (and are used at an incident angle of 10 degrees). Two fold mirrors (M1, M3) have been placed between the two cylindrical mirrors. The use of cylindrical, rather than

spherical, mirrors eliminates the introduction of additional beam divergence in the vertical dimension, thus allowing the system to be easily multi-passed through vertical beam displacement. The beam has two round trips in our stretcher design. In each round trip, a pair of vertical roof mirrors (M7 & M8 for the first round trip, M11 & M12 for the second round trip) is used to change the height of the horizontal plane of the return beam. After the first round trip, a stair case, which consists of 4 mirrors (M2, M6, M9, and M10), is used to change the height of the beam and simultaneously to invert the image of the beam in the plane of diffraction. This technique minimizes the spatial errors because the aberration accumulated during the first round trip is reversed on the second round trip.

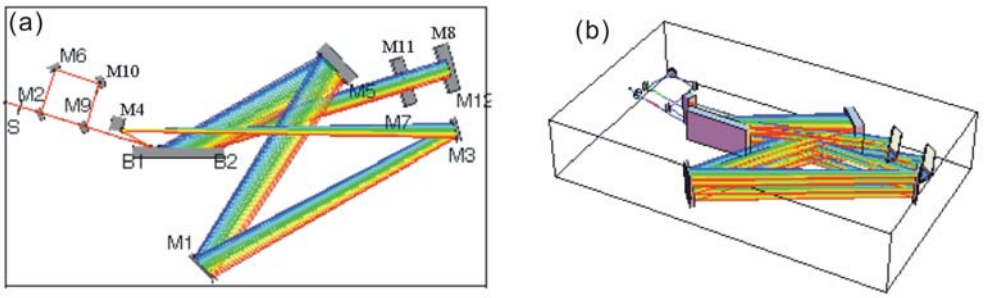

Figure 6.8: Schematic of dielectric grating stretcher. (a) top view, (b) 3-D view. The false-colour ray paths use green to represent the central wavelength of the input signal (~1055 nm), and blue or red to represent the shorter or longer wavelengths.

As the compensation of dispersion, to all orders, can never be achieved independent of wavelength [4], ray-tracing calculations were used to cancel the first few orders of dispersion at the central wavelength. Given a stretcher of the above design and a compressor with identical grating groove density (the detailed compressor setup is described in Chapter 5), the first few orders of dispersion terms can be minimized by correctly choosing the separation and the incident angle of the gratings. Table 6.3 shows the calculated dispersion terms when the optical axis is chosen for a central wavelength of 1055.335 nm.

Figure 6.9 shows the calculated residual delay as a function of wavelength. The calculation includes the dispersion from the stretcher, the compressor, and the fibers in the amplifiers. The figure shows that this system has minimal residual delay when the signal wavelength is in the range from 1054 nm to 1058 nm, and the total residual delay error across the 12 nm spectral window of the stretcher and the compressor is less than 100 fs.

Table 6.3: Dispersion calculation results for the stretcher and compressor

Parameter	Stretcher	Compressor
Groove density	1739.485 groove/mm	1739.485 groove/mm
Spectral window	12 nm	12 nm
Incident angle	61.49 degree	73.50 degree
Dispersion ($\beta_2 z$)	1.57741 x 10^8 fs^2	-1.57957 x 10^8 fs^2
3rd order dispersion ($\beta_3 z$)	-2.1248 x 10^9 fs^3	2.12468 x 10^9 fs^3
4th order dispersion ($\beta_4 z$)	4.72238 x 10^{10} fs^4	-4.75797 x 10^{10} fs^4
5th order dispersion ($\beta_5 z$)	-1.52525 x 10^{12} fs^5	1.49145 x 10^{12} fs^5

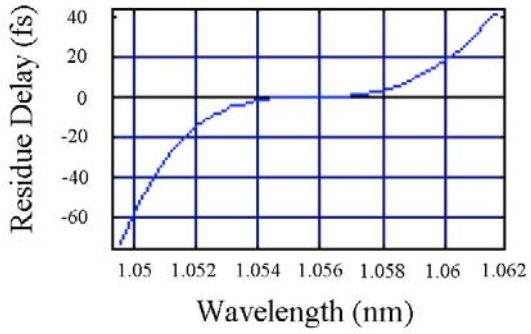

Figure 6.9: Calculated system residual delay as a function of wavelength

The stretcher alignment procedure is described in Appendix II. The overall stretcher efficiency was measured to be 36% (free space). The stretcher was then incorporated into our CPA system as shown in Figure 6.1. The EOM output fiber end was connected to the stretcher as the input. After the free-space propagation in the stretcher, the output beam was re-launched into single-mode fiber for connection with the fiber amplifier, and the maximum fiber coupling efficiency was measured to be ~48%. Figure 6.10 (a) shows the measured pulse temporal shape after the fiber launch. This was measured using a 10 GHz photodiode as described in Chapter 5. Figure 6.10 (b) and (c) show the measured stretcher input and output spectra on dB and on linear scales, respectively.

Figure 6.10 shows that the dielectric grating stretcher provides ~12 nm spectral window, compared to the ~13 nm spectral window of the CFBG stretchers. Therefore, assuming that the rest of the system remains unchanged, the fiber nonlinear thresholds of the system with the two types of stretchers are estimated to be similar. However, compared with the CFBG stretchers, the transmission spectrum of the dielectric grating stretcher has fewer spectral modulations, the input polarization can be more precisely

controlled by using wave-plates in free-space, and the design of the dielectric grating stretcher allows us to accurately compensate for the system dispersion up to the 5th order. Therefore, compared with the experimental results achieved by using the CFBG stretcher, that are shown in Figure 6.8, recompressed pulses with a shorter duration and lower pedestals are expected to be achieved by using the dielectric grating stretcher. The experimental results are shown in the following paragraphs.

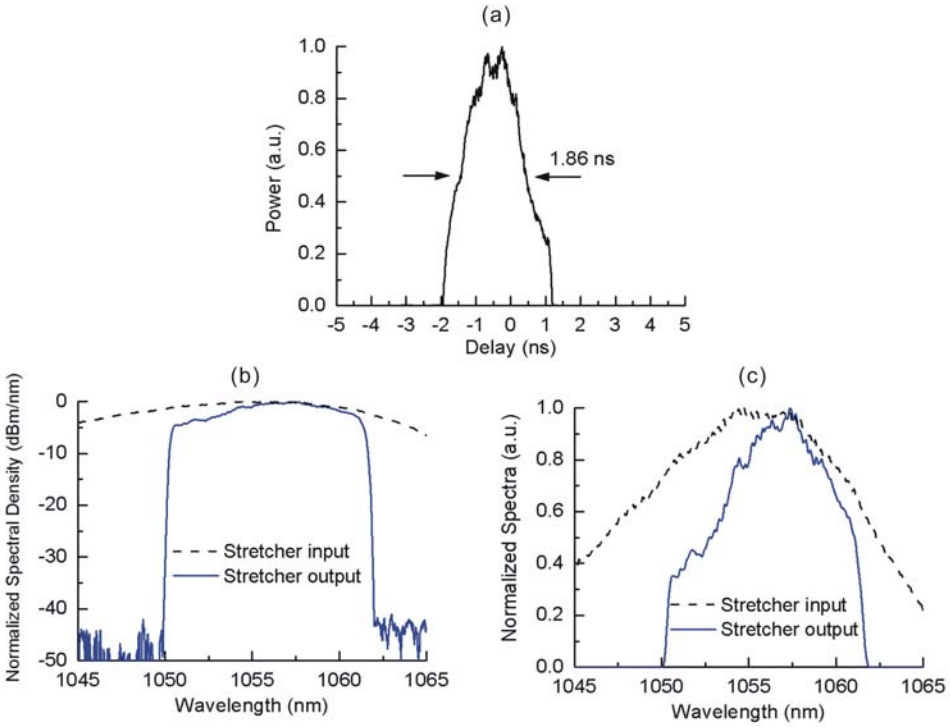

Figure 6.10: Dielectric grating stretcher output pulse shape and spectra

To test the fidelity of the dielectric grating stretcher and compressor, the output pulses were first characterized at low pulse energies, when the nonlinear effects of the fiber amplifiers could be neglected. The system schematic is shown in Figure 6.1. The recompressed pulse spectra and autocorrelations are measured when the system has ~1 W average output power at ~50 MHz repetition rates, corresponding to 0.02 μJ pulse energy. The grating separation in the compressor was adjusted to give the highest peak in the autocorrelation trace.

The dielectric grating compressor was initially aligned with the incident angle of 73.5 degrees, according to the design shown in Table 6.3. However, the measured system output autocorrelation trace showed a pedestal at the designed incident angle. That could have originated from the 3rd (and/or higher) order dispersions of the amplifier fibers and the accuracy of the stretcher alignment, both of which are difficult to estimate without complete characterization of the pulse using a FROG measurement, for example.

Therefore, in order to achieve high quality pulses, I adjusted the compressor incident angle over a relatively small range to compensate the dispersion errors from the system. The left and middle column of the graphs in Figure 6.11 show the measured autocorrelation traces at different compressor incident angles on linear and dB scales, respectively. The right column of graphs in Figure 6.11 shows the compressor input and output spectra. Care was taken to make sure that no spectral clipping had been introduced to the output spectrum during the change of the incident angles. The calculated autocorrelation traces, based on the FFT of the compressor output spectrum with flat phase, are also shown in the left and middle column of the graphs for comparison with experimental results.

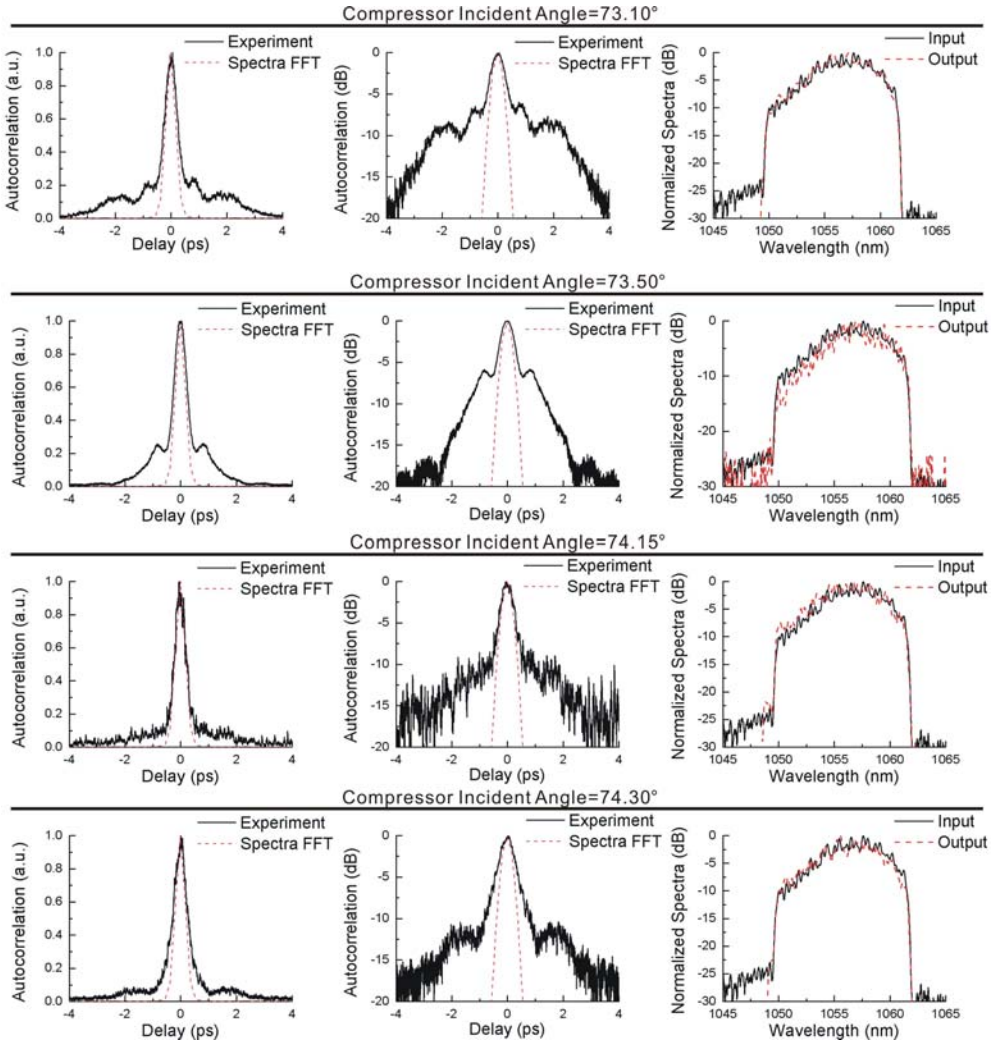

Figure 6.11: Autocorrelation traces in linear scale (left column of graphs), autocorrelation traces in dB scale (middle column of graphs), and output spectra (right column of graphs) of CPA system with different compressor incident angles at low pulse energies.

From Figure 6.11, it can be seen that by adjusting the compressor incident angles in the range of 72.6-74.3 degrees in steps of 0.15-0.20 degrees, it was found that an input angle of 74.15 degrees provided the optimum output pulse quality. After the optimization of the compressor incident angle, the pulse autocorrelation FWHM is measured to be ~500 fs, corresponding to a pulse FWHM of ~350 fs assuming a Gaussian shape (time-bandwidth product $\Delta\nu\Delta\tau$ ~0.6). The experimental result is in close agreement with the calculated autocorrelation FWHM of ~450 fs from the spectrum FFT with flat phase. The pulse quality that has been demonstrated at low pulse energies is expected to be maintained with increased pulse energies until nonlinear effects become significant.

In order to achieve high pulse energies, a pulse gating scheme (as described in Table 6.1) was used to reduce the pulse repetition rate to 16.67 kHz. Figure 6.12 shows the autocorrelation traces and the output spectra of the recompressed pulses with the increase of the pump power in the final PCF amplifier. Figure 6.12 (a), (c), (e), and (g) show the autocorrelation traces of the recompressed pulses when the output average power of the final amplifier is 0.85 W, 1.67 W, 2.51 W, and 3.33 W, corresponding to 50 μJ, 100 μJ, 150 μJ, and 200 μJ pulse energy (before compression) respectively. The overall transmission efficiency of the grating compressor is ~65% for all the powers. The grating separation is adjusted slightly for maximizing the autocorrelation peak in the measurements. The autocorrelation FWHM of the recompressed pulses at 32.5 μJ pulse energy (50 μJ before compression) is measured to be ~1100 fs, corresponding to a pulse width of 780 fs assuming the pulses have a Gaussian shape (time-bandwidth product $\Delta\nu\Delta\tau$ ~0.6). However, pulse duration and pulse pedestals have increased with the increase of the pulse energies. The autocorrelation FWHM of the recompressed pulses at 130 μJ pulse energy (200 μJ before compression) is measured to be ~1600 fs, corresponding to a pulse width of 1130 fs assuming the pulses have a Gaussian shape (time-bandwidth product $\Delta\nu\Delta\tau$ ~0.8). Note that the measurement of the autocorrelation traces at low pulse repetition rates requires an average of several pulses, and therefore the fluctuations between pulses could broaden the measured autocorrelation traces.

The input and output spectra of the compressor with increase in the pump power are shown in Figure 6.12 (b), (d), (f) and (h). As discussed in Section 6.3.1, spectral ripples on the high energy spectra were minimized by adjusting the half-wave plate at the input to the final PCF amplifier, although it was not possible to eliminate these features. The inset of Figure 6.12 (h) shows that the spectral peak of the ASE is maintained ~20 dB lower than the spectral peak of the signal in the final PCF amplifier. There is no gain saturation nor has SRS been observed in the spectrum at pulse energies up to 200 μJ (before compression).

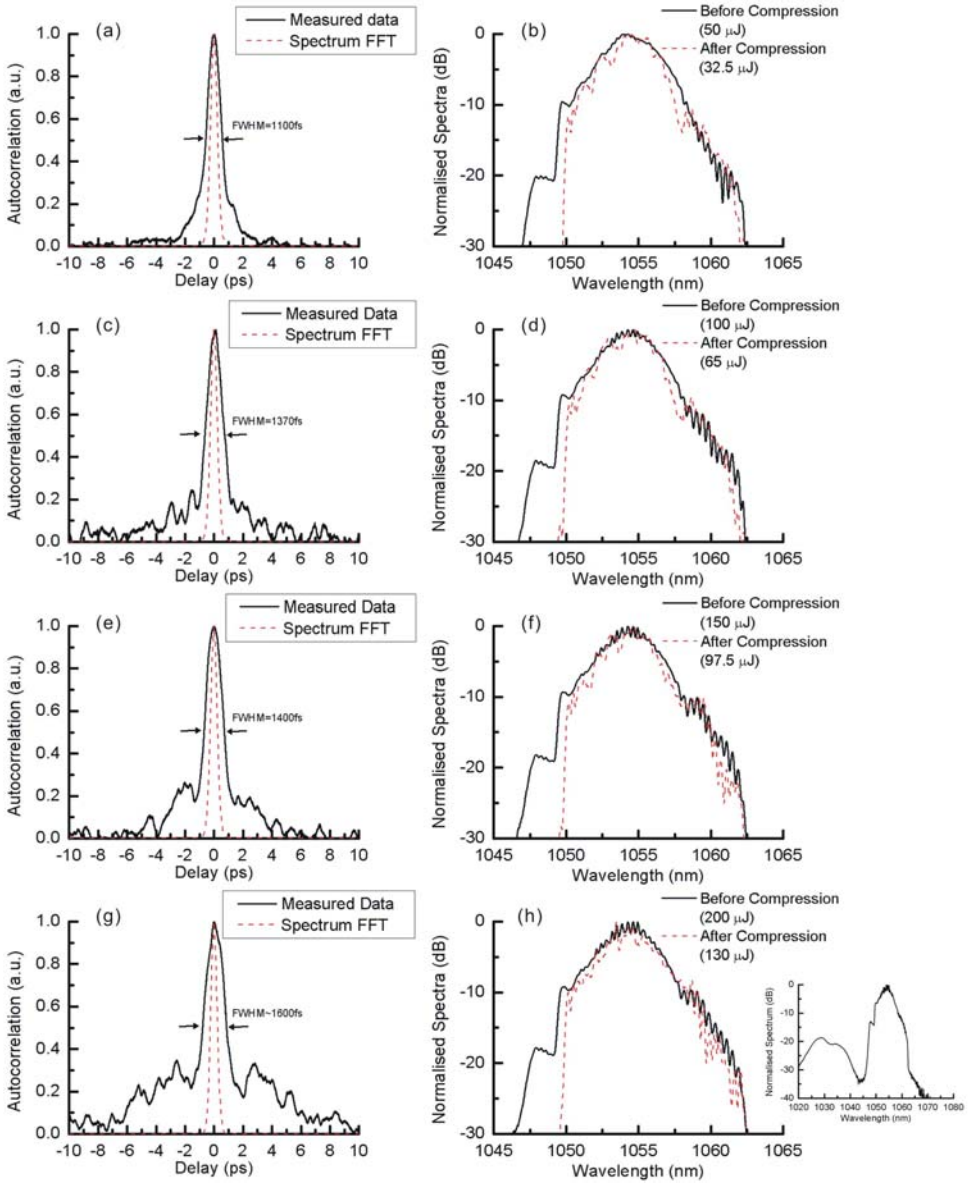

Figure 6.12: Experimentally measured autocorrelation traces of the recompressed pulses (left column) and spectra at the input and output of the compressor (right column).

This CPA system is operating with the existence of SPM to achieve high pulse energies; therefore a certain level of pulse degradation is expected. The estimated B-integrals are 1.1 π, 1.7 π, 2.3 π, and 2.9 π at 50, 100, 150 and 200 μJ pulse energies (before compression), respectively. As there is no significant difference between the spectra of the recompressed pulses with pulse energies up to 130 μJ, the calculated autocorrelation traces from the FFT of the spectra with flat phase have a similar FWHM of ~500 fs, which is ~10% higher than that of pulses with low energies (0.02 μJ). The slight differences in the calculated autocorrelation FWHM between high (>50 μJ, Figure

6.12) and low (0.02 μJ, Figure 6.11) pulse energies is due to the change of gain in each amplifier, especially in the final PCF amplifier.

The experimentally measured autocorrelation traces have an increased FWHM duration (e.g. 1100 fs at 32.5 μJ; 1600 fs at 130 μJ) compared with the calculated traces from spectral FFT (~500 fs). This discrepancy could result from the nonlinear phase shift introduced by SPM which can not be compensated in this system, as well as the averaging error in the autocorrelation trace measurement at low pulse repetition rates due to the energy fluctuations between pulses. Moreover, I also observed the fluctuations of the autocorrelation trace with air flows, which could introduce additional errors to the measured pulse durations, especially at low pulse repetition rates. To reduce the effects from the air flows, I have installed enclosures for the CPA system, and measured re-compressed pulses with 65 μJ energy (100 μJ before compression) and autocorrelation FWHM of ~700 fs (corresponding to a pulse width of ~500 fs assuming the pulses have a Gaussian shape) from the system. The CPA system is then prepared and used for X-ray generation experiments due to the tight timeline of the project, therefore I did not manage to systematically re-characterize the system. Our group is currently working on FROG measurements, and then optimizing the compressor (or stretcher) based on the analysis of the FROG data of the pulses at high pulse energies. In the future, a 70 μm core diameter rod-type PCF (commercially available) amplifier could be used to replace (or added after) the current 40 μm core diameter polarizing PCF amplifier to improve the pulse quality by reducing the SPM, and to further scale the pulse energy. This future work is beyond the content of this thesis.

6.5 Conclusion

This Chapter described the work towards the development of high pulse energy fiber CPA systems. CPA systems with different stretcher and compressor combinations were developed and investigated, including the 20 cm dielectric grating compressor with the CFBG stretcher, the 35 cm grating compressor with the CFBG stretchers, and the 35 cm grating compressor with the dielectric grating stretcher.

Among the three combinations, the system using the 35 cm dielectric grating compressor with the dielectric grating stretcher provided the highest recompressed pulse energy of 130 μJ. We obtained recompressed pulse durations as low as ~350 fs at low pulse energies (~20 nJ before compression), in close agreement with the pulses calculated from the FFT of the compressor output spectrum with flat phase. However, the

recompressed pulse duration increased to 1130 fs with an increase of pulse energy to 130 μJ, which corresponds to a pulse peak power of ~110 MW. Although a certain level of pulse degradation is expected due to the existence of SPM, further improvement of the pulse quality is believed to be possible by optimizing the stretcher and compressor alignment.

The system using the 20 cm dielectric grating compressor with the CFBG stretcher provided lower recompressed pulse energies of 52 μJ. The pulses can be recompressed to as low as ~460 fs at pulse energies of 52 μJ, which corresponds to a pulse peak power of ~110 MW, similar to the pulse peak power that was achieved in the system using the 35 cm dielectric grating compressor with the dielectric grating stretcher. However, based on the characteristics of the 20 cm dielectric grating compressor and the fact that the achieved pulse quality is close to optimum, further improvement of the pulse energy and the pulse quality in this system is not feasible without changing some of the key components.

The system using the 35 cm dielectric grating compressor with the CFBG stretcher has relatively longer recompressed pulse durations (>600 fs) at low pulse energies (~20 nJ before compression). Pedestals of the recompressed pulses were observed at low pulse energies, which remain constant with further increase of energy to up to 20 μJ.

References

[1] D. N. Schimpf, E. Seise, J. Limpert, and A. Tünnermann, "The impact of spectral modulations on the contrast of pulses of nonlinear chirped-pulse amplification systems," *Optics Express*, vol. 16, pp. 16664-16674, 2008.

[2] M. D. Perry and G. Mourou, "Terawatt to Petawatt Subpicosecond Lasers " *Science*, vol. 264, pp. 917-924, 1994.

[3] A. Galvanauskas, "Mode-scalable fiber-based chirped pulse amplification systems," *IEEE Journal of Selected Topics in Quantum Electronics*, vol. 7, pp. 504-517, 2001.

[4] B. E. Lemoff and C. P. J. Barty, "Quintic-phase-limited, spatially uniform expansion and recompression of ultrashort optical pulses," *Optics Letters*, vol. 18, pp. 1651-1653, 1993.

Chapter 7 High energy femtosecond Yb-fiber chirped pulse amplification system with adaptive phase control

This chapter presents a novel approach for the operation of an Yb-fiber CPA system with strong SPM, by shaping the spectral-phase (the phase of the electric field in the frequency domain) of the input pulses. The pre-compensation of both SPM phase distortion at high energies, and residual dispersion from mismatched stretcher/compressor technologies at low energies are investigated. The improvement of pulse quality, made by using a computer controlled adaptive control loop with the feedback from the output autocorrelation, has been demonstrated. This technique could be used to achieve high quality pulses beyond the limit of SPM in fiber CPA systems.

7.1 Introduction

Femtosecond pulse-shaping methods have become popular, within the Ti:Sapphire ultrafast laser research community, for overcoming the residual stretcher/compressor dispersion mismatch and SPM induced distortions in lasers and CPA systems [1-9]. There have been several reports of the use of computer optimization routines, coupled directly with a femtosecond pulse-shaper, for either minimizing pulse duration or for generating waveforms of arbitrary temporal shape. This approach has been useful because the adaptive learning optimization algorithms rapidly search through the large parameter space for the required pulse shape. Recently, ultrafast fiber laser researchers have reported the first demonstrations of the use of adaptive technology in fiber CPA systems [10]. Spectral amplitude shaping has been demonstrated at low energies, creating parabolic pulses that maintain a linear chirp in the presence of SPM (B-integral values up to 16 radians). Phase modulation using a $LiNbO_3$ electro-optic phase modulator has also been demonstrated [11] for low energy pulses.

This chapter presents an Yb-fiber CPA system, incorporating a computer controlled phase-only pulse shaper, developed to produce high quality 800 fs 65 μJ pulses. Two

variants of the system are reported. The first variant includes a dielectric grating stretcher and compressor with matched dispersive characteristics, and shaping the pulses increases the autocorrelation peak by a factor of 2.9 compared to unshaped pulses. The second variant uses 5 km of fiber as a pulse-stretcher, which results in substantially mismatched third order dispersion after the compressor, and shaping increases the autocorrelation peak by a factor of 3.4 compared to unshaped pulses.

A liquid crystal spatial light modulator (SLM) based pulse shaper is used to enable operation at any chosen repetition rate. Shaping in the spectral domain is ideal for Yb-fiber CPA systems because, by appropriate time-gating of the seed pulses, CW pumping can be used to operate at repetition rates from kHz to GHz to enable power scaling to > 100 W average power. Phase shaping is able to offset the pulse broadening effect of SPM in the amplifiers [12], and to compensate for mismatched dispersion between different stretcher and compressor technologies. In contrast, spectral amplitude shaping alone is not able to compensate for dispersion mismatches when the SPM is low. Furthermore, phase only shaping requires a single mask SLM whereas combined phase and amplitude shaping requires a more costly dual mask SLM.

The computer control loop varies a reduced set of Taylor coefficients for the shaper phase profile, and enables the autocorrelation peak to be improved substantially in approximately two minutes. The adaptive learning loop target is to maximize the autocorrelation absolute peak to pedestal difference that is measured and output from the oscilloscope. For many applications, where the peak power of the pulse is the critical parameter, this would be a useful target. More complex pulse-measurement techniques may be required to achieve other pulse shapes or objective functions. A generalized simulated annealing (GSA) control algorithm is used in these experiments as it is easy to implement computationally.

The chapter is organized as follows. Section 7.2 describes the experimental techniques and the implementation of adaptive control. The optimization results are presented in Section 7.3, where the pulse autocorrelations are shown for the dielectric grating stretcher setup, and then for the fiber stretcher setup. Section 7.3 also describes possible strategies for future optimization of the system. Concluding remarks are given in Section 7.4.

7.2 Experimental setup

The schematic of the phase controlled, Yb-fiber, CPA system is shown in Figure 7.1. The commercial Nd:glass laser system, as described in detail in Chapter 4, is used as the seed

source. The seed laser pulses are first phase-shaped and then stretched in duration, using either the dielectric grating stretcher or a 5 km length of Corning SMF28e fiber. With the shaper turned off, the pulse duration at the output of the stretcher is measured to be 1 ns for the dielectric grating stretcher and 0.8 ns for the fiber stretcher, by using a Tektronix 10 GHz fast photo-detector and a Tektronix CSA 803A communications signal analyzer.

The amplifier cascade is very similar to the one that has been described in Chapter 6. For the high energy results, an EOM and two AOMs are used to reduce the repetition rate from 80 MHz to 16.67 kHz. Using both dielectric grating and fiber stretcher setups, it is estimated that the launched pump power was 3 W into the final amplifier and that the launched energy at the input and output of the final amplifier are 2 μJ and 100 μJ, respectively. The overall transmission efficiency of the dielectric grating compressor is ~65%.

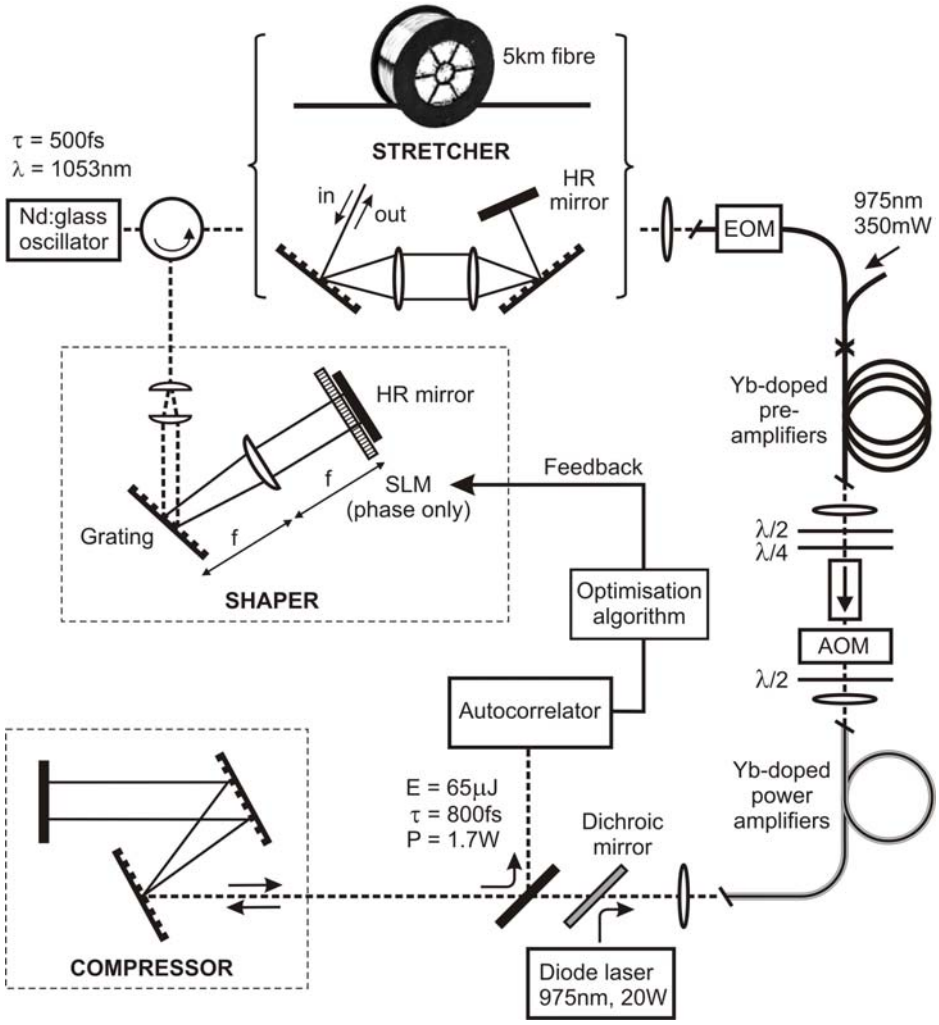

Figure 7.1: Schematic of fiber CPA system with adaptive phase control.

Prof. D. P. Shepherd's research group at ORC is responsible for the design, alignment, and control of the pulse shaper. The pulse shaper includes a telescope to expand the input beam to a dimension of 6 mm ($1/e^2$ intensity half-width) in the plane of incidence of the grating. The grating groove density is 1100 lines/mm and it is oriented at a 10 degree incidence angle. A cylindrical lens (f=200 mm) focused the beam, and a 128-pixel, 12.8 mm wide, single-mask, phase-only, liquid crystal SLM (model number: SLM-128-MIR from CRI) is placed at the Fourier plane of the folded 4f setup [1]. The optical resolution of the 4f setup is calculated to be 0.04 nm [1]. The pixel separation of the shaper implies that the spectrum could be manipulated in blocks of width 0.078 nm. The transmission window of the shaper is 10 nm.

The control loop is approached as a global optimization problem, using the GSA algorithm [13]. Simulated annealing algorithms are stochastic based, whereby worse solutions have a probability to be accepted to avoid local minima. In GSA, next solutions evolve in random directions according to the Tsallis-Stariolo distribution/generator [13]. The search parameters of the algorithm are the coefficients of the spectral phase, β_n, whilst the return value is the absolute difference from autocorrelation peak to pedestal-minimum across the viewable time-range that is output from the oscilloscope. Although simulated annealing algorithms normally start at random initial values, here the GSA algorithm is started from $\beta_n = 0$, because it is expected that the amount of the necessary phase correction will be small. Furthermore, a reflective boundary condition is applied within the search space. For the dielectric grating stretcher configuration, the $\beta_2 \ldots \beta_6$ terms are optimized. For the fiber stretcher, it is found that including $\beta_1 \ldots \beta_4$ dispersion terms improved results, whereas adding β_5 and β_6 terms led to minimal improvements and so these terms are finally omitted. Following initial trials, the search algorithm typically runs for 150 iterations and took ~2 minutes to optimize the autocorrelation peak.

7.3 Results

7.3.1 Dielectric grating stretcher setup

As discussed in Chapter 6, the design of the dielectric grating stretcher is carefully optimized. Therefore the recompressed pulses at low energy are of high quality, as shown by the autocorrelation traces in Figure 7.2 (a). The results in Figure 7.2 (a) also

demonstrate the limits imposed by strong SPM, because 65 μJ pulses without shaping are severely distorted (estimated B-integral~2.5π). The 65 μJ autocorrelation FWHM has increased from ~1.2 ps to ~1.4 ps and there is a pedestal which could not be removed by optimizing the grating separation in the compressor to maximize the autocorrelation peak. The corresponding pulses have bandwidth of 2.5 nm at the final amplifier input, and have a bandwidth of 2.6 nm at the output.

The improvement in pulse quality, achieved by phase shaping with strong SPM, is shown for E = 65 μJ in Figure 7.2 (b). The grating separation in the compressor is adjusted to maximize the autocorrelation peak of the unshaped 65 μJ pulses and then held constant while the feedback loop finds the optimum shaped pulse. The unshaped pulses are severely distorted, but shaping increases the autocorrelation peak by a factor of 2.9, reduces the pedestal, and decreases the autocorrelation FWHM from 1.4 ps to 1.1 ps (~800 fs deconvolved Gaussian pulse; $\Delta\nu\Delta\tau \sim 0.45$). The Fourier transform of the output spectrum with a flat phase is a reasonable match to the shaped-pulse autocorrelation.

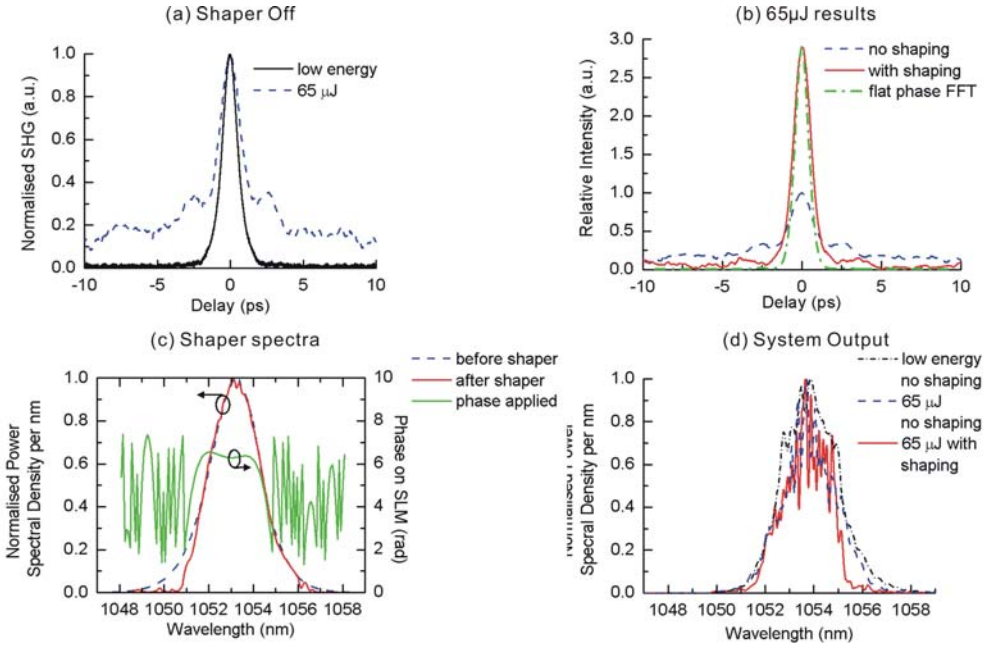

Figure 7.2: Results with dielectric grating stretcher. (a) Autocorrelation without phase control at low energy and at 65 μJ. (b) Autocorrelation of 65 μJ pulses without (dashed blue) and with (solid red) phase shaping, and the flat-phase Fourier transform of the system output spectrum when shaping is applied. (c) Spectra at the input (dashed blue) and output (solid red) of the pulse shaper. The phase applied is also shown. (d) System output spectra.

Figure 7.2 (c) shows the spectra at the input and output of the pulse shaper at 65 μJ , which confirms that the spectral amplitude is not significantly shaped or distorted. Figure 7.2 (c) also shows the applied phase for the optimized 65 μJ pulses. Figure 7.2 (d) shows the spectra at the output of the system for different pulse energies. The spectra without shaping at low energy, and with shaping at high energy are generally of similar shape. The spectral ripples on the high energy spectra are believed to be due to a combination of polarization and nonlinear interactions in the final amplifier fiber, because adjustment of the half-waveplate at the input of the amplifier minimizes, but can not eliminate, the ripples at low pulse energies, and the ripples become stronger at high pulse energies [14].

7.3.2 Fiber stretcher setup

With the fiber stretcher, the third order dispersion adds to that of the compressor and even without SPM the resultant third order dispersion gives rise to a pedestal, as shown by the autocorrelation traces in Figure 7.3 (a). A further complication is that strong spectral broadening is observed after the stretcher fiber because the high peak powers of the ~500 fs un-stretched input pulses leads to SPM. Although SPM in the stretcher fiber can be avoided by attenuating the seed pulse energy, in order to obtain high energies at the system output it is found to be necessary to launch increased seed pulse energies through the stretcher to minimize noise in the amplifiers. Therefore the shaper is required to compensate three effects: the stretcher/compressor third order dispersion mismatch, the SPM spectral broadening of the initially unchirped pulses in the 5 km of Corning fiber, and the SPM acting on the strongly chirped pulses in the amplifier fiber. In the first experiment, with low SPM in both the stretcher and the amplifier fibers, the dielectric grating compressor grating separation is first adjusted to optimize the pulse without shaping and then the grating separation is fixed while the search algorithm operates to increase the autocorrelation peak. With high SPM in the stretcher fiber, shaping experiments are performed with the compressor grating offset from this starting position by up to ± 2 %. When there is low SPM in the amplifier fibers, reducing the grating separation by 1 % (~30 mm) enables the largest improvement in the autocorrelation when the shaper operated. For high pulse energies, reducing the compressor grating separation by 0.7 % (~20 mm) enables the largest improvement in the autocorrelation when the shaper operates.

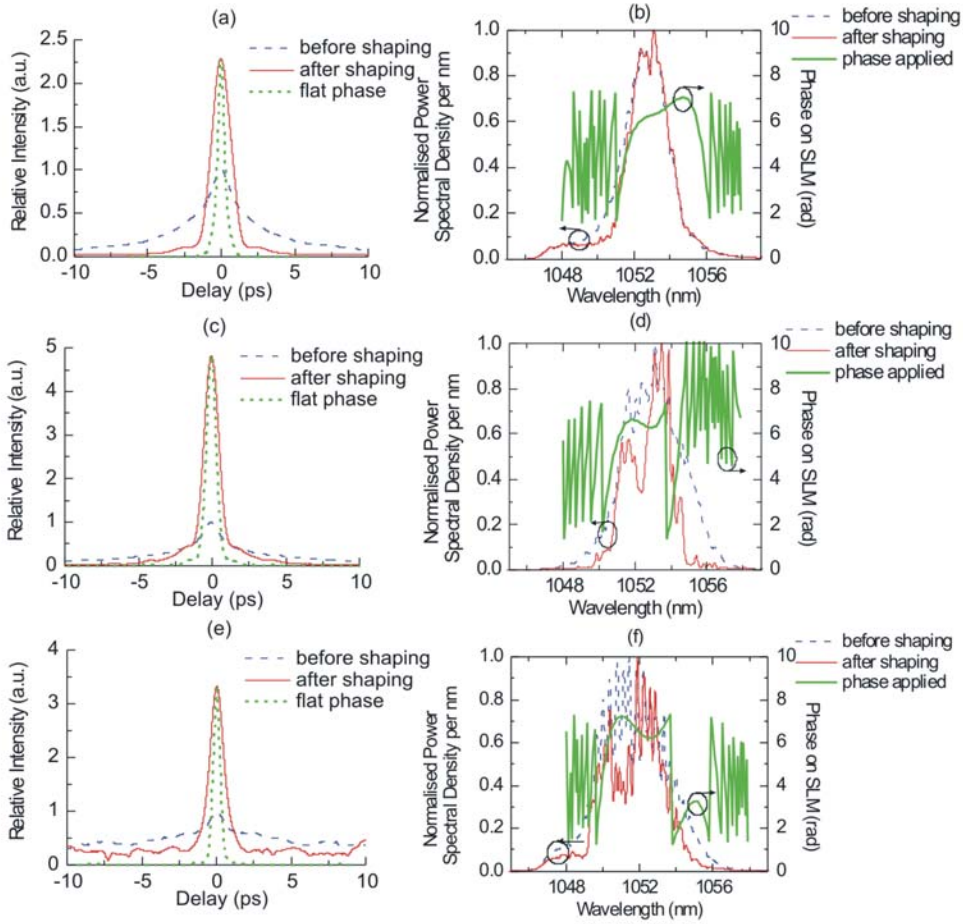

Figure 7.3: Results with fiber stretcher. (a), (c), (e) Autocorrelation traces: without (dashed blue) and with (solid red) phase shaping, and the flat-phase Fourier transform of the system output spectrum with shaping applied. (a) Low final energy, and low SPM in stretcher. (c) Low final energy, but high SPM in stretcher. (e) 65 μJ final pulses, and high SPM in stretcher. (b), (d), (f) System output spectra without (dashed blue) and with (solid red) phase shaping. The phase profiles applied are also shown.

As shown by the autocorrelation traces in Figure 7.3 (a), (c), and (e), shaping produces a significant increase in the autocorrelation peaks in all cases. For the low energy pulses either with or without SPM in the stretcher fiber, the pedestal is also reduced. For the 65 μJ pulses, the autocorrelation pedestal is reduced somewhat, but not as much as for the low energy pulses. The Fourier transforms of the output spectra with a flat phase generally show a narrower pulse than is obtained experimentally, even at low pulse energies. It is thought to be due to the limitations of the pixilated shaper that is not able to completely correct for the phase with increased complexity in the case of the fiber stretcher.

Figures 7.3 (b), (d), and (f), show the spectra at the system output and also the phase profiles that are applied by the shaper. The spectra, measured on a dB scale (not shown),

demonstrate that in all cases the signal is more than 20 dBm/nm above the ASE noise level, measured at a resolution of 0.1 nm. The spectrum is not significantly changed by pre-shaping when there is no SPM in the stretcher. With SPM in the stretcher, the spectrum is modified by the shaper both at the system output (shown) and immediately after the stretcher fiber (not shown). The spectrum from the stretcher fiber varies because the SPM is sensitive to the chirp of the input pulse set by the shaper. The variations in spectral bandwidth at the stretcher output would have led to different stretched pulse durations, depending on the position along the fiber where the new spectral components are generated, and hence in the amount of dispersion those broadened spectral components experienced. For the 65 μJ results, the pulse energy launched into the stretcher fiber is ~150 pJ, and the energy is ~25 pJ at the output. The pulse durations at the input and output of the stretcher fiber are not measured when the shaper is active, and so it is not straightforward to estimate that B-integral without nonlinear numerical modeling.

7.3.3 Discussion

In theory, a pulse that is stretched by a large factor with mainly linear dispersion, as in the dielectric grating stretcher, evolves into the Fourier transform of the initial pulse [12], such that the effect of SPM on the spectral phase of the stretched pulse can be compensated by spectral phase shaping. However, that theory requires a constant spectrum as the pulse is subject to SPM, whereas in a fiber CPA system the spectrum is altered by gain-shaping, as demonstrated by comparison of the spectra in Figure 7.2 (c) and (d). Therefore the improvement in the autocorrelation peak using the dielectric grating stretcher demonstrates the ability of the computer controlled learning loop to operate with the complex interaction of gain-narrowing and SPM in the fiber amplifiers.

In the fiber stretcher, SPM acts on a very weakly chirped pulse which is qualitatively different from the action of SPM on the strongly chirped pulse in the amplifier fiber. In this case the adaptive approach could be perhaps used as a tool to investigate the pulse evolution in the stretcher and amplifier fibers since it enables the optimum input phase to be determined for a given target pulse profile. That knowledge could assist, for example, in determining the required parameters for a numerical model of the system. It is noted that other groups have considered pulse delivery through short fiber lengths by phase pre-compensation for the effects of both SPM and dispersion [15, 16], but that work is not a close match to our 5 km stretcher fiber and the subsequent pulse amplification system.

When considering possible improvements to the system, it is first noted that, at pulse energies above 65 μJ, the autocorrelation pedestal is not eliminated by the shaper. This can be due to the limited complexity of the phase that the pixilated shaper can provide. For example, the shaper doesn't physically provide the required rate of phase change when the calculated phase profile has a rate of change of more than 2π per pixel, such as in the wings of the pulses as shown in Figure 7.2 and 7.3. In addition, the increase of the autocorrelation pedestal in the time domain is accompanied by the increased spectral modulations. It is possible that the SPM has induced a similarly rapid variation in the spectral phase of the pulses which adds to the complexity of the required phase correction. Moreover, the limited number of dispersion coefficients controlled by the algorithm also implies a maximum complexity of the shaped phase. Ultimately, a pixel by pixel optimization algorithm may provide the highest degree of pulse clean-up. Other limitations are imposed by the pixelated shaping device, such as the resolution limit which controls the maximum time-span, the limited number of pixels which controls the maximum complexity of the shaped pulse [1], and a known variety of pulse imperfections as described in detail by Vaughan et al. [17]. An improved system could therefore include an SLM with more pixels and a pixel by pixel optimization algorithm. Furthermore, switching to a combined phase and amplitude modulator could, for example, enable investigations with pre-shaped spectra to compensate for gain narrowing effects.

7.4 Conclusion

It is demonstrated that spectral-phase pre-shaping, controlled by an adaptive feedback loop, improves the pulse quality from an Yb fiber CPA system operated with strong SPM and residual third-order dispersion from mismatched stretcher/compressor technologies. High-quality 65 μJ recompressed pulses, with duration of 800 fs, are produced, and the autocorrelation peak of the shaped pulses is 2.9 and 3.4 times higher for grating and fiber stretchers, respectively, compared to the unshaped pulses. The use of a reduced set of Taylor coefficients for the shaper phase profile enables the autocorrelation peak to be improved substantially in approximately two minutes.

In future, phase shaping could enable switching from the grating stretchers to more compact technologies by compensating for the dispersion mismatches that arise. For example, compact and relatively inexpensive fiber stretchers, or CFBG stretchers could be used. Phase shaping can also optimize the pulse duration when using novel

compressor technologies that have complex dispersion profiles, such as hollow core photonic bandgap fibers. Scaling the average power from the ~1.1 W used in these experiments to >100 W should be possible by increasing the pulse repetition rate and by using higher power pump laser-diodes.

The results shown in this chapter demonstrate the possibility of power-scaling ultrashort pulse fiber systems by enabling the production of high quality, high energy pulses when there is significant SPM in the amplifier fiber. The work has been published in [18, 19], and the demonstration of combined spectral amplitude and phase pre-shaping is subsequently reported by our research group using a parabolic pulse amplification scheme [20].

References:

[1] A. M. Weiner, "Femtosecond pulse shaping using spatial light modulators," *Review of Scientific Instruments*, vol. 71, pp. 1929-1960, 2000.

[2] T. Brixner, A. Oehrlein, M. Strehle, and G. Gerber, "Feedback-controlled femtosecond pulse shaping," *Applied Physics B-Lasers and Optics*, vol. 70, pp. S119-S124, 2000.

[3] A. Efimov, M. D. Moores, B. Mei, J. L. Krause, C. W. Siders, and D. H. Reitze, "Minimization of dispersion in an ultrafast chirped pulse amplifier using adaptive learning," *Applied Physics B-Lasers and Optics*, vol. 70, pp. S133-S141, 2000.

[4] A. Efimov and D. H. Reitze, "Programmable dispersion compensation and pulse shaping in a 26-fs chirped-pulse amplifier," *Optics Letters*, vol. 23, pp. 1612-1614, 1998.

[5] A. Efimov, M. D. Moores, N. M. Beach, J. L. Krause, and D. H. Reitze, "Adaptive control of pulse phase in a chirped-pulse amplifier," *Optics Letters*, vol. 23, pp. 1915-1917, 1998.

[6] T. Tanabe, K. Ohno, T. Okamoto, M. Yamanaka, and F. Kannari, "Feedback control for accurate shaping of ultrashort optical pulses prior to chirped pulse amplification," *Japanese Journal of Applied Physics Part 1-Regular Papers Short Notes & Review Papers*, vol. 43, pp. 1366-1375, 2004.

[7] K. Ohno, T. Tanabe, and F. Kannari, "Adaptive pulse shaping of phase and amplitude of an amplified femtosecond pulse laser by direct reference to frequency-resolved optical gating traces," *Journal of the Optical Society of America B-Optical Physics*, vol. 19, pp. 2781-2790, 2002.

[8] G. Cheriaux, O. Albert, V. Wanman, J. P. Chambaret, C. Felix, and G. Mourou, "Temporal control of amplified femtosecond pulses with a deformable mirror in a stretcher," *Optics Letters*, vol. 26, pp. 169-171, 2001.

[9] D. Yelin, D. Meshulach, and Y. Silberberg, "Adaptive femtosecond pulse compression," *Optics Letters*, vol. 22, pp. 1793-1795, 1997.

[10] D. N. Schimpf, J. Limpert, and A. Tünnermann, "Controlling the influence of SPM in fiber-based chirped-pulse amplification systems by using an actively shaped parabolic spectrum," *Optics Express*, vol. 15, pp. 16946-16953, 2007.

[11] G. H. Zhu, J. Edinberg, and C. Xu, "Nonlinear distortion free fiber-based chirped pulse amplification with self-phase modulation up to 2 pi," *Optics Express*, vol. 15, pp. 2530-2534, 2007.

[12] A. Braun, S. Kane, and T. Norris, "Compensation of self-phase modulation in chirped-pulse amplification laser systems," *Optics Letters*, vol. 22, pp. 615-617, 1997.

[13] C. Tsallis and D. A. Stariolo, "Generalized simulated annealing," *Physica A*, vol. 233, pp. 395-406, 1996.

[14] D. N. Schimpf, E. Seise, J. Limpert, and A. Tünnermann, "The impact of spectral modulations on the contrast of pulses of nonlinear chirped-pulse amplification systems," *Optics Express*, vol. 16, pp. 16664-16674, 2008.

[15] F. G. Omenetto, A. J. Taylor, M. D. Moores, and D. H. Reitze, "Adaptive control of femtosecond pulse propagation in optical fibers," *Optics Letters*, vol. 26, pp. 938-940, 2001.

[16] M. Tsang, D. Psaltis, and F. G. Omenetto, "Reverse propagation of femtosecond pulses in optical fibers," *Optics Letters*, vol. 28, pp. 1873-1875, 2003.

[17] J. C. Vaughan, T. Feurer, K. W. Stone, and K. A. Nelson, "Analysis of replica pulses in femtosecond pulse shaping with pixelated devices," *Optics Express*, vol. 14, pp. 1314-1328, 2006.

[18] F. He, H.S.S.Hung, N.K.Daga, N.Naz, J.Prawiharjo, J.H.V.Price, D.C.Hanna, D.P.Shepherd, D.J.Richardson, J.W.Dawson, C.W.Siders, and C.P.J.Barty, "High energy femtosecond fiber chirped pulse amplification system with adaptive phase control," in *Conference on Lasers and Electro-Optics*. San Jose Optical Society of America, 2008, CThB5.

[19] F. He, H.S.S.Hung, J.H.V.Price, N.K.Daga, N.Naz, J.Prawiharjo, D.C.Hanna, D.P.Shepherd, D.J.Richardson, J.W.Dawson, C.W.Siders, and C.P.J.Barty, "High energy femtosecond fiber chirped pulsed amplification system with adaptive phase control," *Optics Express*, vol. 16, pp. 5813-5821, 2008.

[20] J. Prawiharjo, N. K. Daga, R. Geng, J. H. Price, D. C. Hanna, D. J. Richardson, and D. P. Shepherd, "High fidelity femtosecond pulses from an ultrafast fiber laser system via adaptive amplitude and phase pre-shaping," *Optics Express*, vol. 16, pp. 15074-15089, 2008.

Chapter 8 Conclusion and future work

8.1 Conclusion

This thesis focused on the development of Yb-doped fiber based CPA systems. Two approaches, aiming at either scaling of average power or scaling of pulse energy, have been investigated. In particular, this thesis research has described the development of a high average power system producing high quality ~360 fs pulses with 70 W average power and ~7 μJ energy (at a repetition rate of 10 MHz), and a high pulse energy system producing ~1100 fs pulses with ~130 μJ energy (at a repetition rate of 16.67 kHz). In both systems, further increase of pulse energy was limited by the onset of SPM induced pulse distortion.

Numerical models to predict the gain bandwidth of various Yb-doped fiber amplifiers, ranging from a low power, core-pumped, Yb/P/Al doped, single mode fiber amplifier to a high power, cladding-pumped, Yb/Al doped, LMA double-clad fiber amplifier, were described. All the simulation predictions were in good agreement with experimental results. The models have been used for optimizing the gain bandwidth of the amplifier cascade in the CPA systems, as gain narrowing during amplification can result in an increase in the minimum duration of the recompressed pulses. Subsequent experimental results proved the validity of the modeling predictions.

A number of the state-of-the-art technologies have been incorporated into the CPA systems, which enabled us to achieve a pulse energy and average power beyond the fiber CPA systems that were developed prior to this thesis research, or to implement more practical alternatives to the technologies previously used in systems of comparable performance. The collaboration with LLNL enabled us to access the world leading grating technologies for pulse stretching and compression. A dielectric grating stretcher, designed by LLNL with up to 5^{th} order phase dispersion coefficients matched to the compressor, was used in the high pulse energy version CPA system, and a dielectric grating compressor was used in both versions of the CPA systems. Compact CFBG stretchers, with up to 3^{rd} order dispersion matched to the dielectric grating compressor, were incorporated in the CPA systems. The CFBGs, made available by taking advantage

of the ORC's world leading CFBG fabrication facility, were characterized by using the measurement setups that were developed in this thesis research. Besides the pulse stretcher and compressor, the CPA systems also incorporated the most advanced fiber technologies. LMA fibers were used in the system by taking advantage of the ORC's fiber fabrication facility. PCF was used in the later developments due to its advantages for the amplification of high intensity pulses, and also because of the fire in which the ORC had lost its fiber fabrication ability.

This thesis research also developed a fiber CPA system with adaptive control of the spectral phase. The pulse shaper, provided by Prof. D. P. Shepherd's research group at the ORC, enabled pre-compensation of both SPM phase distortion and residual dispersion from mismatched stretcher/compressor technologies, and was self-optimizing for operation at both low and high pulse energies. Spectral phase shaping of the seed pulses had demonstrated an improved pulse quality in experiments. This novel approach could benefit fiber CPA systems operating with strong SPM, and allow the use of compact pulse stretchers which did not have dispersion characteristics matched to the compressor.

8.2 Future work

Fiber lasers have the potential for a wide range of applications, such as supercontinuum sources [1], frequency combs for optical metrology [2], and fiber based sources for frequency conversion to other wavelengths including X-ray (high harmonic generation), UV (third harmonic generation, or sum-frequency generation), visible (second harmonic generation), mid-IR (parametric amplification), and Terahertz (difference frequency generation). In addition, ultrafast fiber lasers have become the replacements for conventional mode-locked bulk glass or crystal lasers in many industrial applications such as micro-machining, ophthalmology, and microscopy.

A variety of applications have been enabled by the development of the fiber CPA systems presented in this thesis. The most desirable progress resulting from this thesis would be the demonstration of high harmonic generation in argon gas to generate ultra-short pulse X-rays in the wavelength range of 10-50 nm. Followed by the successful development of the high pulse energy fiber CPA system in this thesis research, our group is working in collaboration with the Physics department in the University of Southampton on this particular application of the system (http://www.phys.soton.ac.uk/xray/). Besides the desired target of the project, the fiber

CPA systems can also be directly applied to other applications, including micro-machining, green light generation, UV generation, Terahertz generation, supercontinuum generation, and pumping optical parametric oscillators and optical parametric amplifiers. Moreover, the research presented in this thesis has been used by Prof. D. P. Shepherd's group for the EPSRC project on the 'An Intelligent Mid-Infrared Pulse Generator for Experiments in Coherent Control', in which a similar ultrafast fiber laser has been built for pumping an optical parametric oscillator (http://www.orc.soton.ac.uk).

Besides the range of interesting applications, future development of fiber CPA systems beyond the content of this thesis includes the improvement of the numerical models, further scaling of pulse energy, further scaling of average powers, and the incorporation of features such as carrier envelope phase locking [3], adaptive phase compensation and nonlinear pulse compression, which will be discussed in the following paragraphs.

The numerical models that were developed in this thesis research are based on spectrally-resolved steady-state models. The high peak powers in pulsed applications of Yb-fiber amplifiers pose unique challenges not fully addressed by these models, and future work could be usefully directed towards the release of additional modelling tools to address these specific challenges, such as the incorporation of nonlinear and dispersive effects within the current models. The effective overlap integral approach has been used in the current model to reduce the computations required. However, for high power LMA amplifiers, it may be helpful to develop new models for multi-mode fibers, and include bending loss calculations for all the modes.

As the pulse energy is limited mainly by SPM in the CPA systems that have been developed in this thesis research, further power scaling of the pulse energy can be achieved by using fibers with even larger effective mode areas. For example, fibers with core diameters of 70-80 μm have been reported in rod-type PCFs [4, 5], as well as in LMA fibers [6, 7]. The pulse energy of the current high pulse energy CPA system could be extended to ~1 mJ in future by applying the most recent developments in rod-type PCF technology.

Yb-fiber technology has advantages in high average power operation because Yb has a low quantum defect, and fiber has a favourable geometry for heat dissipation. These advantages have been fully exploited for CW operation where industrial research has led to a commercial Yb-fiber laser with an average power of 50 kW (http://www.ipgphotonics.com). In pulsed applications, 100 W level average power has been demonstrated at low pulse energies in several fiber CPA systems including the work presented in this thesis [8-10]. A possible avenue for future development of the high

power CPA system is to maintain the high pulse energy at or above the ~100 μJ level but to exploit higher average power by increasing the pulses higher repetition rates, e.g. 100 μJ at 1 MHz implies 100 W average power.

The carrier envelope phase has an important effect in 'extreme nonlinear optics' applications where pulses of few optical cycles and sufficiently high intensity are used such that the pulse electric field, rather than the intensity, is relevant, such as X-ray generation [11]. Carrier envelope phase dependence in X-ray generation has been reported in reference [12], in which uncontrolled carrier envelope phase resulted in fluctuations in the signal. Future development of the project could consider incorporating carrier envelope phase locking to assist the X-ray generation. Moreover, with the advances in the carrier envelope phase control, the pulse train enhancement in passive cavities has become feasible [13, 14]. The first fiber CPA seeded enhancement cavity was reported in 2007. In this system, the high repetition rate (136 MHz) pulse train from the fiber CPA system is coherently added inside a passive ring cavity by controlling the fiber oscillator's pulse repetition rate and carrier envelope offset frequency [15, 16]. The system produced an intracavity peak intensity of 3×10^{14} W/cm^2, and ionization of noble gases has been demonstrated. Such systems could be applied to our project for X-ray generation in the future.

In respect to the incorporation of pulse shaping technology in the fiber CPA systems, the initial 'proof of principle' research in this thesis demonstrated the possibility of power-scaling ultrashort pulse fiber systems by enabling the production of high quality, high energy pulses when there is significant SPM in the amplifier fiber. In future, combined spectral amplitude and phase pre-shaping could enable improved results at even higher pulse energies, and may allow optimum operation using a compact fiber stretcher with mismatched dispersive characteristics to the compressor. Furthermore, scaling the average power from the ~1 W of these experiments to >100 W should be possible by increasing the pulse repetition rate and by using higher power pump laser-diodes.

Finally, nonlinear pulse compression could be added to the current high pulse energy system to further reduce the pulse duration. A typical schematic for nonlinear pulse compression consists of a bandwidth generator, which generates the necessary chirp through a nonlinear interaction such as SPM, and a dispersive component acting as a pulse compressor to remove, or at least decrease, the chirp of the pulses [17-20].

References:

[1] J. H. V. Price, W. Belardi, T. M. Monro, A. Malinowski, A. Piper, and D. J. Richardson, "Soliton transmission and supercontinuum generation in holey fiber, using a diode pumped Ytterbium fiber source," *Optics Express*, vol. 10, pp. 382-387, 2002.

[2] J. Ye and S. Cundiff, *Femtosecond Optical Frequency Comb: Principle, Operation and Applications*: Springer, 2005.

[3] D. J. Jones, S. A. Diddams, J. K. Ranka, A. Stentz, R. S. Windeler, J. L. Hall, and S. T. Cundiff, "Carrier-Envelope Phase Control of Femtosecond Mode-Locked Lasers and Direct Optical Frequency Synthesis," *Science*, vol. 288, pp. 635-639, 2000.

[4] J. Limpert, N. D. Robin, I. Manek-Honninger, F. Salin, F. Roser, A. Liem, T. Schreiber, S. Nolte, H. Zellmer, A. Tunnermann, J. Broeng, A. Petersson, and C. Jakobsen, "High-power rod-type photonic crystal fiber laser," *Optics Express*, vol. 13, pp. 1055-1058, 2005.

[5] F. Röser, T. Eidam, J. Rothhardt, O. Schmidt, D. N. Schimpf, J. Limpert, and A. Tünnermann, "Millijoule pulse energy high repetition rate femtosecond fiber chirped-pulse amplification system," *Optics Letters*, vol. 32, pp. 3495-3497, 2007.

[6] K. H. Liao, K. C. Hou, G. Chang, V. Smirnov, L. Glebov, R. Changkakoti, P. Mamidipudi, and A. Galvanauskas, "Diffraction-Limited 65-μm Core Yb-doped LMA Fiber based High Energy Fiber CPA Systems," presented at Conference on Lasers and Electro-Optics, Long Beach, 2006, CPDB4.

[7] L. Dong, J. Li, and X. Peng, "Bend-resistant fundamental mode operation in ytterbium-doped leakage channel fibers with effective areas up to 3160 μm^2," *Optics Express*, vol. 14, pp. 11512-11519 2006.

[8] J. Limpert, T. Clausnitzer, A. Liem, T. Schreiber, H. J. Fuchs, H. Zellmer, E. B. Kley, and A. Tunnermann, "High-average-power femtosecond fiber chirped-pulse amplification system," *Optics Letters*, vol. 28, pp. 1984-1986, 2003.

[9] F. Röser, J. Rothhard, B. Ortac, A. Liem, O. Schmidt, T. Schreiber, J. Limpert, and A. Tunnermann, "131 W 220 fs fiber laser system," *Optics Letters*, vol. 30, pp. 2754-2756, 2005.

[10] F. He, J. H. V. Price, A. Malinowski, A. Piper, M. Ibsen, and D. J. Richardson, "High Average Power, High Energy, Femto-second Fiber Chirped Pulse Amplification System," presented at Conference on Lasers and Electro-Optics, Baltimore, 2007, CMEE5.

[11] S. T. Cundiff, "Phase stabilization of ultrashort optical pulses," *Journal of Physics D: Applied Physics*, vol. 35, pp. R43-R59, 2002.

[12] C. G. Durfee, A. R. Rundquist, S. Backus, C. Herne, M. M. Murnane, and H. C. Kapteyn, "Phase Matching of High-Order Harmonics in Hollow Waveguides," *Physics Review Letters*, vol. 83, pp. 2187-2190, 1999.

[13] R. J. Jones and J. Ye, "High-repetition-rate coherent femtosecond pulse amplification with an external passive optical cavity," *Optics Letters*, vol. 29, pp. 2812-2814, 2004.

[14] C. Gohle, T. Udem, M. Herrmann, J. Rauschenberger, R. Holzwarth, H. A. Schuessler, F. Krausz, and T. W. Hansch, "A frequency comb in the extreme ultraviolet," *Nature*, vol. 436, pp. 234-237, 2005.

[15] I. Hartl, T. R. Schibli, A. Marcinkevicius, D. C. Yost, D. D. Hudson, M. E. Fermann, and J. Ye, "Cavity-enhanced similariton Yb-fiber laser frequency comb: 3×10^{14} W/cm^2 peak intensity at 136 MHz," *Optics Letters*, vol. 32, pp. 2870-2873, 2007.

[16] D. C. Yost, T. R. Schibli, and J. Ye, "Overcoming the power scalability limit in intracavity HHG," in *Conference on Lasers and Electro-Optics*. San Jose: Optical Society of America, 2008, CPDA10.

[17] C. V. Shank, R. L. Fork, R.Yen, R.H.Stolen, and W. J. Tomlinson, "Compression of femtosecond optical pulses," *Applied Physics Letters*, vol. 40, pp. 761-763, 1982.

[18] W. J. Tomlinson, R. H. Stolen, and C. V. Shank, "Compression of optical pulses chirped by self-phase modulation in fibers," *Journal of optical society of America B*, vol. 1, pp. 139-149, 1984.

[19] J. Moses and F. W. Wise, "Soliton compression in quadratic media: high energy few-cycle pulses with a frequency-doubling crystal," *Optics Letters*, vol. 31, pp. 1881-1883, 2006.

[20] M. Nisoli, S. D. Silvestri, and O. Svelto, "Generation of high energy 10 fs pulses by a new pulse compression technique," *Applied Physics Letter*, vol. 68, pp. 2793-2795, 1996.

Appendix I Modelling of pulse shaping due to dynamic gain saturation in fiber amplifiers

This appendix shows how high energy pulses, with user definable temporal profiles, can be created in a gain-saturated amplifier by suitable pre-shaping of the low-energy input pulses. Based on the successful development of the Yb-fiber gain model, as presented in Chapter 3, this modeling approach is developed to support another commercially funded ORC project in Prof. D. J. Richardson's research group. The model simulates the gain saturation effects of a high pulse energy system producing 100 ns pulses, and the modeling results have been applied into experiments to create desired output pulse profiles.

A1.1 The gain-dynamic model

In many industrial applications, such as marking and material processing, the precise laser pulse temporal profile is critical for determining the accuracy of the material finish, and the precise spectral characteristics are of secondary importance. When the pulse energy is above the saturation fluence of the amplifier, dynamic gain saturation causes the leading edge of the pulse to experience a higher gain compared to the trailing edge, and the output pulse profile becomes distorted. The saturation fluence can be calculated according to

$$F_{sat} = h\upsilon_s / (\sigma_e(\lambda) + \sigma_a(\lambda)) \tag{A1.1}$$

where h is Plank constant, υ_s is the frequency of the signal, σ_a and σ_e represent the absorption and emission cross section, respectively. The calculated saturation fluence is typically ~0.3 μJ/μm^2 for Yb-doped fibers operating at ~1 μm [1], and the saturation energy (which is equal to the mode area multiplied by the saturation fluence) is only about 10 μJ for a standard single mode fiber. However, by taking advantage of LMA fibers, in which the mode area can be expanded while maintaining single mode guidance, the saturation energy can be significantly increased [2, 3].

The steady-state model (as described in Chapter 3) is unsuitable in the case when time dependent gain plays a significant pulse shaping role, and here the results obtained from gain dynamic modeling of a high pulse energy Yb-fiber amplifier with 100 ns pulses are presented. The model is used to find appropriate pre-shaping profiles for input pulses that enabled us to obtain a variety of tailored output pulse shapes by incorporating the effects of gain saturation across the pulses.

The time dependent upper level ion fraction $N_2(t,z)$ and gain $g(\lambda,t,z)$ in an element of Yb-fiber amplifier can be simulated by the following, time-dependent, two-level rate and propagation equations using the effective overlap integral parameter, described in Chapter 3.

$$\frac{\partial N_2(t,z)}{\partial t} = [R_{12}(\lambda)+W_{12}(\lambda)]N_1(t,z)-[R_{21}(\lambda)+W_{21}(\lambda)+A_{21}]N_2(t,z) \tag{A1.2}$$

$$\frac{\partial P_s(\lambda,t,z)}{\partial z}+\frac{1}{\mathrm{v}}\frac{\partial P_s(\lambda,t,z)}{\partial t} = \Gamma_s(\lambda)[\sigma_e(\lambda)N_2(t,z)-\sigma_a(\lambda)N_1(t,z)]\rho P_s(\lambda,t,z) - \alpha_s P_s(\lambda,t,z) \tag{A1.3}$$

$$\pm\frac{\partial P_p^{\pm}(\lambda,t,z)}{\partial z}+\frac{1}{\mathrm{v}}\frac{\partial P_p^{\pm}(\lambda,t,z)}{\partial t} = \Gamma_p(\lambda)[\sigma_e(\lambda)N_2(t,z)-\sigma_a(\lambda)N_1(t,z)]\rho P_p^{\pm}(\lambda,t,z) - \alpha_p P_p^{\pm}(\lambda,t,z) \tag{A1.4}$$

Parameters are the same as described in Chapter 3, and v is the velocity of light in fiber [4]. (ASE terms are included in the model, but are not written explicitly above, and ASE is not a strong factor in the experiments considered in this section.)

The inclusion of time dependent gain requires more computational resources compared with the steady-state model. The gain dynamic model I have used is based on a simplified model, proposed by Bononi *et al.* [5], that was developed for telecommunications to study the adding or dropping of signal channels in wavelength division multiplexed networks. The set of coupled nonlinear differential equations (Equations (A1.2)-(A1.4)) are simplified by Sun *et al.* into a single ordinary differential equation [6]. Independently, Bononi and Chinn further simplify Sun's model by introducing a parameter called the 'reservoir', $r(t)$, which is the total number of excited ions in the fiber:

$$r(t) \approx \rho\, A_{eff} \int_0^L N_2(t,z)\, dz \quad , \tag{A1.5}$$

where L is the fiber length and ρ is the ion density and A_{eff} is the effective core area [7]. Thus the dynamic model can be simplified as:

$$\dot{r}(t) = -\frac{r(t)}{\tau} + \sum_{j=0}^{N} \frac{P_j^{in}(t)}{h\upsilon_j} \left[1 - e^{B_j r(t) - C_j} \right], \tag{A1.6}$$

where P_k^{in} is the input optical power of channel k, $k = 0, \ldots, N$, including all the signal channels as well as the pump channel. $B_k = \Gamma_k(\sigma_{ak} + \sigma_{ek})/A_{eff}$ and $C_k = \rho \Gamma_k \sigma_{ak} L$ are dimensionless parameters [5, 8].

I first modeled the system previously considered in a paper by Wang and Po in which the full coupled nonlinear differential equations (Equations (A1.2)-(A1.4)) were numerically solved by using finite difference methods for high energy, nanosecond, pulses in an Yb-fiber amplifier [9]. I found that the results were in close agreement with the published simulations which provided verification of the accuracy of the simplified model. Note that the analytical solution to the pulse pre-shaping in fiber amplifiers has been reported four years after the work presented in this appendix has been performed [10].

A1.2 Optimised pre-shaping of input pulses to compensate for gain dynamic pulse shaping

Here I show results for an Yb-fiber laser and amplifier system consisting of a fiber-pigtailed pulsed laser diode operating at 1080 nm, and two Yb-fiber amplifier stages. The source is a directly modulated laser diode driven at a repetition rate of 20 kHz, and the output pulse profile is shaped by programming the input electrical driving signal generator. The laser is not wavelength stabilized, and produced chirped pulses with a bandwidth of approximately 2.5 nm. The bandwidth of the amplified pulses, which increase with the increase of pulse energies, increase to ~5.5 nm at the maximum energies of ~0.35 mJ.

The two amplifier stages are commercial units, which fully spliced to pump and signal fibers and patented as GT-Wave Yb-fiber amplifiers from SPI Lasers Ltd (www.spilasers.com). The first GT-Wave amplifier has a 10 m long fiber with 6 μm core (calculated saturation energy of 0.017 mJ), and is backward pumped by a 1 W pigtailed laser diode at 915 nm. The second GT-Wave amplifier has a 7 m long fiber with 20 μm core (calculated saturation energy of 0.19 mJ), and is backward pumped by a 25 W pigtailed laser diode at 915 nm. Due to the pump coupling loss in the setup, and because of GT-Wave's pump-coupling structure, the measured incident pump powers are not

fully transferred to the gain fiber. Therefore, effective pump powers are used in the simulations, with the same effective pump power coefficient.

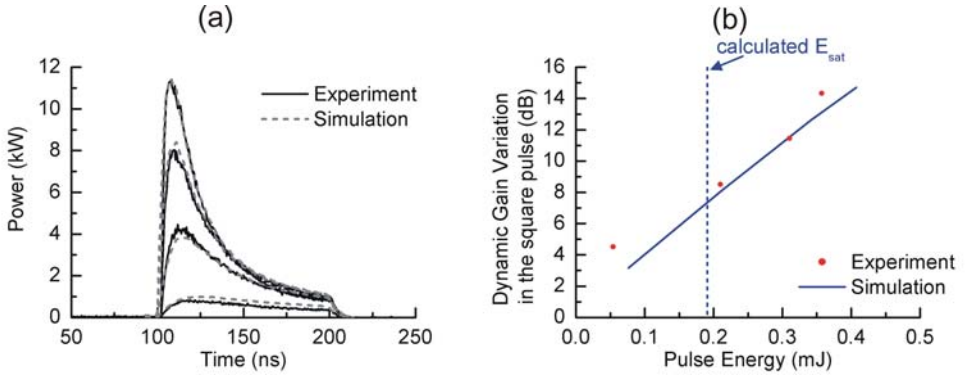

Figure A1.1: Output pulse shaping and dynamic gain variation for a square input pulse. (a)Shows output pulse shapes from the final amplifier at pump powers of 5.7 W, 13.7 W, 21.7 W, and 25.7 W, respectively; (b) shows the maximum gain variation between the leading and trailing edge of the output pulse at different output pulse energies.

Initially, the input signal consists of square pulses (35 nJ energy, 100 ns duration, 0.35 W peak power). The first GT-Wave amplifier uses a constant 1 W of pump power and provided ~26 dB of gain. No significant pulse distortion is observed at the output of this amplifier. Figure A1.1 (a) shows the experimental (solid lines) and simulation (dashed lines) output pulse shapes from the second amplifier, using increasing pump powers of 5.7 W, 13.7 W, 21.7 W, and 25.7 W, respectively. For significantly reshaped output pulses, after the final amplifier, with the highest energy of 0.35 mJ = (1.84 × saturation energy), the time dependent gain, $g(t)$, in the final amplifier is reduced from 23 dB at the leading edge of the pulse, to 8 dB for its trailing edge. Figure A1.1 (b) shows the maximum gain variations across the pulse, at different pulse energy levels, at the output of the final amplifier. Good agreement is obtained between simulation results (solid line) and experimental results (dots).

As examples of the usefulness of the model, Figure A1.2 shows the simulation predictions of the input pulses that are required to achieve specific output pulses, such as triangular, square, and two-step shapes. These output pulse shapes are then realized experimentally. The experimental results are also shown in Figure A1.2 for comparison. The peak power of the input pulses from the diode source was ~0.35 W in each case, and the output peak power was (a) 10.6 kW for the triangular output, (b) 2.6 kW for the square output, and (c) 4 kW for the two-stepped output. This demonstration illustrates the benefits of gain dynamic modeling for optimizing pulsed applications of Yb-fiber amplifier technology.

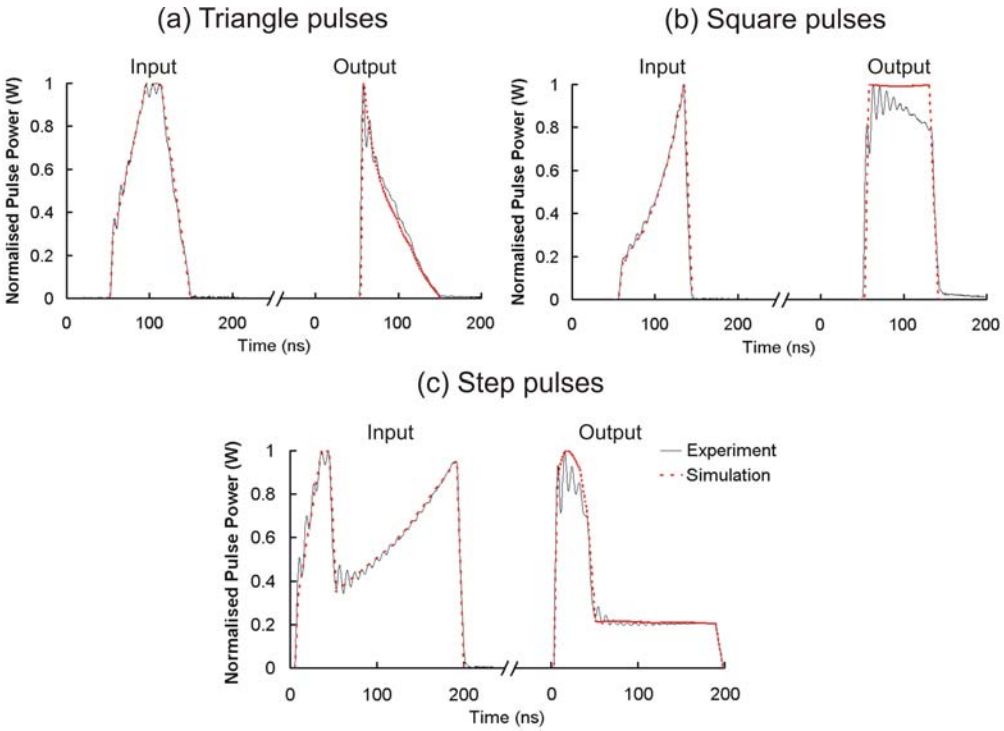

Figure A1.2: Experimental (solid line) and simulation (dashed line) results demonstrating how the desired output pulse shapes were obtained by pre-shaping the input pulses, in the presence of gain saturation, in an Yb-fiber amplifier system. (Examples shown are (a) triangular, (b) square, and (c) step output pulses.)

References:

[1] R. Paschotta, J. Nilsson, A. C. Tropper, and D. C. Hanna, "Ytterbium-doped fiber amplifiers," *IEEE Journal of Quantum Electronics*, vol. 33, pp. 1049-1056, 1997.

[2] A. Galvanauskas, Z. Sartania, and M. Bischoff, "Millijoule femtosecond all-fiber system," presented at Conference on Lasers and Electro-Optics, Baltimore, 2001, paper CMA1.

[3] A. Piper, A. Malinowski, K. Furusawa, and D. J. Richardson, "High-power, high-brightness, mJ Q-switched ytterbium-doped fibre laser," *Electronics Letters*, vol. 40, pp. 928-929, 2004.

[4] E. Desurvire, *Erbium-doped fiber amplifiers: principles and applications*: New York: Wiley, 1994.

[5] A. Bononi and L. A. Rusch, "Doped-fiber amplifier dynamics: A system perspective," *Journal Of Lightwave Technology*, vol. 16, pp. 945-956, 1998.

[6] Y. Sun, J. L. Zyskind, and A. K. Srivastava, "Average inversion level, modeling, and physics of erbium-doped fiber amplifiers," *IEEE Journal of Selected Topics in Quantum Electronics*, vol. 3, pp. 991-1007, 1997.

[7] G. P. Agrawal, *Nonlinear Fiber Optics*, 3rd ed. San Diego: Academic Press, 2001.

[8] S. R. Chinn, "Simplified modeling of transients in gain-clamped erbium-doped fiber amplifiers," *Journal of Lightwave Technology*, vol. 16, pp. 1095-1100, 1998.

[9] Y. Wang and H. Po, "Dynamic characteristics of double-clad fiber amplifiers for high-power pulse amplification," *Journal of Lightwave Technology*, vol. 21, pp. 2262-2270, 2003.

[10] D. N. Schimpf, J. Limpert, A. Tünnermann, and F. Salin, "Seed pulse optimization for saturated fiber-amplifiers," in *Conference on Laser and Electro-Optics*. San Jose: Optical Society of America, 2008.

Appendix II Introduction to dielectric gratings technology and stretcher alignment procedures

The high power CPA systems that are presented in this thesis research rely extensively on the diffraction grating based stretchers and compressors. This appendix introduces the design of dielectric gratings, and the alignment procedure for the dielectric grating stretcher.

A2.1 Dielectric grating design

One of the limiting components in Yb-fiber based CPA systems for high average power and high energy femtosecond pulse generation is the pulse compressor, particularly the efficiency and the optical damage resistance of the diffraction gratings. Metallic reflection grating incorporates high reflectivity with diffraction. The conductivity of the metal forces reflection, while periodic grooves create diffraction. Because metallic gratings owe their reflectivity to conductivity, they absorb high intensity radiation which leads to heating and damage. Metallic reflection grating with diffraction efficiency as high as 95% has been reported [1], and they are commercially available with typical efficiency of approximately 90%. Fused silica based transmission gratings have enhanced damage threshold than metallic reflection gratings [2]. Such gratings have been demonstrated in fiber CPA systems with high diffraction efficiency (~95%) and high average power (over 100 W) handling ability [3]. However, the size of the fused silica transmission grating is limited by the lithographic fabrication technique, which consequently constrained its application into high pulse energy fiber CPA system where extremely high pulse compression ratio is required. Dielectric gratings, which are made by layer of dielectric materials, have much smaller absorption coefficients than metals. Dielectric gratings not only provide a high peak intensity damage threshold, which is ~10 times that of gold gratings [4], but also enable operation at kilowatt average power levels without thermal distortion due to the low surface absorption [5]. Dielectric

gratings with diffraction efficiency as high as 99% have been reported [6]. Therefore, it would be desirable to use dielectric gratings in the work that presented in this thesis research.

As shown in Figure A2.1, a multilayer dielectric grating consists of a layer of grooves on the surface to provide the diffraction, and a multilayer dielectric stack to provide high reflectivity. The adjustable grating parameters are the groove density, depth, shape and duty cycle, which determine the diffraction properties. Multilayer stacks, which consist of thin (sub-wavelength-thickness) dielectric films, rely on interference to produce reflection. Note that the fabrication of such multilayer dielectric stacks is widely used in the optics industry such as for mirrors and anti-reflection coatings.

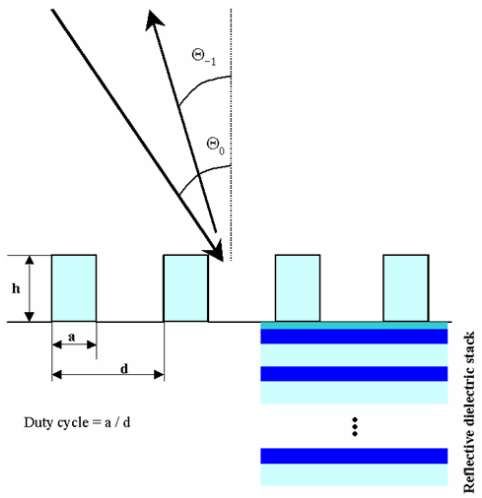

Figure A2.1: Schematic of multilayer dielectric grating

The highest possible efficiency is required when the gratings are used for pulse compression in CPA systems. High efficiency operation can originate from the analysis of the grating equation

$$m\frac{\lambda}{d} = \sin\Theta_0 + \sin\Theta_m \tag{A2.1}$$

where λ is the wavelength, d is the groove spacing, Θ_0 is the incident angle, and Θ_m is the diffracted angle for the diffraction order m. When a reflection grating is used in a first-order Littrow setup, the angle of incidence is decided by

$$\Theta_l = \sin^{-1}\left(\lambda / 2d\right) \tag{A2.2}$$

To achieve high efficiency, d is chosen to ensure that only two propagation orders exist (specular reflection, order $m = 0$, and back-reflection, order $m = -1$), and the gratings are used in the first order near-Littrow mount [7]. With such a configuration,

high diffraction efficiency can be obtained by a proper coating design, adjusting the depth of the grooves and controlling the thickness of the top layer [8, 9]. In practice, multilayer dielectric gratings with 96~99% diffraction efficiency into the $m = -1$ order were demonstrated in 1995 [6, 8]. A detailed discussion on the design of dielectric gratings can be found in references [7, 9].

A2.2 Dielectric grating stretcher alignment

This section presents the alignment procedure of the dielectric grating stretcher described in Chapter 6.

Figure A2.2 shows the optical layout of the stretcher. For convenience, the stretcher was designed as a fiber-pigtailed 'black-box' component with passive single-mode fiber at the input and the output, although it increased the difficulty of the alignment, especially at the launching of the output fiber. In Figure A2.2, B1 and B2 represent the grating, and M1, M2, …, M12 represent all the other mirrors used in the setup. The green line in the figure shows the optical path of the input beam at the central wavelength of 1055.335 nm. The red and blue lines indicate the optical path of shorter (blue) and longer (red) wavelengths in the stretcher respectively.

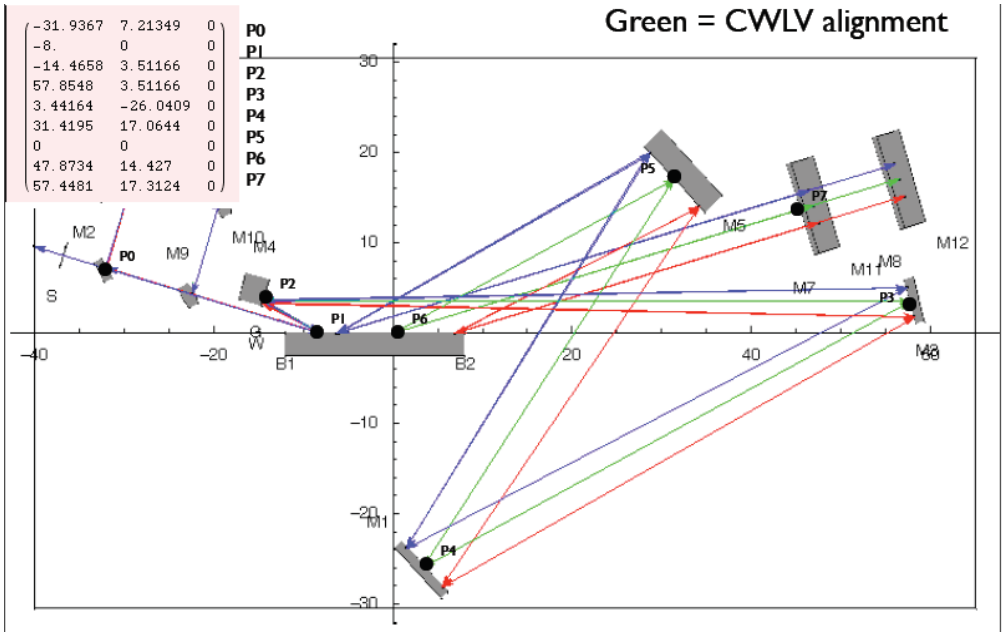

Figure A2.2: Optical path of the stretcher design used for alignment. The top left inset shows the (x,y,z) co-ordinates of P0-P7. (design provided by LLNL)

The inset of the figure shows the x- and y-axis position of P1, P2, …, P7, which are the main reflection points in the setup. The total path length of the beam is approximately 12.5 m. This requires the beam to have a diameter of more than 2.4 mm FWHM in order that it remains well collimated over the path length. However, the beam diameter cannot expand much more than 2.4 mm FWHM because otherwise the beam would clip on M4, as well as the small aperture of the output aspheric lens that is used to couple light into the output fiber-pigtail.

The stretcher alignment was performed at the ORC and the procedure can be summarized as follows:

- The grating was aligned within its mount prior to the incorporation into the stretcher. As shown in Figure A2.3, the adjustments include the minimization of tip (orientation of the grating surface) and tilt (orientation of the grating grooves) errors. In practice, the tip error was minimized first by ensuring that the 0^{th} order diffracted beam is in the same height as the input beam. Then tilt error was minimized by ensuring that both the 0^{th} and 1^{st} order diffracted beam are in the same horizontal plane as the input beam. A narrow bandwidth (<0.01 nm, FWHM), tunable (1025-1080 nm), CW laser from Sacher Lasertecknik Group is used for the alignment. The achieved angular error after the alignment is estimated to be less than ±0.001 radian.

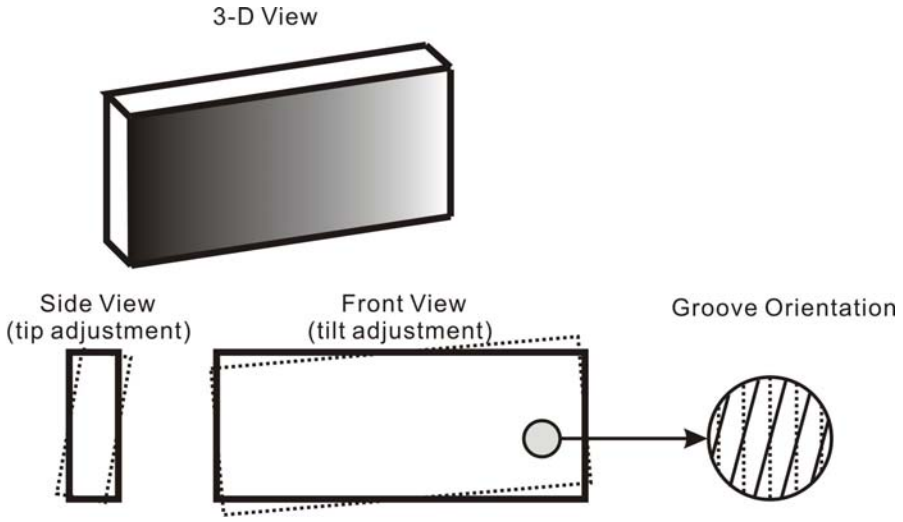

Figure A2.3: Adjustment of grating within its mount

- Two cylindrical (M4 and M5) mirrors were used in the setup so that the mirrors could be used off axis without introducing additional beam divergence in the vertical dimension. These mirrors were aligned within the mounts to minimize the tip and tilt errors (defined as shown in Figure A2.3) before being

incorporated into the stretcher. In practice, the tip error was minimized first by ensuring that the reflected beam was in the same horizontal plane as the input beam. Then the tilt error was minimized by translating the mounted mirror perpendicular to the input beam and making sure that the reflected beam was always at the same height as the input beam. The achieved angular error after the alignment is estimated to be less than ±0.001 radian.

- The vertical roof mirror assembly, including M7, M8, M11 and M12, was aligned separately prior to the incorporation into the stretcher. As shown in Figure A2.4, the roof mirror was adjusted in two orientations to ensure that the output beam was parallel to the input beam, which, after the grating diffraction, is spatially expanded in the horizontal plane. As a collimated Gaussian beam from the Sacher laser, rather than a horizontally expanded beam, was used in the alignment, the adjustments were realized by moving the roof mirror assembly perpendicular to the input beam and making sure that the output beam was always parallel to the input beam.

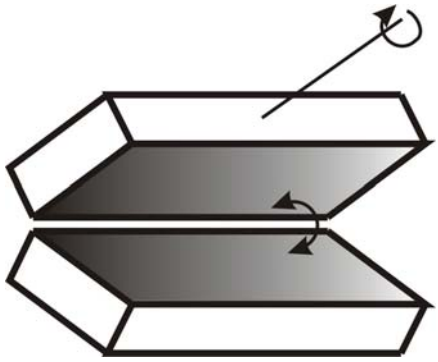

Figure A2.4: Adjustment of roof mirror assembly within its mount

- M2, M6, M9 and M10 are assembled as a staircase to raise the beam height and to invert the image of the beam in the plane of diffraction before the second round trip. This technique reduces the spatial chirp of the pulse. The staircase was aligned separately before incorporating it into the stretcher, ensuring that the output beam was parallel to and vertically above the input beam at the same height as the design.

- Lines were scribed onto the optical bench corresponding to the required beam path for the central wavelength of 1055.335 nm, as shown by green lines in Figure A2.2. Points P1-P7 were marked onto the optical bench. The 0^{th} order reflected beam is also scribed onto the optical bench.

- The narrow line-width tunable laser, tuned at centre wavelength of

1055.335 nm, was connected to the stretcher input fiber for alignment. A telescope was built to collimate the beam from the input fiber, and the intensity profiles of the beam were measured at 2 m intervals along a beam path of ~14 m by using a CCD camera. The telescope design was experimentally optimized to ensure that the collimated beam had approximately 2.4 mm FWHM diameter at ~12 m away along the beam path.

- The laser was aligned along P0-P1 line at the designed beam height. The grating was placed in the horizontal-axis by monitoring both the 1^{st} order diffracted light along the P1-P2 line and the 0^{th} order reflected light along the reflection line. The grating was placed on the horizontal-axis in Figure A2.2 with the input beam 5~10 mm away from the side of the grating. When the grating was positioned correctly, the alignment laser followed both the zero and first order lines precisely all the way to the edges of the breadboard, at the same height as the incident beam.
- M4 was placed at P2, by monitoring reflected beam along P2-P3.
- M3 was placed at P3, by monitoring reflected beam along P3-P4.
- M1 was placed at P4, by monitoring the reflected beam along P4-P5.
- M5 was placed at P5, by monitoring the reflected beam along P5-P6.
- The roof mirror assembly was placed at P7, ensuring that the return beam is oppositely directed and vertically displaced from beam coming from P6.
- The staircase assembly was incorporated in the setup, ensuring that the returning beam is oppositely directed and vertically displaced from beam coming from P1 towards P0.
- The output beam of the stretcher was launched from free-space to a piece of passive single-mode fiber.
- The alignment laser was disconnected from the stretcher input fiber, and the broad bandwidth signal of the CPA system from the mode-locked oscillator was connected to the stretcher input fiber.
- A full characterization of the stretcher was carried out, and the results were presented in Chapter 6.

Reference:

[1] R. D. Boyd, J. A. Britten, D. E. Decker, B. W. Shore, B. C. Stuart, M. D. Perry, and L. Li, "High-efficiency metallic diffraction gratings for laser applications," *Applied Optics*, vol. 34, pp. 1697-1706, 1995.

[2] T. Clausnitzer, J. Limpert, K. Zollner, H. Zellmer, H. J. Fuchs, E. B. Kley, A. Tunnermann, M. Jupe, and D. Ristau, "Highly efficient transmission gratings in fused silica for chirped-pulse amplification systems," *Applied Optics*, vol. 42, pp. 6934-6938, 2003.

[3] J. Limpert, T. Clausnitzer, A. Liem, T. Schreiber, H. J. Fuchs, H. Zellmer, E. B. Kley, and A. Tunnermann, "High-average-power femtosecond fiber chirped-pulse amplification system," *Optics Letters*, vol. 28, pp. 1984-1986, 2003.

[4] C. P. J. Barty, M. Key, J. Britten, R. Beach, G. Beer, C. Brown, S. Bryan, J. Caird, T. Carlson, J. Crane, J. Dawson, A. C. Erlandson, D. Fittinghoff, M. Hermann, C. Hoaglan, A. Iyer, L. J. II, I. Jovanovic, A. Komashko, O. Landen, Z. Liao, W. Molander, S. Mitchell, E. Moses, N. Nielsen, H.-H. Nguyen, J. Nissen, S. Payne, D. Pennington, L. Risinger, M. Rushford, K. Skulina, M. Spaeth, B. Stuart, G. Tietbohl, and B. Wattellier, "An overview of LLNL high-energy short-pulse technology for advanced radiography of laser fusion experiments," *Nuclear Fusion*, vol. 44, pp. S266-S275, 2004.

[5] J. Limpert, F. Roser, T. Schreiber, and A. Tunnermann, "High-power ultrafast fiber laser systems," *IEEE Journal of Selected Topics in Quantum Electronics*, vol. 12, pp. 233-244, 2006.

[6] N. Destouches, A. V. Tishchenko, J. C. Pommier, S. Reynaud, and O. Parriaux, "99% efficiency measured in the -1st order of a resonant grating," *Optics Express*, vol. 13, pp. 3230-3235, 2005.

[7] B. W. Shore, M. D. Perry, J. A. Britten, R. D. Boyd, M. D. Feit, H. T. Nguyen, R. Chow, and G. E. Loomis, "Design of high-efficiency dielectric reflection gratings," *Journal of Optics Society of America A*, vol. 14, pp. 1124-1136, 1997.

[8] M. D. Perry, R. D. Boyd, J. A. Britten, D. Decker, B. W. Shore, C. Shannon, and E. Shults, "High-Efficiency Multilayer Dielectric Diffraction Gratings," *Optics Letters*, vol. 20, pp. 940-942, 1995.

[9] K. Hehl, J. Bischoff, U. Mohaupt, M. Palme, B. Schnabel, Lutz Wenke, R. Bodefeld, W. Theobald, E. Welsch, R. Sauerbrey, and H. Heyer, "High-efficiency dielectric reflection gratings: design, fabrication, and analysis," *Applied Optics*, vol. 38, pp. 6257-6271, 1999.

Appendix III Publication list

Journal papers:

1. **F. He**, H.S.S.Hung, J.H.V.Price, N.K.Daga, N.Naz, J.Prawiharjo, D.C.Hanna, D.P.Shepherd, D.J.Richardson, J.W.Dawson, C.W.Siders, and C.P.J.Barty, "High energy femtosecond fiber chirped pulsed amplification system with adaptive phase control," *Optics Express*, vol. 16, pp. 5813-5821, 2008.

2. **F. He**, J.H.V.Price, K.T.Vu, A.Malinowski, J.K.Sahu, and D.J.Richardson, "Optimisation of cascaded Yb fiber amplifier chains using numerical-modelling," *Optics Express*, vol. 14, pp. 12846-12858, 2006.

3. M. L. V. Tse, P.Horak, J.H.V.Price, F.Poletti, **F.He**, and D.J.Richardson, "Pulse compression at 1.06 microns in dispersion-decreasing holey fibers," *Optics Letters*, vol. 31, pp. 3504-3506, 2006.

Conference papers:

4. D.J.Richardson, F.Poletti, M.L.V.Tse, P.Horak, J.Y.Y.Leong, **F.He**, J.H.V.Price, X.Feng, H.N.Rutt, K.E.Frampton, W.H.Loh, S.Asimakis, P.Petropoulos, "Recent advances in highly nonlinear microstructured optical fibers and their applications," in *Asia Optical Fiber Communication and Optoelectronic Exposition and Conference*. Shanghai 2008, SuB1 (Invited).

5. **F. He**, H.S.S.Hung, N.K.Daga, N.Naz, J.Prawiharjo, J.H.V.Price, D.C.Hanna, D.P.Shepherd, D.J.Richardson, J.W.Dawson, C.W.Siders, and C.P.J.Barty, "High energy femtosecond fiber chirped pulse amplification system with adaptive phase control," in *Conference on Lasers and Electro-Optics*. San Jose 2008, CThB5.

6. N. K. Daga, **F. He**, H. S. S. Hung, N. Naz, J. Prawiharjo, D. C. Hanna, D. J. Richardson, and D. P. Shepherd, "Adaptive Phase Shaping in a Fiber Chirped

Pulse Amplification System," in *Conference on Ultrafast Phenomena*. Stresa, Italy 2008, poster.

7. **F. He**, J. H. V. Price, A. Malinowski, A. Pipe, M. Ibsen, and D. J. Richardson, "High Average Power, High Energy, Femto-second Fiber Chirped Pulse Amplification System," in *Conference on Lasers and Electro-Optics*, Baltimore 2007, CMEE5.

8. **F. He**, J.H.V.Price, and D. J. Richardson, "Optimisation of short pulse multi-stage Yb fiber amplifier systems using commercial gain-modelling software," in *Conference on Lasers and Electro-Optics*, Long Beach 2006, CThR6.

9. A. Malinowski, J.H.V.Price, **F. He**, P.Dupriez, H.D.Foreman, A.C.Tropper, and J.Nilsson, "Pulsed high power fiber laser systems," in *IEEE/LEOS Summer Topical Meeting*. Quebec City 2006, MC2.2 (Invited).

10. J. H. V. Price, A.Malinowski, A.Piper, **F. He**, W.Belardi, T.M.Monro, M.Ibsen, B.C.Thomsen, Y.Jeong, C.Codemard, M.A.F.Roelens, P.Dupriez, J.K.Sahu, J.Nilsson, and D.J.Richardson, "Advances in high power short pulse fiber laser systems and technology," in *Photonics West*. San Jose 2005, 5709-30 (Invited).

11. A.Malinowski, A.Piper, J.H.V.Price, **F. He**, M.Ibsen, J.Nilsson, and D.J.Richardson, "Short pulse high power fiber laser systems," in *Conference on Lasers and Electro-Optics*. Baltimore, 2005, (invited).